NASA CR-159567

PHYSICAL PROCESSES IN DIRECTED ION BEAM SPUTTERING

PREPARED FOR

LEWIS RESEARCH CENTER

NATIONAL AERONAUTICS AND SPACE ADMINISTRATION

GRANT 3086

by

Raymond S. Robinson

March 1979

Department of Physics
Colorado State University
Fort Collins, CO 80523

1. Report No. NASA CR-159567	2. Government Accession No.	3. Recipient's Catalog No.
4. Title and Subtitle PHYSICAL PROCESSES IN DIRECTED ION BEAM SPUTTERING (U)		5. Report Date March 1979
		6. Performing Organization Code
7. Author(s) Raymond S. Robinson		8. Performing Organization Report No.
9. Performing Organization Name and Address Department of Physics Colorado State University Fort Collins, Colorado 80523		10. Work Unit No.
		11. Contract or Grant No. NSG-3086
		13. Type of Report and Period Covered
12. Sponsoring Agency Name and Address National Aeronautics and Space Administration Washington, DC 20546		14. Sponsoring Agency Code

15. Supplementary Notes

Grant Manager - Michael J. Mirtich, Jr., NASA Lewis Research Center, Cleveland, Ohio 44135.
This is a reproduction of the Ph.D. Thesis of Raymond S. Robinson done under Harold R. Kaufman.

16. Abstract

Directed ion beam sputtering is becoming a widely accepted physical method for both the removal and deposition of material. This investigation provides insight in terms of specific physical models into some aspects of the processes that take place during directed ion beam sputtering. The general operation of a discharge chamber for the production of ions is described. A model is presented for the magnetic containment of both primary and secondary or Maxwellian electrons in the discharge plasma. Calculations have been made of cross sections for energy and momentum transfer in binary collisions between like pairs of Ar, Kr, and Xe atoms in the energy range from about 1 eV to 1000 eV. These calculations were made from available pair interaction potentials using a classical model. Experimental data from the literature has been fit to a theoretical expression for the Ar resonance charge exchange cross section over the same energy range. A model has been developed that describes the processes of conical texturing of a surface due to simultaneous directed ion beam etching and sputter deposition of an impurity material. This model accurately predicts both a minimum temperature for texturing to take place and the variation of cone density with temperature. It also provides the correct order of magnitude of cone separation. It was predicted from the model, and subsequently verified experimentally, that a high sputter yield material could serve as a seed for coning of a lower sputter yield substrate. Seeding geometries and seed deposition rates were studied to obtain an important input to the theoretical texturing model.

17. Key Words (Suggested by Author(s)) Ion beams Ion etching Sputtering Ion beam texturing Bohm diffusion Rare gas cross sections	18. Distribution Statement Unclassified-Unlimited

19. Security Classif. (of this report) Unclassified	20. Security Classif. (of this page) Unclassified	21. No. of Pages	22. Price*

* For sale by the National Technical Information Service, Springfield, Virginia 22161

NASA-C-168 (Rev. 10-75)

TABLE OF CONTENTS

LIST OF FIGURES

Figure Page

LIST OF TABLES

I. INTRODUCTION

Directed ion beam sputtering is becoming a widely accepted physical method for both the sputter etching and deposition of thin films, not only in specialized research laboratories but as an everyday tool for industrial processes. The growth of this technique is evidenced by the number of commercial firms offering production ion beam equipment either as a recent addition to existing product lines or in the form of completely new ventures.

Three important parts of the complete directed ion beam sputtering process are: (1) the nature of the discharge chamber plasma where the ions are formed, (2) properties of the ion beam itself, and (3) the effects of ion bombardment on a solid substrate or target.

Present Investigation

The objective of the present investigation is to provide insight, in terms of specific physical models, into certain aspects of the processes that take place in the three areas listed above.

Plasma and Ion Beam Generation

Magnetic fields have been applied in electron bombardment ion sources to enhance ionization by increasing the path lengths of energetic or primary electrons. These fields have usually been applied in such a way that they extend over and strongly influence the entire region within which ion production takes place. Decoupling of the magnetic field from the ionization region through the use of the multipole concept has allowed conceptual simplification in understanding and modeling interaction of the field with the different electron populations in a discharge plasma, while at the same time, improving ion beam uniformity and allowing source design and construction to proceed without numerous iterations. The dual role of the magnetic field in, (1) containing high energy or primary electrons to enhance ionization, and (2) allowing the conduction of thermalized secondary or Maxwellian electrons to anodes to sustain an arc discharge can be understood through modeling a multipole field that is concentrated at the boundaries of the plasma volume. This modeling approach is used in the plasma studies herein.

Ion Beam Propagation

Ion beams can undergo a variety of interactions with background species present in the region a beam must traverse between the ion source and a target or substrate. The cross sections for various binary collision processes are investigated to determine the major interactions through which the physical properties of an ion beam may be altered. Resonance charge exchange and elastic collision cross sections are studied in detail, providing a measure of the background and pressure environments appropriate for ion beam sputtering.

Ion Beam Sputter Texturing

Ion beam texturing or coning of a solid substrate results when a surface is bombarded by an ion beam while an impurity is simultaneously deposited on the same surface. The texturing process, the distribution of cones on a surface, and cone suppression can be understood in terms of a surface diffusion and sputtering model involving ion beam characteristics, substrate temperature, and the physical properties of the substrate and impurity materials.

Background of Directed Ion Beam Sputtering

Research interest in ion beam sputtering has grown in recent years. An entire technical session[1,2,3,4,5,6,7,8] of the recent 25th National Symposium of the American Vacuum Society, with the exception of one paper, was devoted to ion beam sputtering. Sputter texturing[9,10] and submicron structure fabrication[11] using ion beams were also discussed at that symposium. In contrast, the previous symposium, one year before, had only two papers[12,13] on the subject of ion beam sputtering. A chapter covering in detail the subject of ion beam sputter deposition has recently been written by Harper.[14]

Ion sources and ion beams have been in use for many years, applied to a variety of tasks including providing charged particle beams for input to high energy accelerators, surface composition analysis and ion implantation in semiconductor devices. Sputtering has been exploited in magnetron and RF and DC diode plasma devices for the deposition of thin films.

The technique of directed ion beam sputtering involves some fairly specific requirements and advantages that set it apart from other, related processes. The energy range of interest is from a few hundred eV to a few thousand eV, not approaching the several tens of thousands and sometimes the hundreds of thousands of eV typical of ion implantation. Only marginal gains in sputter yield can be achieved by going beyond several hundred eV but severe substrate damage and/or ion implantation can result at high ion energies. Typical sputter etch rates for beams of a few mA/cm^2 current density are of the order of a few hundreds of Angstroms per minute. The pressure environment in which ion beam sputtering can be done is limited only by the capacity of the particular pumping system used and is not restricted to the relatively high pressures (about 30 mTorr) of RF and DC sputtering. Typical pressures range from 10^{-5} Torr to 10^{-3} Torr. This is because the plasma generation and sputtering environments can be almost completely decoupled in ion beam work. Perhaps the most significant feature of ion beam sputtering, setting it apart, is the use of broad beams created by bringing hundreds or thousands of individual beamlets together into the configuration desired for a specific application requiring high current densities. This is typically accomplished using a set of multiaperture electrodes to extract ions from a plasma and to accelerate and focus them through each set of apertures in the electrode system. Virtually every other ion beam device utilizes a single aperture through which all of the ion beam current must be directed. At low energies there are severe restrictions on the total current that can be extracted through a single aperture.[12] Because the useful work that can be done by an ion beam is often proportional to its current output, low to moderate energy tasks will usually be accomplished best using broad beam devices. Unlike alternative conventional sputtering devices, the broad beam ion source allows the ion energy, beam current density and angle of ion incidence to be controlled independently.

The unique features of ion beam sputtering are a direct result of the recent transference of a highly developed technology from rocket engines to ground-based processing.[15] Ion rockets have been developed by the National Aeronautics and Space Administration (NASA) for space propulsion. Out of a variety of candidate systems an electron bombardment ion source, using a magnetic field to enhance ionization and a multiple aperture accelerator system to generate a broad beam, has emerged as the system of choice for electric propulsion or ion drive.[16] Electron bombardment ion sources have undergone an extensive and intensive development program emphasizing reliability, long lifetimes, well-collimated beams, high current densities at moderate energies, and high propellent utilization efficiencies. Existing devices are highly optimized but remain, however, objects of considerable research into the basic physical principles of their operation.[17,18,19,20,21,22,23]

Materials processing applications of ion beam sputtering present an array of differing specific requirements that encourage development of ion beam systems along diverging lines while retaining the fundamental features that make these systems attractive. For example, etching processes may require very uniform current density profiles while deposition would demand very high current densities localized in as small an area as possible to minimize both target size and contamination. Associated with this development will be continued research into the physical processes involved in materials processing and ion beam sputtering including ion production; beam extraction, focusing, and acceleration; beam propagation and interaction with the background environment and, finally, interactions with targets and substrates. As indicated, the study of these processes constitutes the subject matter of this thesis.

II. PLASMA AND ION BEAM GENERATION*

Ion beams for sputtering applications are obtained by extracting ions from a plasma and accelerating the ions to the desired energy while focusing them electrostatically to form a beam. These ions are customarily singly ionized, atomic ions bearing a positive charge. The process of electron bombardment is generally used to produce the ions. Electron bombardment may produce not only single ions but a small fraction of multiply ionized atoms as well. It is generally not important in most considerations of these beams and plasmas to treat the multiple ions in detail because they constitute only a very small fraction of the beam. Negative ions may also be neglected in electron bombardment devices because of the low particle densities used and because rare gases are typically employed whose negative ions are not stable.

Plasma Generation

Ion source plasmas are generated by an electrical discharge between a cathode and an anode inside of a suitable container into which the working gas can be injected. Discharge currents of a few Amperes are common along with pressures in the 10^{-3} to 10^{-4} Torr range. Figure 2-1 is a schematic representation of a discharge chamber showing a general layout of cathode, anode, magnetic field, and accelerator system. The purpose of the magnetic field was initially to increase the path length and therefore the ionization efficiency of ionizing electrons by constraining them to follow helical paths inside the discharge chamber. Gas discharges have been commonly used to supply ions for experimental use. Typically, single aperture beam

---

*Some of the work presented in this chapter was done under NASA Grant NSG-3011.

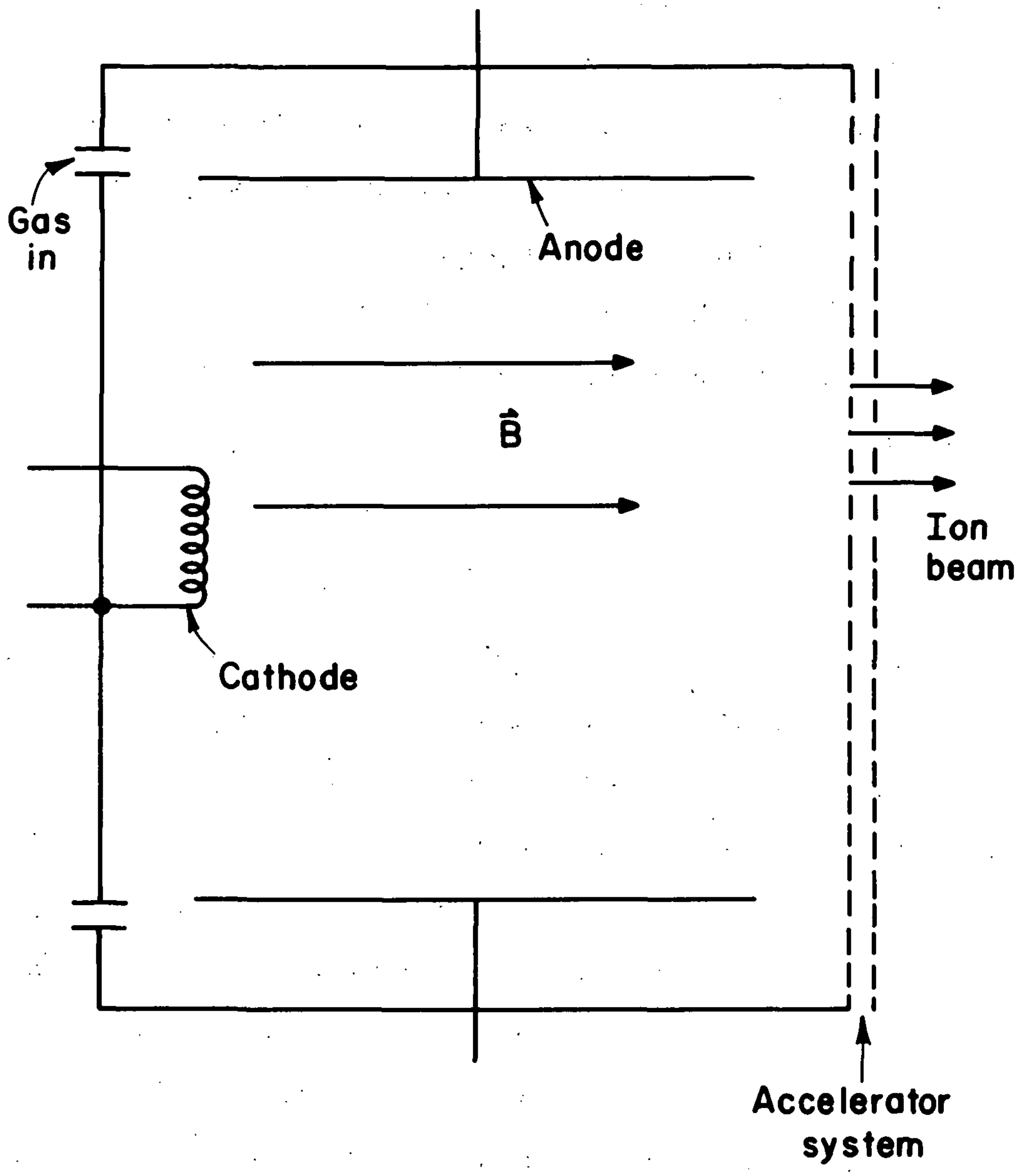

Figure 2-1. General discharge chamber schematic.

extraction techniques and relatively low beam currents have been satisfactory. However, the ion source performance objectives for ion milling or ion machining applications are high ion current density, a uniform beam current density profile, and generally, a low ion energy which is usually obtained by sacrificing current density. In addition, a large ion source with a uniform beam current density profile allows consistent processing over large areas. The beam should also be uniform and collimated so that a maximum ion current density can be used at a large distance from the ion source. An increased distance from the source to the target decreases mutual contamination of the target and the ion source.

Magnetic Field Evolution

A considerable effort has gone into increasing the size, efficiency and reliability of discharge plasma devices in conjunction with the development of ion thrusters for space propulsion by NASA. This lengthy development effort is described by Kaufman.[1] The evolution of the discharge chamber configuration over a long period has been primarily in incremental alterations to the distribution of the magnetic field inside the chamber. Beginning with the earliest designs having an axial field, the direction that succeeding improvements have taken is shown schematically in Fig. 2-2 along with the general shape of the associated ion beam current density profile. Beattie[2,3] describes the impact of these improvements in magnetic field distribution on the lifetime of space thruster accelerator systems through assessments of the undesirable effects of highly non-uniform beam current density profiles.

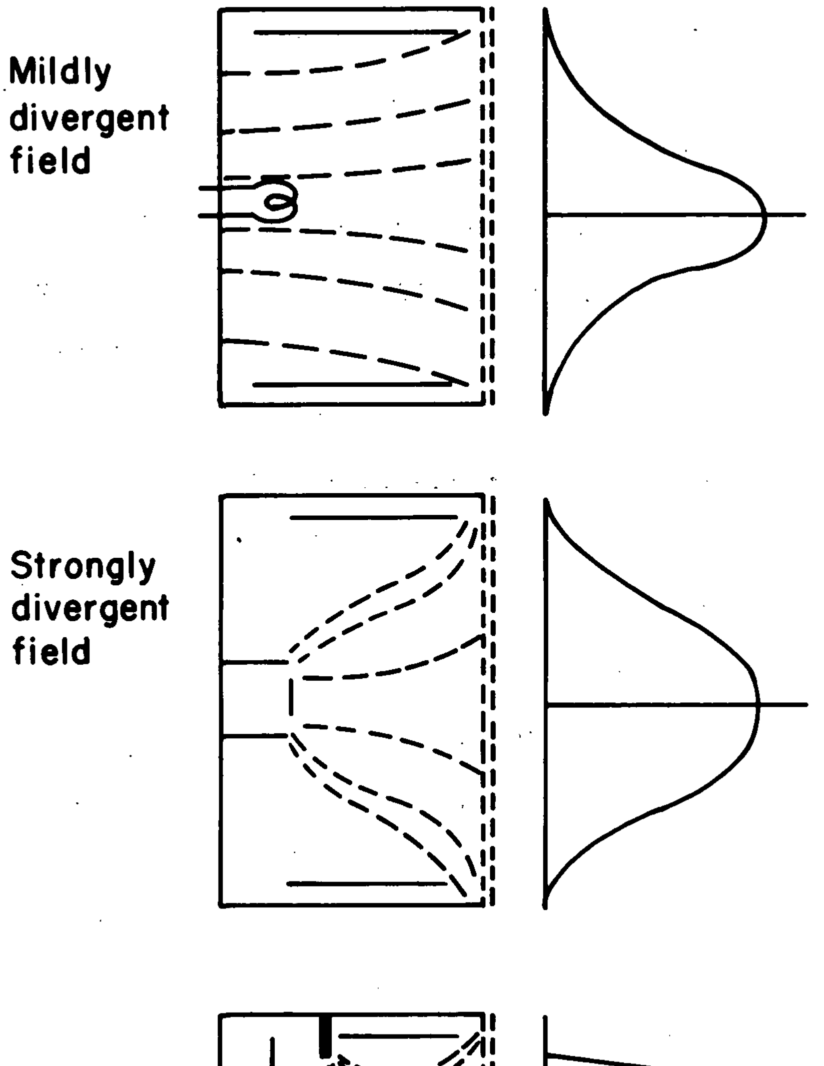

Figure 2-2. Early magnetic field configurations inside of discharge chambers with associated beam current density profiles.

As Fig. 2-2 clearly shows, the magnetic field has generally permeated the entire plasma inside the discharge chamber in early designs. This intimate coupling of the plasma and the magnetic field has helped to make theoretical analyses of discharge chamber processes extremely difficult, resulting in a cut and try approach as the only fruitful means of improving discharge configurations. A significant simplification is possible using a low field multipole design that allows almost a complete decoupling of the magnetic field from the bulk of the discharge plasma. An ion source with a multipole magnetic field is reported by Isaacson and Kaufman.[4] As described therein, this design is conceptually related to both the multipole approach of Moore[5] and Ramsey,[6] and the cusped field approach of Beattie and Wilbur.[3] The low field in a multipole design has specific performance objectives in terms of interactions with the two dominant electron populations in a discharge plasma and should not be confused with high magnetic field approaches to plasma containment.

Discharge Chamber

This study involved the use of various multipole discharge chambers. The largest multipole chamber to date (30 cm diameter) was designed and constructed in connection with this work. This chamber will be described to provide a concrete example of the multipole concept.

A cylindrical discharge chamber was selected with an inside diameter of 30 cm and a depth of 10 cm. A radial cross-section of the 30-cm discharge chamber showing construction details is shown in Fig. 2-3. A multipole discharge chamber will generally produce a more

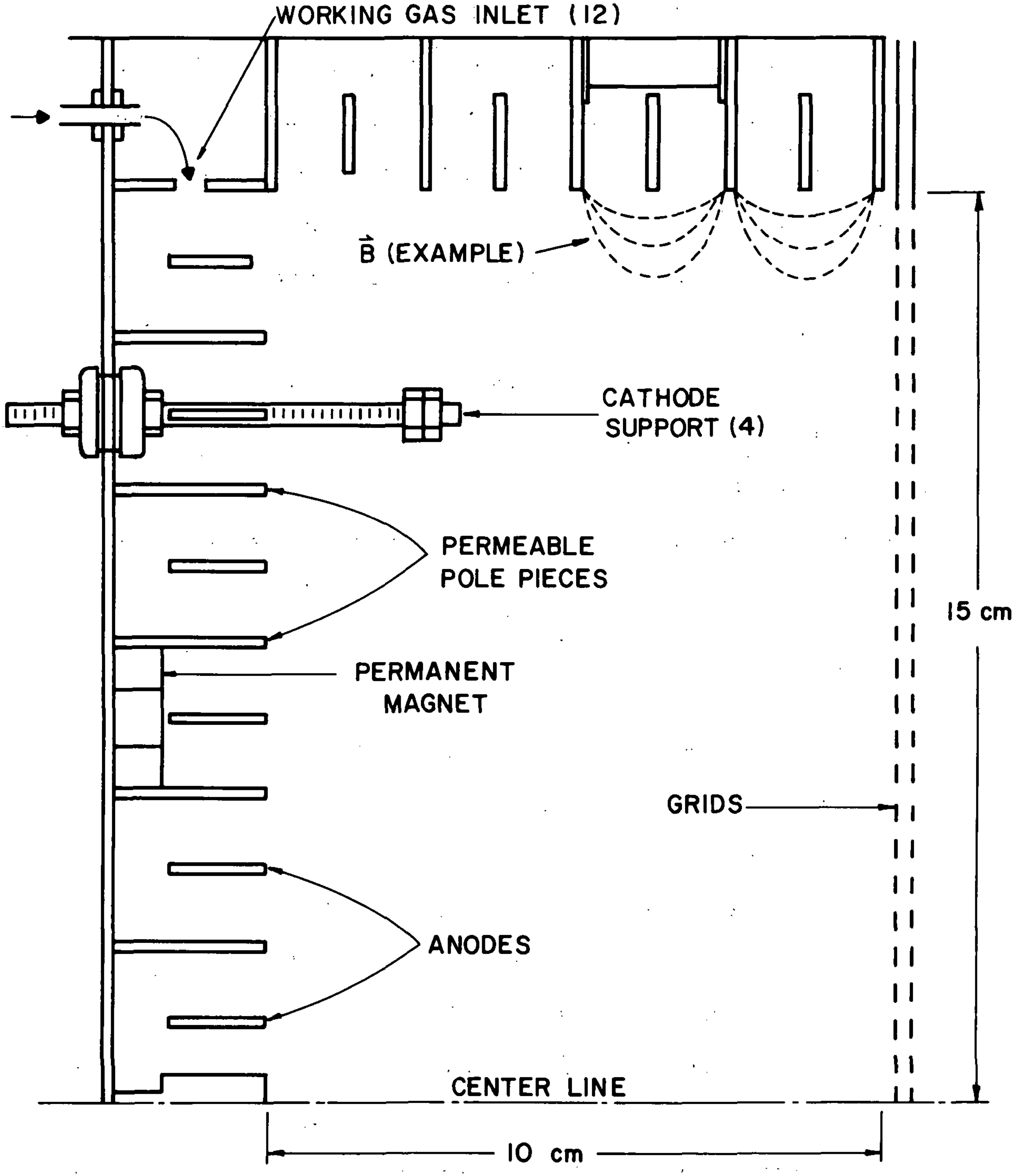

Figure 2-3. Radial cross section of a 30-cm ion source.

uniform ion beam current density profile as the chamber is decreased in depth, however, the minimum working gas pressure inside the chamber required for operation will increase as chamber depth is decreased. Data obtained by Isaacson and Kaufman[4] showed these trends down to a chamber depth equal to about half of the 15 cm diameter used in their investigations. The absence of any further improvement in uniformity for smaller depths was felt due, in part, to the close proximity of the central refractory cathode to the accelerator system. With the circumferential cathode employed in the 30 cm source, a further decrease in depth was expected to improve beam uniformity for the larger source. A chamber depth equal to one third of the 30 cm diameter was therefore selected.

The magnetic field in the source was provided by 139 Alnico V permanent magnets. The five side pole pieces are annular disks of 30.5 and 35.6 cm inside and outside diameters. The 1.5 mm thick low-carbon steel pole pieces were spaced about 2.5 cm apart. There are twenty permanent magnets between each pair of pole pieces on the sides for a total of eighty magnets in these locations. The pole pieces on the upstream end of the discharge chamber are rolled cylinders of 1.5 mm thick, low-carbon steel. The center pole piece was a solid cylinder that was required to have a diameter of 9.5 mm to avoid saturation. All hardware at the upstream end is mounted on an aluminum plate 3.2 mm thick and 35.6 cm in diameter. On the upstream end, beginning at the center, there are two, five, eight, twelve, fourteen, and eighteen magnets between adjacent sets of pole pieces for a total of fifty-nine magnets.

The sense of the magnets surrounding the discharge chamber is such that the magnetic polarity of adjacent pole pieces is opposite. An example of the magnetic field lines in the fringe field between pole pieces is shown schematically by dotted lines in Fig. 2-3. An essential feature of this multipole design of alternating polarity is that the fringe field decreases very rapidly with increasing distance from the pole pieces, so that the magnetic field is negligible over most of the discharge chamber volume. This results in relatively free access to this volume by primary electrons which would, in turn, be expected to give a more uniform plasma density.

Ten 1.5 mm thick non-magnetic stainless steel anodes are located at equal spacings along the side and upstream end of the discharge chamber. Each anode is midway between the two neighboring pole pieces (see Fig. 2-3). Like the pole pieces, the four side anodes are flat, annular disks and the six upstream anodes were rolled cylinders, ranging from about 2.5 cm to 28 cm in diameter. A cylindrical shroud of 0.25 mm stainless steel seals the sides of the discharge chamber. The side and upstream anodes are held by aluminum oxide isolating supports mounted on this shroud and on the upstream aluminum end plate.

Refractory metal cathodes of 0.25 mm tantalum wire were used in the discharge chamber. The periodic maintenance of thermionic emitters is not a major problem in ground applications. On the other hand, the extended emission surface of a wire discharge chamber cathode can be a definite advantage in obtaining a more uniform beam profile. Tungsten wire could have been used instead of tantalum, but tantalum was preferred because of its greater ductility.

The discharge chamber cathode was made in the shape of a square, held at the corners by four insulated supports extending through the upstream end of the chamber (see Fig. 2-3). The cathode supports extended far enough into the discharge chamber to prevent thermionic emission of electrons into the fringe magnetic field where they might be lost directly to the anodes. Electrical connections were made to the cathode corners so that the four side sections were effectively in parallel. Cathode placement was selected to enhance beam uniformity. The circumferential cathode employed was near the side (cylindrical) wall of the discharge chamber to help offset the decrease in plasma density usually found in that location. It was also located nearer the upstream end of the chamber to permit the use of a very flat chamber without the sharp peaks in beam current density that are often found when a cathode is close to the accelerator system.

Primary Electron Containment

The electrons in a discharge plasma of low density have been found to consist of a fraction of roughly monoenergetic primary electrons superimposed on a larger thermal distribution at lower energy. The primary electrons have roughly the energy corresponding to the potential difference between the cathode and the anode in the discharge chamber. When primary electrons lose energy, such as in the process of ionizing a neutral atom, both the primary electron and the secondary electron ejected from the atom can more rapidly thermalize because of their larger collision cross sections at lower energies.[7] This, then, is the mechanism leading to two distinct populations of electrons termed primaries and Maxwellians. The validity of this description of the electron distribution in the discharge chamber has been substantiated by the successful analyses of numerous electrostatic probe characteristics based on such a distribution, a priori, and by the detailed measurements of Medicus[8] and Martin.[9] These studies and the work presented herein show the primaries to be a 5 or 10 percent fraction of the total electron population.

In the multipole concept, a fringe magnetic field adjacent to the anodes prevents the escape of primary electrons directly to the anodes, before expending most of their energy in the production of ions, by deflecting them in the field. In calculating the deflection of an electron in such a fringe field, it is assumed that the radius of curvature of the anode is large compared to the depth of the fringe field. It is further assumed that the magnetic induction $\vec{B}$ is parallel to the anode and that its magnitude varies only as a function of the distance from the anode, and that a primary electron will not suffer a collision while it is in the fringe field.

In passing through an infinitesimal region dx, an electron with a component of velocity v normal to $\vec{B}$ is deflected through an angle $d\theta$, as indicated in Fig. 2-4. The radius of curvature for the electron trajectory in the region dx is

$$r = mv/q\ B(x) \ , \tag{2-1}$$

where m and q are the mass and charge of an electron. In Fig. 2-4, x represents the penetration depth of the electron into the fringe field from the field free region. The radius of curvature r can be related to $d\theta$ and dx through geometrical considerations,

$$r d\theta = dx/\sin\theta \ . \tag{2-2}$$

Combining Eqns. (2-1) and (2-2) to eliminate r,

$$B(x)dx = \frac{mv}{q}\sin\theta d\theta \ . \tag{2-3}$$

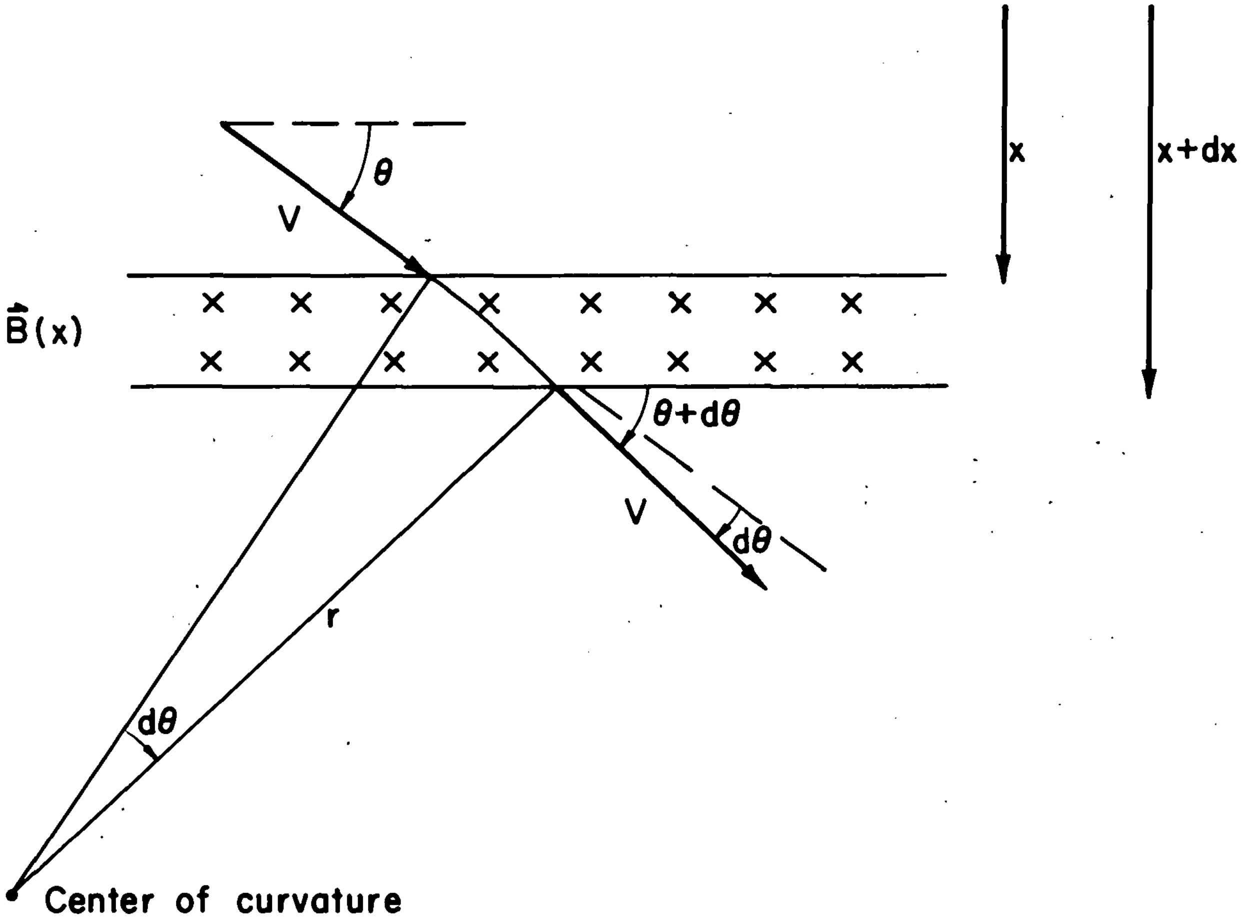

Figure 2-4. Electron deflection in an inhomogeneous magnetic field.

The integral of B(x)dx can be related to the electron deflection by

$$\int_0^D B(x)dx = \int_{\theta_i}^{\theta_f} \frac{mv}{q} \sin\theta d\theta \ , \tag{2-4}$$

where θ_i is the angle of incidence of the electron from the field free region and θ_f is the trajectory angle after the electron traverses a thickness D of magnetic induction. The maximum value of the angular integral corresponds to the maximum possible electron penetration toward the anode, and is obtained with θ_i equal to zero and θ_f equal to π. For these limits,

$$\int_0^D B(x)dx = 2mv/q \ . \tag{2-5}$$

In terms of electron kinetic energy E,

$$\int_0^D B(x)dx = \left(\frac{8m\ E}{q^2}\right)^{\frac{1}{2}} \ . \tag{2-6}$$

With the substitution for electron charge and mass, this becomes

$$\int_0^D B(x)dx = 6.74 \times 10^{-6}\ E^{\frac{1}{2}} \ , \tag{2-7}$$

where E is in electron-volts and the left-hand side is in SI units. This expression provides a criterion for primary electron containment by the integrated magnetic field. Charged particle containment where both electrical and magnetic fields are present is considered in Appendix A.

Primary electrons have long mean free paths, typically several cm, and are not likely to undergo strong deflection from the indicated trajectory while in the fringe field region. Low energy (a few eV) Maxwellian electrons, however, have much shorter path lengths, usually a few mm and are more likely to migrate across the fringe field region (by collision) to be collected at the anode, thus sustaining the discharge current.

Although this derivation did not specifically take into account the strong curvature of the magnetic field lines along some of the possible directions of approach to an anode, the criterion provided for the integrated magnetic field is valid as an upper limit for this case as well because circulating charged particles in regions where a magnetic field exists enclose within their orbits a fixed magnetic flux which depends on the charge and momentum of the particle.[10] Thus, there would be a critical magnetic field line beyond which an electron would not penetrate toward the anode for a given electron energy, regardless of the direction of approach.

Figure 2-5 shows a typical variation of magnetic field strength midway between two pole pieces measured for the 30 cm source. The plane of measurement is shown in the insert at the top of the figure. The magnetic field integral of interest would be the area under the curve from the inside field free region to the edge of the anode.

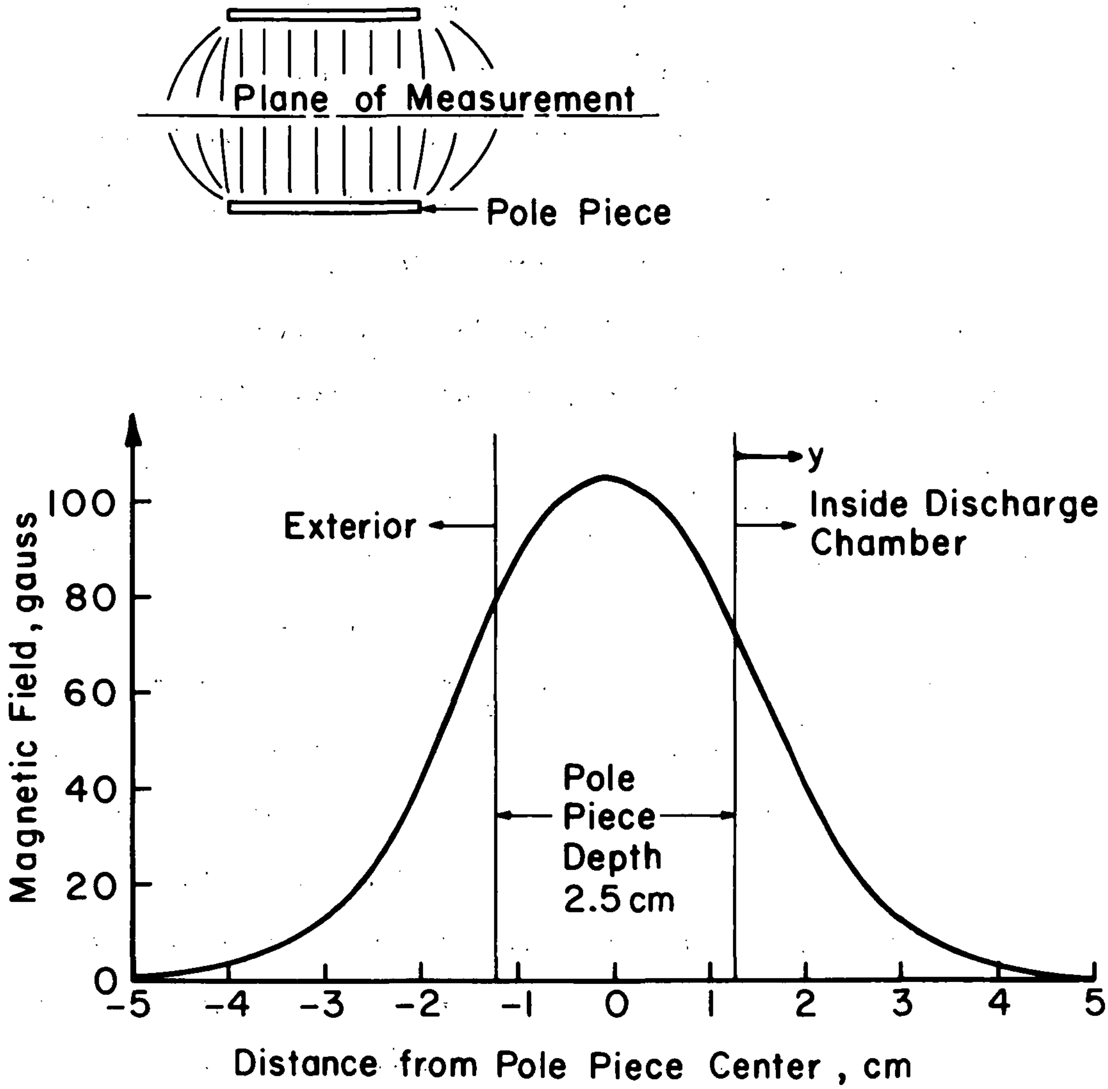

Figure 2-5. Variation of magnetic field midway between two pole pieces.

A least squares curve fit was obtained for the interior fringe field:

$$B(y) = 106\ e^{-0.235(y+1.27)^2} , \tag{2-8}$$

where y is the distance in cm from the anode edge and B(y) is in Gauss. As an example of the deflecting properties of the fringe field, using Eq. (2-8) for the field variation and integrating the equations of motion for an electron using a fourth-order Runge-Kutta method, a deepest penetration trajectory was obtained for a 45.5 eV electron. This trajectory is shown in Fig. 2-6. The depth of penetration shown is in agreement with the containment criterion, Eq. 2-6.

Plasma and Beam Uniformity

By restraining the primary electron population to a large field-free volume in the center of the discharge chamber, it was expected that the ion production and plasma density would be uniform over this volume because of the electrons' unimpeded access to the entire volume. This is in sharp contrast with earlier designs in which electrons were in constant interaction with the magnetic field. Thus, the required path lengths for primary electrons have been achieved using the fringe magnetic field while, at the same time, alleviating some of the problems of earlier designs by making the beam current density more uniform. To investigate the anticipated uniformity, Langmuir probe surveys of the operating discharge chamber were undertaken to determine plasma properties in both the nearly field-free volume of the discharge chamber and near the magnetic field boundaries. These surveys also permitted comparisons of the measured plasma density profiles with the extracted ion current density profiles. The Langmuir probe

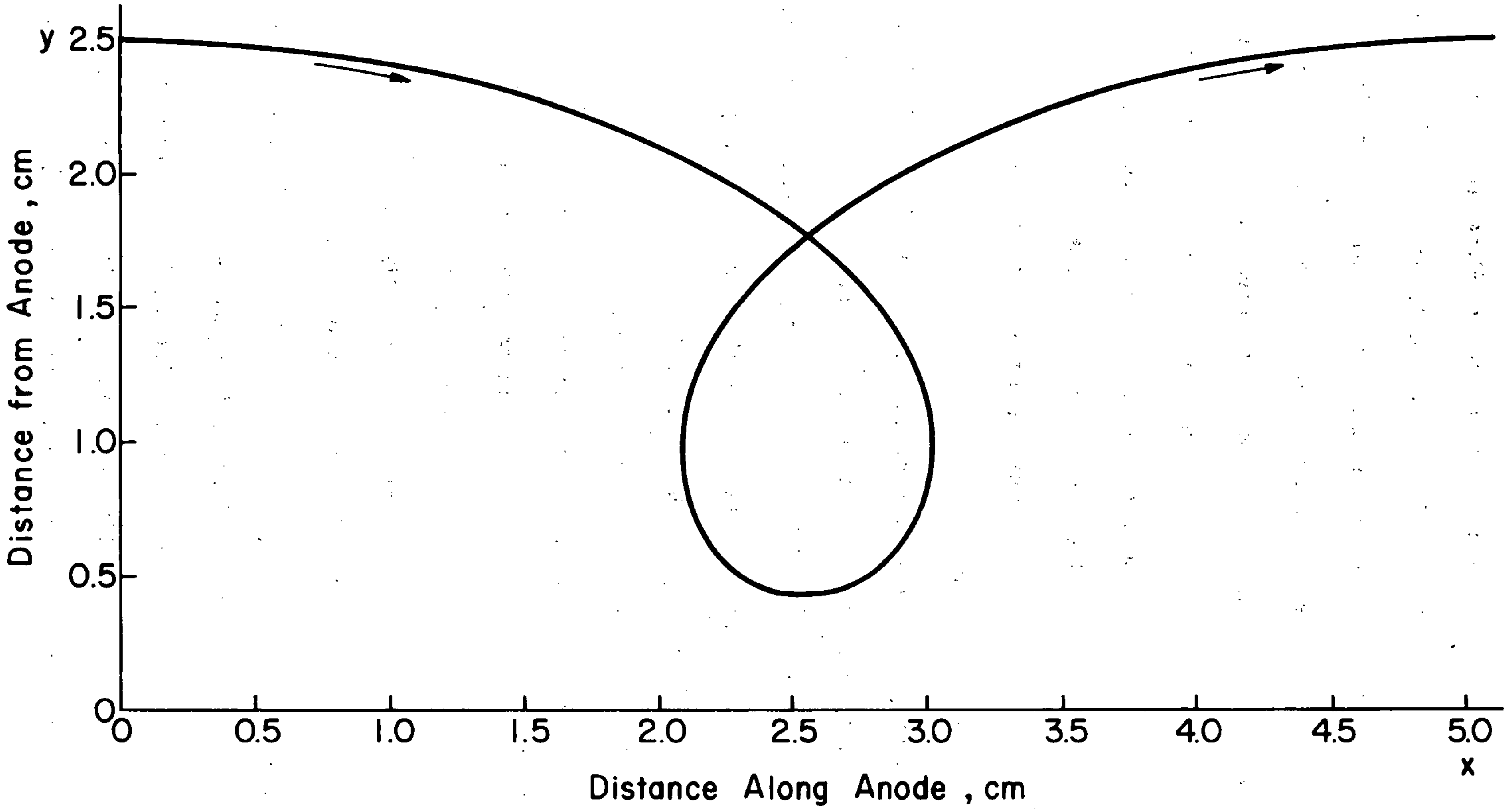

Figure 2-6. Computed electron trajectory in fringe field region.

consisted of a short, cylindrical segment of 0.64 mm diameter Ta wire. The exposed portion of wire for current collection was 2.5 mm long. The remaining length of wire was encased in alumina for insulation from the plasma. The probe was designed to move in an arc parallel to the accelerator system. The arc swept out by the probe was made to pass through the centerline of the discharge chamber. The probe could be moved through its arc from one side of the chamber to the other during source operation. The distance between the probe plane and the screen grid, however, could only be changed by adjusting the mechanical assembly between pumpdowns.

The probe potential was variable from -90V to +135V relative to the ion source body (cathode potential). The current drawn to the Langmuir probe was determined by monitoring the voltage drop across a precision sensing resistor. The probe current was displayed on an X-Y recorder as a function of probe bias potential. A typical maximum probe current for the voltages analyzed was about 10 mA or, at most, one percent or less of the total discharge current.

Some 60 Hz interference was encountered while taking early Langmuir probe data. The first attempt to solve this problem was with a filter network at the input to the X-Y recorder. Although the quality of the traces was somewhat improved with the addition of the filter, some interference still remained. It was suspected that the cathode heater was the source of this interference because the heater voltage was about 17 V_{rms}. This heater voltage was significant compared to the 50V discharge, so that plasma fluctuations might be expected to follow the heater voltage. The cathode supply was rebuilt to give DC with 1.8 percent ripple. Using this rebuilt heater supply, no significant level of noise was encountered with the high voltage off. When the thermionic neutralizer was turned on, some noise was observed until the background pressure was reduced to 2.5×10^{-4} Torr.

The probe was located in a plane about 1 cm upstream of the screen grid for the measurements shown in Fig. 2-7. Figure 2-7 shows measured densities of the two dominant electron populations in the discharge chamber. The probe data were analyzed using a numerical method similar to the one described by Beattie.[11] The numerical method assumes two electron populations, a priori, and finds the best fit to the data by adjusting the relative populations along with the primary energy and the Maxwellian temperature. A curve fitting technique was developed for reduction of Langmuir probe data obtained in these tests. This technique is related to the standard least squares methods, but does not suffer from the limitations in these standard methods that are encountered when the dependent variable covers a very wide range of magnitude. When the uncertainties in the data are independent of measurement magnitude, the standard methods give the correct answers. But the uncertainties in Langmuir probe data tend to be proportional to the absolute value of the measurement over most of the measurement range. The smaller values thus tend to have smaller uncertainties and should be so weighted in a curve fit; this is achieved by using relative errors scaled with respect to the dependent variable. The technique provides much better curve fits at small currents with only a slightly poorer fit at high currents in the same probe trace. A program has been written using this curve fitting technique. Use of this program appears to substantially reduce the "art" aspect of analyzing probe traces when compared to either graphical methods or previous programs.

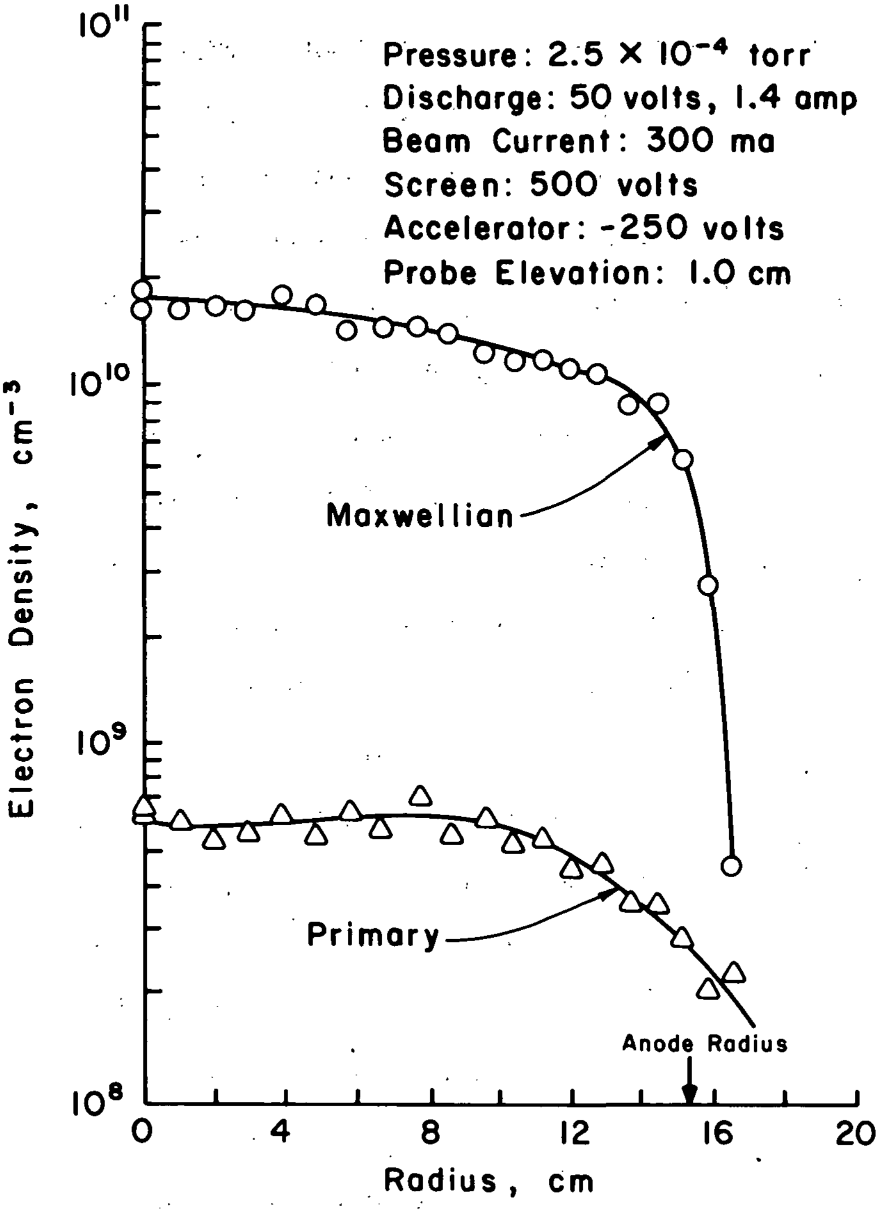

Figure 2-7. Primary and Maxwellian electron densities measured just upstream of the accelerator system as a function of radius.

The densities (Fig. 2-7) are fairly constant as the probe is moved from the center of the chamber toward the wall. There is a very sharp drop in plasma density as the fringe field is encountered, an indication that the multipole field is adequate for the desired electron containment. Measured Maxwellian electron temperature was found to be uniform at about 4 eV over the entire source radius. Plasma potential is uniform in the field-free region at about 56 V, with a several volt drop across the fringe field to the anode potential at about 50 V.

The current density in the ion beam was measured with Faraday probes. The current-collecting surfaces were 6.4-mm-diameter disks of molybdenum. These disks were located flush with a surrounding ground shield and biased at -25 V relative to ground to reflect electrons. The density profiles shown in Fig. 2-7 qualitatively agree with the experimentally measured beam current density profiles of Fig. 2-8.

The profile of Fig. 2-8 were taken using dished molybdenum grids and are interesting in that they show peaks near the outer edge of the ion beam. If these peaks reflected actual variations in discharge-chamber plasma density, then they should have also been evident when a set of flat carbon grids was used but no peaks were seen then.

The peaks are believed to result from the dished shape of the molybdenum grids, although the specific process is not clear. For example, the spacing between dished grids is known to vary across the beam diameter at operating temperatures. Despite this variation, the relative displacement of screen and accelerator holes to deflect the beamlets in the axial direction was made a linear function of distance from the beam center. This discrepancy would be expected to produce

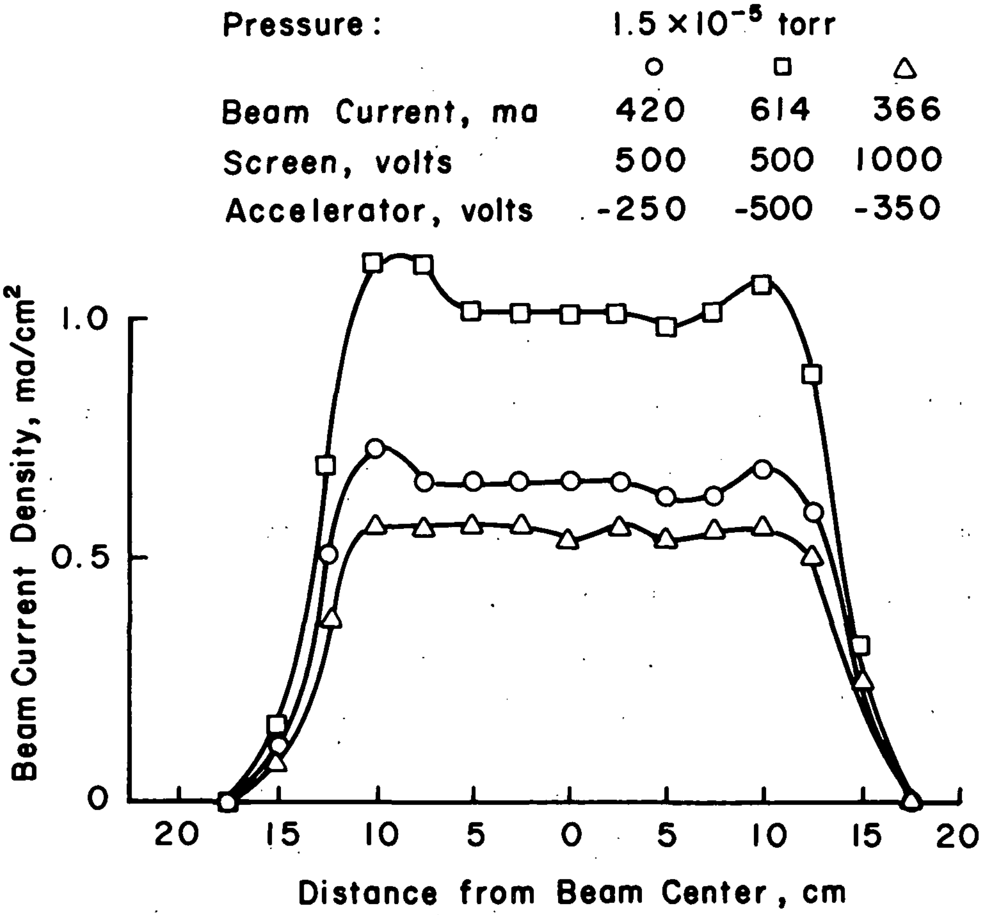

Figure 2-8. Beam current density profiles measured for the 30-cm ion source.

some ion-optic aberration. Another possible cause of the peaks is in the deceleration region downstream of the accelerator. The decelerating electric field is nearly normal to the local dished grid surface, but the ion trajectories are at an appreciable angle to this normal near the edge of the beam. The relative directions of electric field and trajectories could therefore cause further deflections near the edge of the beam; which could cause the observed peaks.

Multipole Discharge Limitation

Discharge chamber operation in the 30-cm multipole was found to depend critically on the anode configuration used. While operating in a large vacuum facility at low background pressure, the 30-cm source was wired so that each of the ten anodes could be individually switched from anode to screen potential. Thus, any combination of anodes could be switched off to observe the effects of anode configuration on source operating characteristics.

Switching any single anode, or any pair of anodes, to screen potential changed the beam current extracted but allowed the source to continue operating. Switching off all possible combinations of three anodes allowed the source to continue operating with one exception, when anodes #5, #7, and #9 were switched off together, the discharge was extinguished at both 900 ma-equiv. flow and at 1500 ma-equiv. flow. The anodes are numbered sequentially starting with #1 as the smallest center anode at the upstream end and with #10 closest to the grids. With only a few exceptions turning off almost any four anodes together would extinguish the discharge.

Discharge losses were observed to increase as the number of anodes in operation decreased. Figure 2-9 shows the increase in discharge loss with anodes #1, #2, and #3 off and with anodes #8, #9, and #10 off. The combined length of anodes #8, #9, and #10 is much longer than the combined length of #1, #2, and #3. The discharge loss is seen to be much higher with the three longer anodes off than with the three shorter anodes off.

The only major change in source operating conditions that occurred, as various anodes were turned off while maintaining a constant discharge current, was a decrease in beam current. To illustrate the correlation between these effects, the extracted beam current was plotted as a function of the fraction of total available anode length drawing current. Figure 2-10 shows reasonable correlation between these two parameters.

The foregoing observations indicate possible limitations to the scaling possibilities of multipole designs to much larger ion sources or thrusters or to further simplification of the design by eliminating some of the anode structure. To gain further understanding into the limiting process the source was operated with various anode configurations while probing the bulk plasma properties with a Langmuir probe. The plasma was initially close to anode potential with all the anodes connected. As a sufficient number of anodes were disconnected, the plasma assumed a potential substantially negative of the anodes. This effect is shown with minor differences in Figs. 2-11(a) and 2-11(b). Figure 2-11(a) was obtained at close to the minimum discharge voltage for each anode configuration, while Fig. 2-11(b) was obtained about 10 V higher. The two working gas densities shown in each figure cover

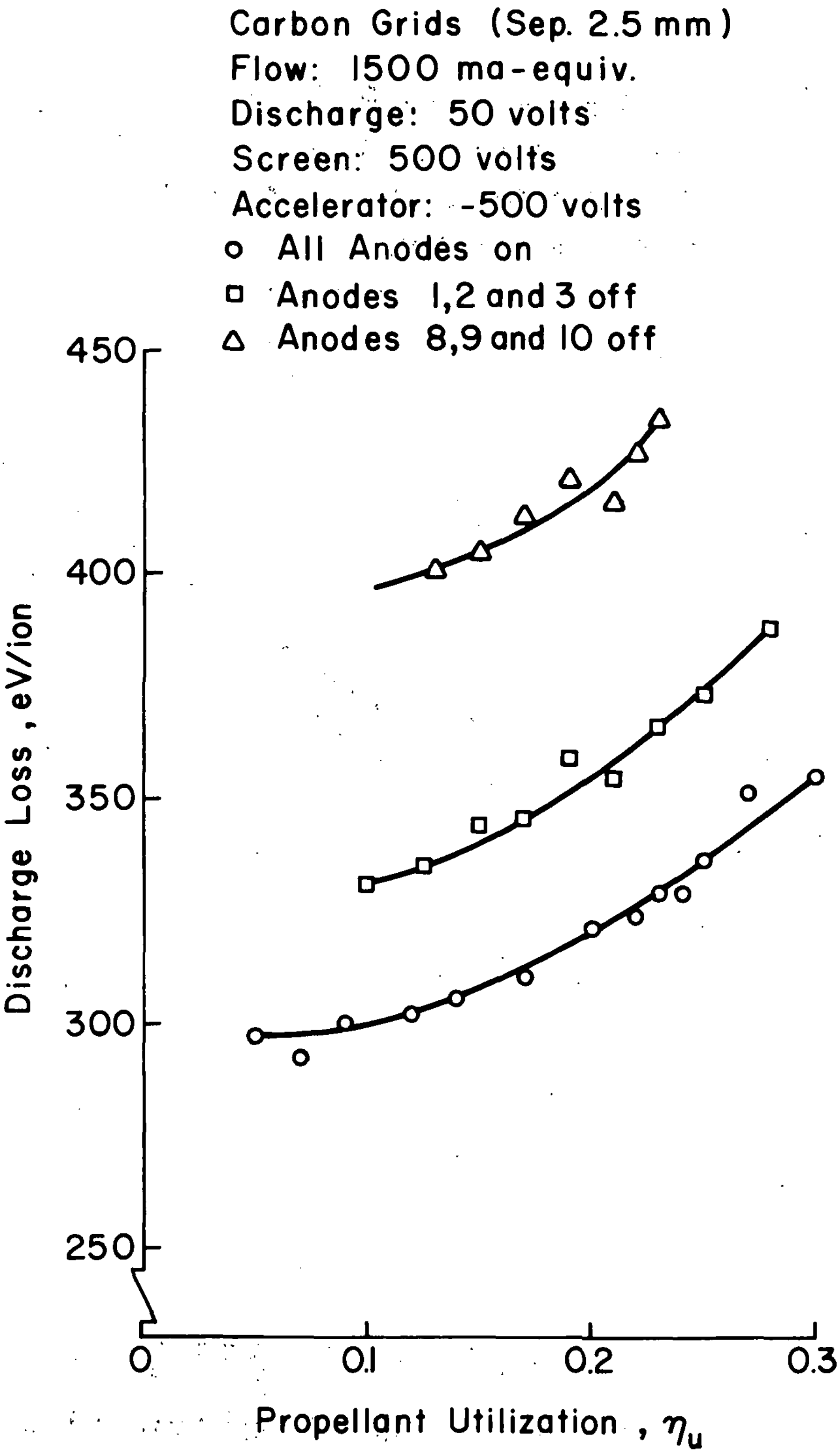

Figure 2-9. Discharge loss variations with anode configuration.

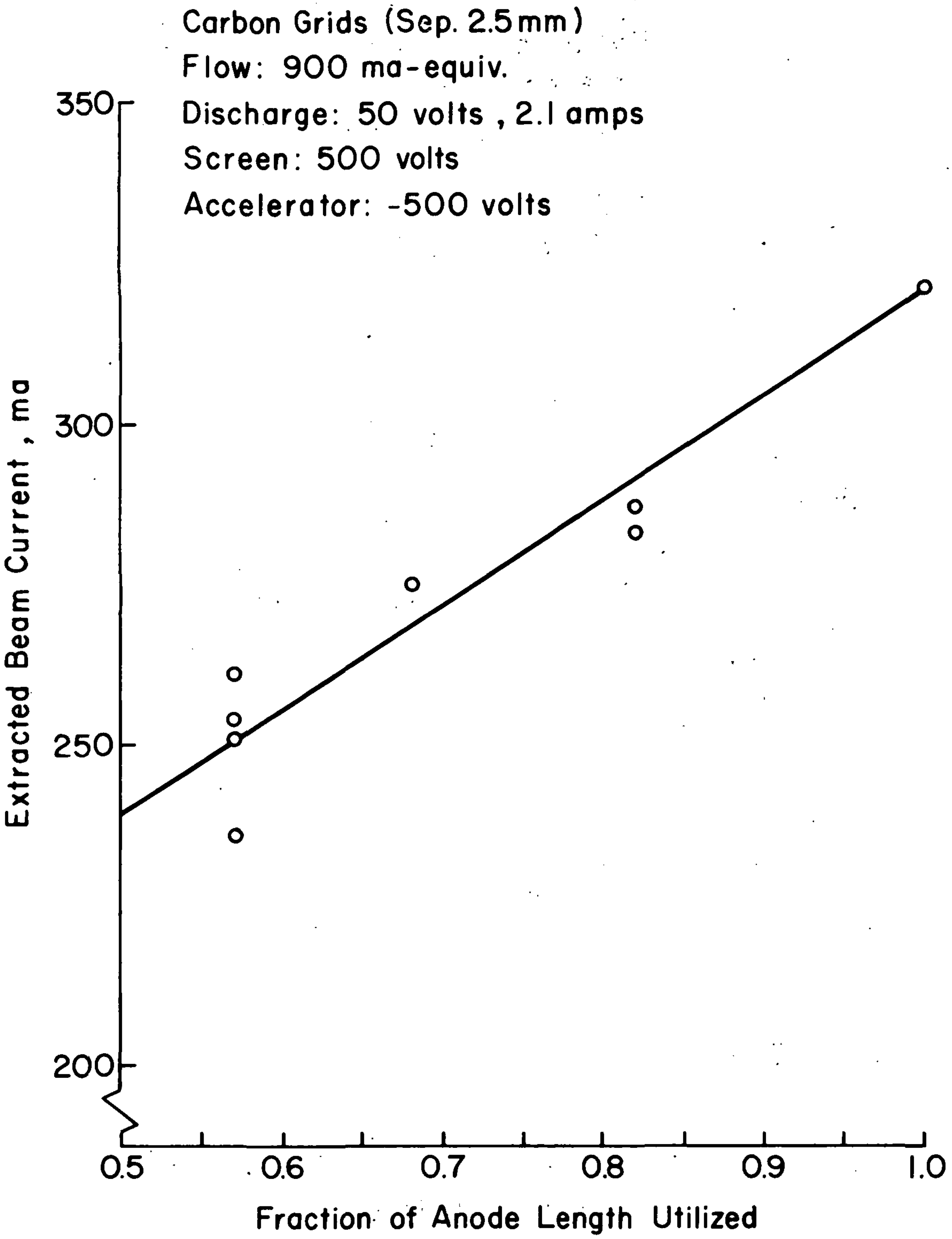

Figure 2-10. Correlation of extracted beam current with anode configuration.

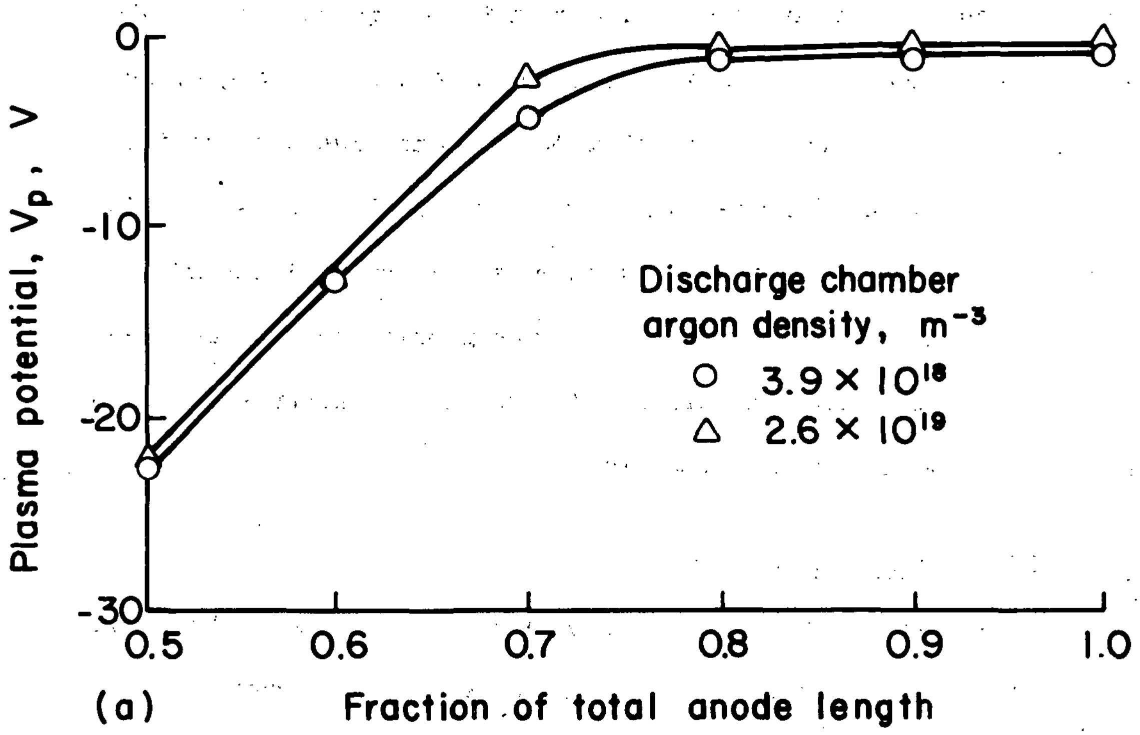

Near the minimum discharge voltage.

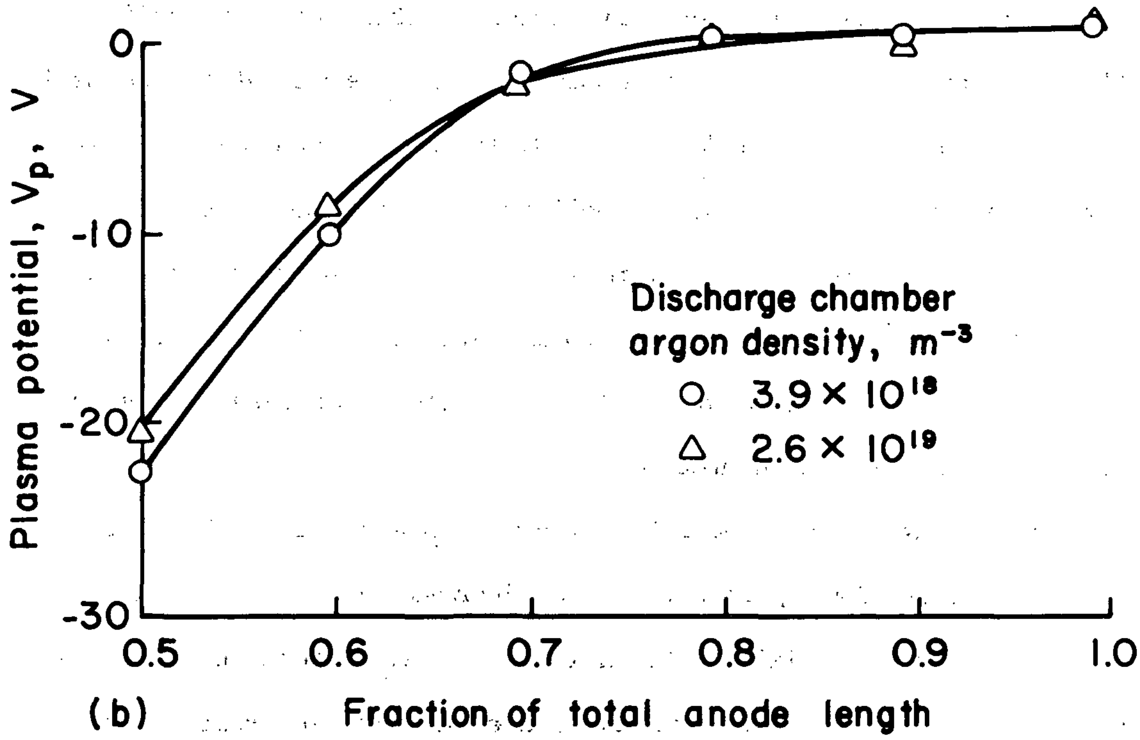

About 10 V above the minimum discharge voltage.

Figure 2-11. Plasma and anode parameters for the 30-cm chamber.

the usual range of interest for source or thruster operation. When the effective anode area (proportional to active anode length) is reduced below an approximate critical value, the plasma potential apparently must become increasingly negative of the anodes to maintain the desired electron current to the anodes. Because electron diffusion can result from both potential and density gradients, the added contribution of the potential gradient diffusion is the amount required to compensate for the reduced anode area.

Thermal Electron Diffusion Model

The electron current to a discharge-chamber anode can be limited by the diffusion of electrons through the magnetic field above the anode. This condition can be thought of as either an anode area limitation or a limitation on current (or current density) to that anode. The current approach is more convenient for derivation of the effect, while considering it as an area effect appears more useful in discussing experimental performance. The effect is discussed in connection with the multipole magnetic field. The effect, though, appears to be involved wherever electrons must cross magnetic field lines to reach a discharge-chamber anode. The development of this model for the multipole magnetic-field configuration is facilitated by the ease with which that configuration can be analyzed.

Before presenting the model, it should be emphasized that the anode area involved may, or may not, be a physical area. The electron mobility along magnetic field lines is much greater than the mobility across field lines. The effective anode area is therefore that area from which electron can be drained from the discharge plasma by moving along field lines to reach the anode.

Electrons emitted from the cathode, together with electrons liberated in the ionization process, must diffuse to the anodes to sustain a discharge current. In doing so, the electrons must cross magnetic fields sufficient to contain electrons of primary energy. The basic equation for electron diffusion in the presence of voltage and density gradients is

$$\vec{\Gamma} = -\mu\, n_e\, \vec{E} - D\vec{\nabla} n_e \tag{2-9}$$

where $\vec{\Gamma}$ represents the particle flux of electrons, n_e is the electron number density, and μ and D are the electron mobility and diffusion coefficients respectively. The mobility and diffusion coefficients are related by the Einstein relations,[12]

$$\mu = e\, D/kT_e \tag{2-10}$$

where e is absolute magnitude of the electronic charge, k is Boltzmann's constant and T_e is the electron temperature. The classical diffusion coefficient in the absence of (or parallel to) a magnetic field is[12]

$$D = kT_e/m_e\nu_e \tag{2-11}$$

with m_e the electron mass and ν_e the electron collision frequency.

The classical diffusion coefficient normal to a magnetic field is[12]

$$D = D/(1 + \omega_c{}^2\tau^2) \tag{2-12}$$

where ω_c is the electron cyclotron frequency and τ is the mean time between collisions ($\tau = 1/\nu_e$). This reduces in the strong field limit of $\omega_c\tau >> 1$ to

$$D = D/\omega_c^2\tau^2 = kT_e m_e \nu_e/e^2B^2 \ . \qquad (2\text{-}13)$$

There is also a drift velocity at right angles to the applied field $\vec{E}$. For the last diffusion coefficient to be observed, this drift must take place without generating an additional electric field. Anodes and pole pieces that are closed loops meet this condition.

Experimental measurements of electron diffusion across a magnetic field with $\omega_c\tau >> 1$ usually correspond to larger diffusion coefficients than given by Eq. (2-13), often by orders of magnitude. These larger values are attributed to "anomalous" or "turbulent" diffusion. A simple and well known semiempirical approach to turbulent electron diffusion was given by Bohm.[13] The Bohm diffusion coefficient given in later publications[14,15] has a slightly different numerical coefficient and is

$$D_B = kT_e/16\ eB \ . \qquad (2\text{-}14)$$

Bohm diffusion varies as $1/B$, while classical diffusion for the same strong field condition varies as $1/B^2$. In fact, the Bohm value of diffusion is obtained if we assume that turbulence increases the effective collision frequency to $\omega_c/16$. Despite the simplicity of the Bohm diffusion coefficient, it effectively correlates experimental observations over a wide range of conditions.[15]

It should be noted that the diffusion of interest herein is primarily of Maxwellian or thermal electrons. Whether we are concerned with the coulomb collisions of classical diffusion or the collective collisions of turbulent diffusion, the lower energy electrons have almost all of the collisions and diffuse across a magnetic field more readily than the higher energy primary electrons.

The diffusion condition for anodes of most interest is the maximum diffusion that can be obtained without the assistance of a forward electric field, which would result if the anodes were substantially more positive than the discharge-chamber plasma. A reasonable assumption for this limiting condition appears to be zero electric field in the region of interest close to the anodes of a multipole discharge chamber. This condition of nearly uniform potential in the diffusion region has been observed experimentally, with the only nonuniform region a jump of several volts at the anode. Using this uniform potential assumption together with the Bohm diffusion coefficient, Eq. (2-9) can be written in one dimension as

$$\Gamma = -D_B \, dn_e/dx \, . \tag{2-15}$$

In terms of current density, this becomes

$$j = e \, D_B \, dn_e/dx \, . \tag{2-16}$$

With the substantiation of Eq. (2-14), we find

$$j = \frac{kT_e}{16B} \frac{dn_e}{dx} \, . \tag{2-17}$$

Prior knowledge of the variation of n_e with x is not assumed. Instead, the near constancy of current density in the diffusion region is used, which results from the small thickness of that region compared to chamber diameter and the small fraction of total ionization therein. Noting too that the electron temperature is also nearly constant in the diffusion region, all the constants of Eq. (2-17) are collected on the left side to obtain

$$\frac{16j}{kT_e} = \frac{dn_e}{Bdx} . \tag{2-18}$$

The detailed variation of n_e with x is not known, but the differential expressions may be replaced with expressions integrated over the depth of the fringe field to the anode edge where the electron density falls to zero.

$$\frac{dn_e}{Bdx} = \frac{n_e}{\int Bdx} , \tag{2-19}$$

where $\int Bdx$ is the same integral that is involved in the containment of high-energy primary electrons. With this substitution, the electron current density becomes

$$j = \frac{kT_e\, n_e}{16\int Bdx} . \tag{2-20}$$

In calculating this current density, the fringe field area above the anodes is important, while the projected area of the anodes is not.

As mentioned at the beginning of this section, this is because the diffusion coefficient parallel to the magnetic field is so much greater than that normal to the field. The absence of any significant effect of anode projected area has also been established experimentally.[15]

An additional correction can be made for the variation in area normal to the electron current j. The magnetic field lines close to the inner anode edges follow paths nearly parallel to the smoothed outer surface of the discharge chamber (see dashed line in Fig. 2-12). Farther away from the anodes, though, the field lines follow longer looping paths. This variation in field line length results in a similar variation in area normal to the diffusing electron current. A numerical integration through increments of $\int Bdx$ can be used to correct for this area variation. An applicable equation is

$$j = \frac{kT_e}{16} \frac{\sum_{i=1}^{N} \Delta n_{e_i}}{\sum_{i=1}^{N} (\Delta \int Bdx)_i \, d/\ell_{B_i}} , \tag{2-21}$$

where Δn_e is the increment in electron density required to drive the current j through an increment in magnetic field integral $(\Delta \int Bdx)_i$ with an "area" ℓ_{B_i}/d where ℓ_{B_i} is the length of the i^{th} field line. The ratio ℓ_{B_i}/d is effectively a length because a unit width is assumed in the direction normal to both ℓ_{B_i} and j. The local current density thus equals j where $\ell_{B_i}/d = 1$. Solving Eq. (2-21) is facilitated if one recognizes the clear analogy with current flow through resistors connected in series. In this analogy, the density increment is analogous to the voltage across a resistor, while the resistance is

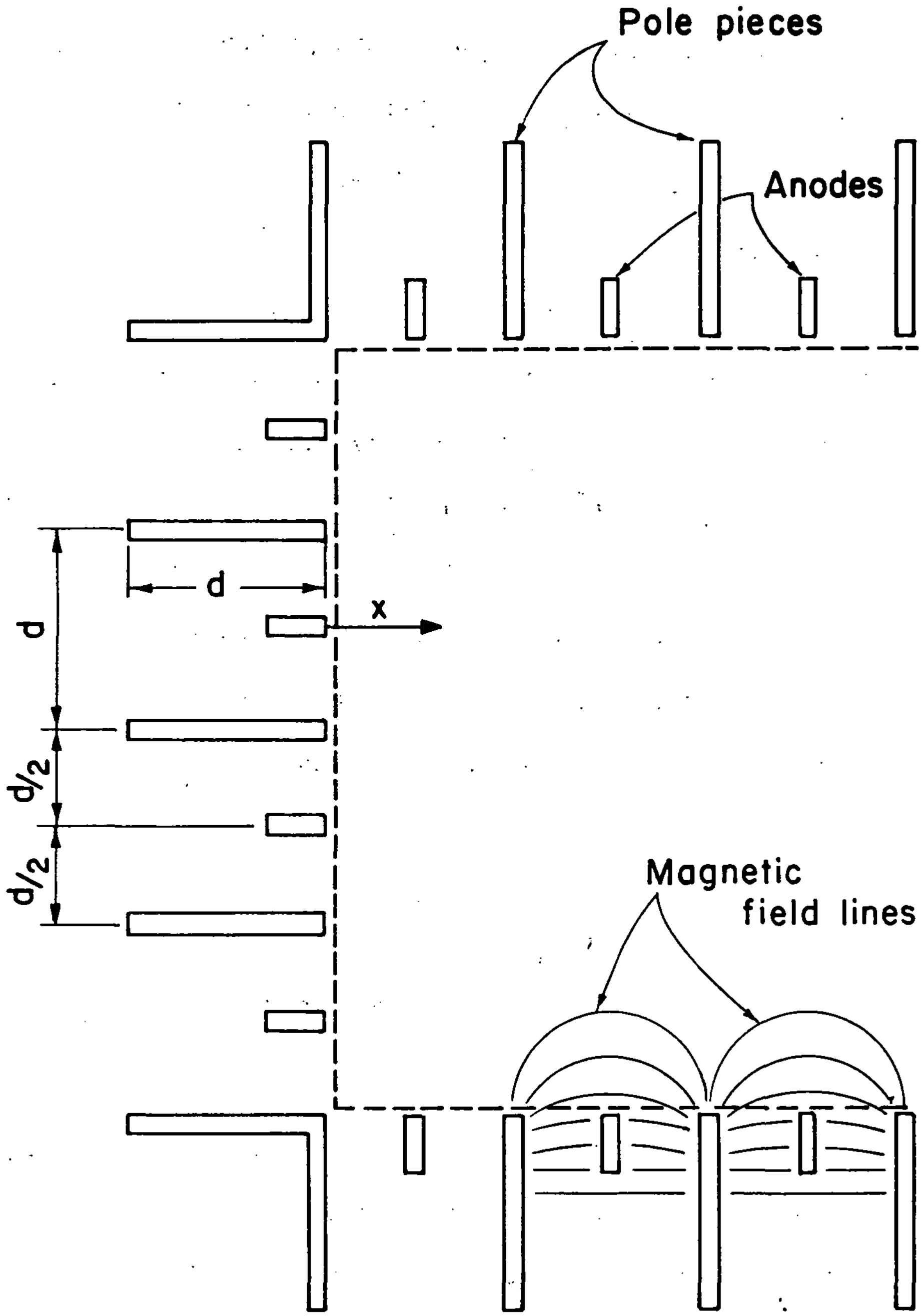

Figure 12. Multipole discharge chamber. Dashed line shows assumed outer surface of discharge chamber.

analogous to $(\Delta \int B dx)_i \, d/\ell_{B_i}$. Using this analogy, it can be shown that an effective overall value of ℓ_{B_i}/d is

$$\frac{\ell_{B_{eff}}}{d} = \frac{\int B dx}{\int B \frac{d}{\ell_B(x)} dx} \tag{2-22}$$

where the integral is over the region between the anode and the nearly field-free main volume of the discharge chamber. We can use a curve fit for the variation of B with distance similar to the one obtained previously (Eq. 2-8),

$$B = B_{max} \exp[-1.5 \, (x/d + 1/2)^2] \; ,$$

where x is indicated in Fig. 2-12. Assuming parabolic arc paths for field lines between the ends of pole pieces, one can then find by integrating Eq. (2-22) that the area correction is equivalent to

$$j \approx \frac{kT_e n_e}{13 \int B dx} \tag{2-23}$$

where j is based on the area indicated by the dashed line in Fig. 2-12. Equation (2-23), then, can be used to find the maximum electron current that will diffuse to the anodes without making the anodes more positive than the discharge-chamber plasma. In view of the relatively small difference between Eqs. (2-20) and (2-23), a more accurate correction for the area affect does not appear necessary. Also, a separate correction for corner pole pieces, which have a slightly different variation of B with x, is not required.

The theoretical electron currents to the anodes were calculated using Eq. (2-23), the effective anode areas for the active anodes, and plasma properties from a centrally located Langmuir probe. The experimental anode currents were assumed to be the sums of discharge and beam currents. The ratios of experimental-to-theoretical anode currents were then plotted in Figs. 2-13(a) and 2-13(b). Basing the calculations on the plasma properties led to considerably more scatter in Figs. 2-13(a) and 2-13(b) than in Figs. 2-11(a) and 2-11(b), enough scatter so that only one curve is shown, Still, the trends appear clear. The anode current ratio, J_{exp}/J_{th}, becomes greater than unity at close to the anode fraction where the plasma becomes negative relative to the anodes.

Operation with a plasma significantly negative of the anodes is believed to be marginally stable, or even unstable. The reasons for such a viewpoint are the absence of such data in thruster literature,* and the difficulty of obtaining such data in this investigation. The data of Figs. 2-11 and 2-13 were obtained by using rheostats to

---

*The only description of a plasma significantly negative relative to the anode is the cesium multipole of Moore.[5] A very high magnetic field strength was used in this early multipole design. This high field strength apparently prevented sufficient electrons from diffusing to the multipole anodes, which roughly resembled the multipole anodes of Fig. 2-12. A "plasma anode" (a narrow strip of metal across the discharge chamber, unprotected by a magnetic field) was therefore introduced to provide a path for the required electron current. Stable operation with the plasma negative relative to the multipole anodes was obtained by also operating the plasma anode negative of the multipole anodes. The plasma anode, of course, operated close to plasma potential. Similar operation may have been used by Ramsey,[6] but insufficient description was included for the determination of the potential bias between plasma and multipole anodes.

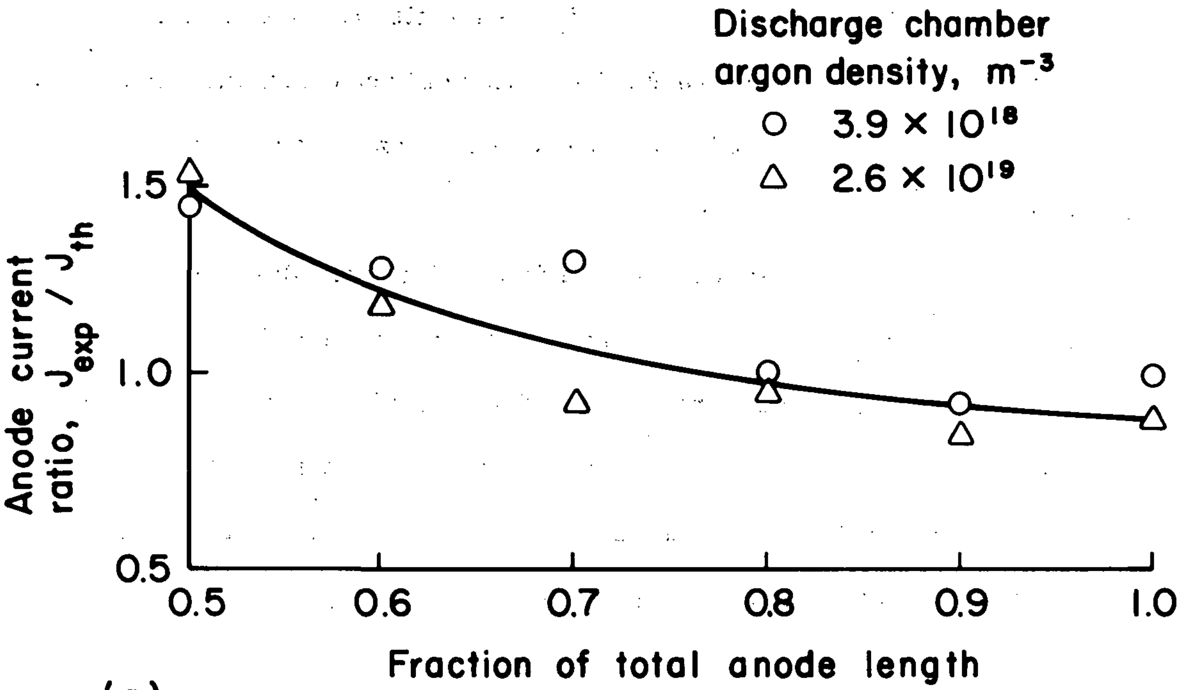

(a) Near minimum discharge voltage.

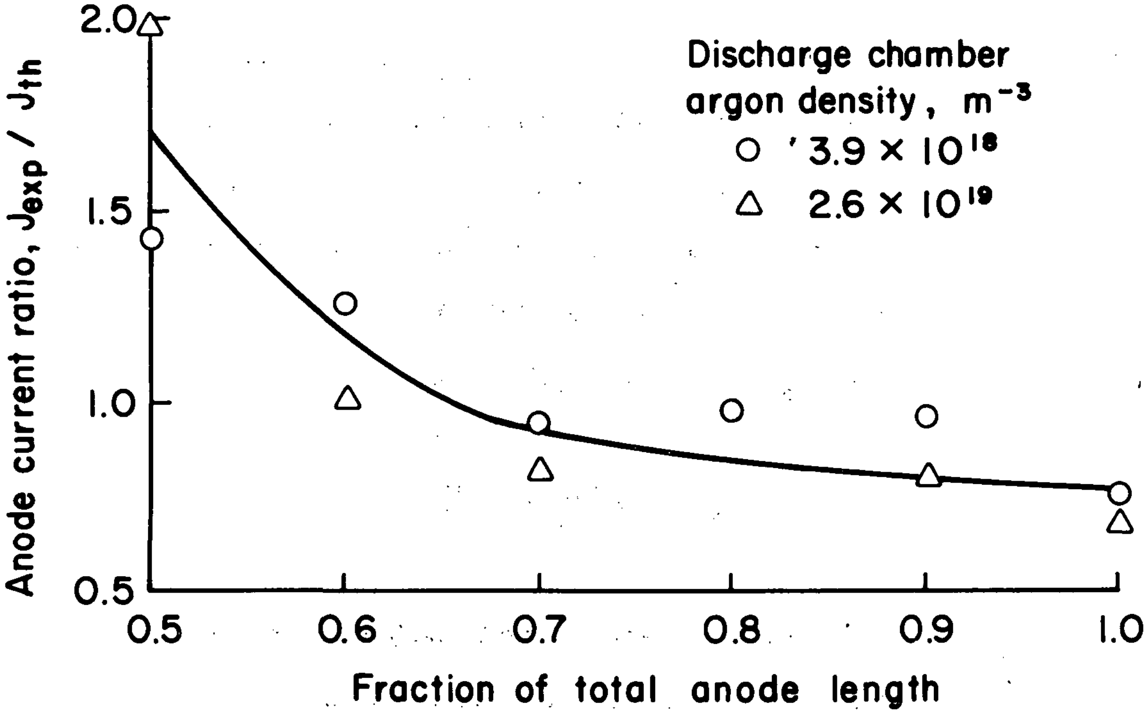

(b) About 10 V above minimum discharge voltage.

Figure 2-13. Experimental to theoretical anode current ratios.

gradually disconnect anodes, thereby minimizing switching transients. Without these rheostats, switching of anodes without extinguishing the discharge was reliable only above ∿70% of total anode length. That is, it was reliable only at anode lengths where the plasma was not significantly negative of the anodes.

Other tests were also conducted with both 15-cm and 7.5-cm multipole discharge chambers (configurations described in Ref. 17 and 18). Because plasma probe data were not obtained with these smaller discharge chambers, it was necessary to estimate electron temperature from other tests and electron density from beam current. To the latter end, the beam current extracted can be expressed as

$$J_b = A_{scr}\, n_e\, v_B\, e\ , \qquad (2\text{-}24)$$

where n_e is the electron/ion density, v_B is the Bohm critical sheath velocity, e is the absolute electronic charge, and A_{scr} is the effective open screen area for extraction. This area can be somewhat above or below the geometrical open area, but the latter should be a good approximation. Replacing the Bohm velocity with the equivalent expression $(k\,T_e/m_i)^{½}$, Eq. (2-24) becomes

$$J_b = A_{scr}\, n_e\, e(kT_e/m_i)^{½}\ . \qquad (2\text{-}25)$$

Using K_{ab} as the anode-to-beam current ratio, the anode current required to generate the ion beam can be written as

$$J_a = K_{ab} A_{scr} n_e\, e(kT_e/m_i)^{½}\ . \qquad (2\text{-}26)$$

From Eq. (2-23), the current permitted to diffuse to the anode (or anodes) without the anode becoming substantially more positive than the discharge-chamber plasma is

$$J_a = A_a \, kT_e \, n_e / 13 \int B dx \ , \tag{2-27}$$

where A_a is the anode area. Equating these two anode currents to obtain the minimum anode area for stable operation,

$$A_a = 13 \, K_{ab} A_{scr} e \int B dx / (kT_e m_i)^{\frac{1}{2}} \ . \tag{2-28}$$

This, then, is the relationship that can be used in the absence of plasma probe data.

In earlier tests of the 15-cm discharge chamber with argon[16] the mean electron temperature ranged from about 5 to 15 eV. Using 10 eV as a typical value, together with measured values for the magnetic field integral, screen open area, and anode-to-beam current ratio, minimum discharge voltages* were used with Eq. (2-28) to estimate anode area. For a 24 magnet configuration of the 15 cm chamber an anode area of 430-510 cm^2 was estimated. The measured anode area was 471 cm^2, which is in excellent agreement with the estimates from Eq. (2-28).

---

*The minimum discharge voltage, where the discharge is extinguished, is believed to correspond to the anode diffusion limit. The reason that the limit is approached in this condition is that the discharge losses per ion are roughly constant while the discharge voltage decreases toward the limit. As a result, the ratio of discharge-to-beam current, K_{ab}, increases as discharge voltage drops. When K_{ab} increases to a large enough value, at the minimum voltage, the required anode area will exceed the actual area anode and the discharge will extinguish.

Similar minimum discharge voltage tests were conducted with the 7.5-cm discharge chamber. Inasmuch as electron temperature generally increases as thruster size becomes smaller, an electron temperature of 15 eV was felt to be a better estimate for this thruster size. With this temperature and similar measured values as for the 15-cm tests, Eq. (2-28) indicated an anode area of 70-130 cm^2. The measured anode area was 118 cm^2, which again is in excellent agreement.

This diffusion model also appears applicable to general performance trends. As an example, the minimum permissible discharge voltage tends to increase as neutral pressure in the discharge chamber is decreased. We also know that, in the operating range of interest, the discharge losses tend to increase as neutral density is decreased. This increase would result in an increase in required anode current at constant discharge voltage, which, in itself, would result in an increased requirement for anode area. If this increased anode area is not available, then the minimum discharge voltage increases to where the anode current becomes consistent with the anode area available.

Application to Design

The electron diffusion theory of this section can be applied to design problems. An obvious application is to estimate the minimum required anode area for expected operating conditions. Less obvious is the evaluation of other multipole magnetic field configurations. One example of a possible design is shown in Fig. 2-14(a). This flux concentrator design is a possible means of reducing the stray magnetic flux, thereby reducing the required magnet weight. From the model however, the flanges that serve to concentrate the flux will also serve

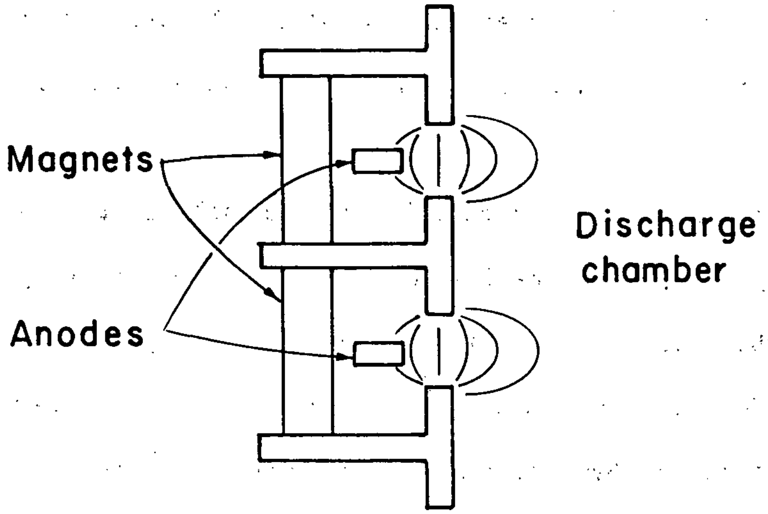

(a) Flux concentration

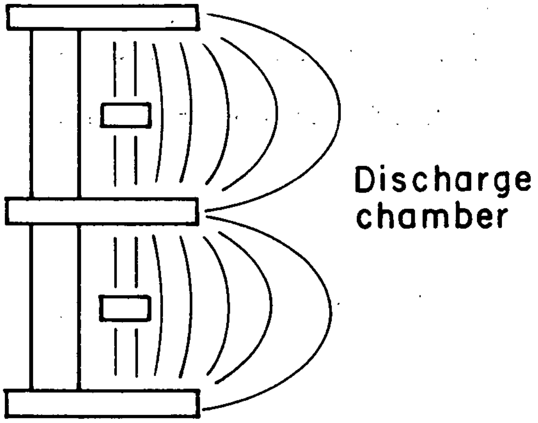

(b) Recessed anodes

Figure 2-14. Possible multipole magnet and pole-piece configurations.

to reduce the effective anode area. Inasmuch as the flux integral above the anode is fixed by the need to contain high velocity primary electrons, this integral will need to be about the same for both the regular design and the design of Fig. 2-14(a). The reduction of magnet weight would thus have to be balanced against the loss in effective anode area.

Another approach, the recessing of anodes behind the pole pieces, is shown in Fig. 2-14(b). The model clearly indicates that the shape of the field above the anodes is of secondary importance. Except for corner locations, the anodes have in the past been made flush with the inside edges of the pole pieces. By recessing the anodes, it should be possible to reduce the number of magnets for the same magnetic field integral above the anodes.

The diffusion of electrons through the magnetic field above multipole anodes has been studied in detail. The data are consistent with Bohm diffusion across a magnetic field. The model based on Bohm diffusion is simple and easily used for diffusion calculations.

III. ENERGETIC BINARY COLLISIONS IN RARE GAS PLASMAS

Energetic binary collisions become important in plasmas or in ion beams where high voltages (several hundred or a few thousand eV) are introduced to accelerate ions toward a target within a plasma or to form a beam. High voltage, taken in this context, is meant to imply particle energies very much greater than thermal energies, usually three to five orders of magnitude greater, while, at the same time, not approaching the extremely high energies utilized in particle accelerators for nuclear research. Interest in these collision cross sections arose primarily in connection with experimental work involving the propagation of ion beams used for sputtering and processes occurring within diode plasma sputtering devices.[1,2] Thus, although the cross sections obtained should also be of interest in other areas, the cross sections obtained herein are largely described in terms of their impact on the understanding of these particular experimental sputtering applications as representative systems. Energies of several hundred eV are typical of those employed in diode sputtering and in ion beam devices.[3] At such energies, interaction cross sections are found to differ sharply from their values at very low or thermal energies.[4] It is this strong dependence on energy that is of most interest because the relative importance of certain interaction processes can be enhanced or diminished by moving from one realm of energy to another.

The plasmas and beams generated in sputtering devices are typically derived from rare gases, with Ar being the most common by far, primarily because of its low cost. Other, more reactive gases are employed occasionally to achieve special effects due to chemical reactions in addition to the physical sputtering effect of a directed ion beam.[5] This work will be restricted to consideration of Ar, Kr, and Xe for momentum and energy transfer calculations and to Ar for the discussion of charge exchange.

Ion Beam Interactions

Effective application of ion sources to various ion milling, *reactive ion etching and sputter deposition processes requires* characterization of the major interactions of the ion beam with the background environment through which it propagates. The major interaction processes are: (1) resonance charge exchange between fast ions and slow moving or thermal neutrals, and (2) momentum transfer from fast moving neutrals to slow moving neutrals. A variety of other processes can take place as well but are found to be quantitatively much less significant than these two.

For example, a small fraction of ions generated in a discharge chamber are doubly ionized. Depending on the particular ion source and operating conditions, the fraction of doubly ionized atoms extracted with the beam ranges from less than one percent to several percent.[6] In sputtering applications, double ions would strike the substrate with twice the energy of single ions. The effect of this doubly ionized fraction can be significant where depth of damage is a critical factor, but is otherwise a negligible process.[7] As another example, while it is recognized that free electrons will generally be present in plasmas and propagating beams, their collisional effects may usually be neglected. Electrons are important for space-charge and current neutralization of an ion beam but do not otherwise enter significantly *into reactions. Electron masses are of the order of* 10^{-5} *of the ion* or atom masses of interest so that in the usual range of background densities the energy and momentum losses from beam particles to electrons are negligible. In addition, the injection energy of electrons from a neutralizer is too low to cause significant ionization.[8] The process of recombination of electrons with ions can be neglected compared to charge transfer for ion neutralization because the cross section for this process is several orders of magnitude smaller than charge exchange cross sections.[9]

As a final example, the momentum transfer from ions to background neutrals is of relatively lesser importance because: (1) the ion-atom collision cross section is somewhat less than for atom-atom collisions, and (2) the charge exchange process has a much larger cross section than the momentum transfer process. Thus, the high-velocity beam particles involved in significant momentum transfer processes tend to be neutral particles that result from ion-atom resonance charge exchange rather than the ions themselves.

The background plasma through which an ion beam propagates is largely the result of charge exchange between beam ions and the neutral background gas. In addition, neutral working gas flows out of the discharge chamber through the apertures in the accelerator system and produces a local density increase in the neutral background gas near the ion source. There is another local density increase in the neutral background gas at the target due to beam ions that have given up their directed energy to the target and have been neutralized by recombination with electrons at the target or substrate, thus contributing to the neutral gas background in the vacuum chamber. Aside from the local pressure maxima mentioned above, pressure in the vacuum chamber is governed by the speed of the pumping system relative to the total flow rate of working gas into the discharge chamber.

Using known characteristics of practical ion sources, vacuum systems, and working gases some estimates can be made of the various deviations of actual beam properties from the ideal case of no beam-background interactions.

Charge Exchange

An ion and a neutral atom of the same element can undergo resonance charge exchange wherein an electron is transferred from the atom to the ion, e.g., $Ar_f^+ + Ar \rightarrow Ar_f + Ar^+$ (the subscript f indicating a fast-moving particle relative to the other reactant). If a fast ion undergoes charge exchange with an atom of thermal neutral gas, the result is a slow ion and a fast neutral atom possessing essentially the original ion energy. Resonance charge exchange can be a significant process in the propagation of energetic ions or ion beams through typical background gas pressures. The resonance charge exchange cross section can be looked upon as a reflection of the quantum mechanical probability amplitude for an electron to be localized near a second ion in the neighborhood of the one to which it is originally bound.

Several workers have reported experimental data for Ar resonance charge exchange in various energy ranges. A few theoretical studies have also explored the expected behavior of the charge exchange cross section as a function of relative energy. A functional form for the total cross section for resonance charge is given by Iovitsu and Ionescu-Pallas[10] and Rapp and Francis.[11] Their expression for the form of the total cross section variation for resonance charge exchange Q_r is

$$Q_r = (a - b \ln v)^2 , \qquad (3\text{-}1)$$

where a and b are constants to be determined using empirical data and v is the relative speed of the atom and ion. This form for the total resonance charge exchange cross section has been shown experimentally by Zuccaro[12] to hold for Hg.

A curve of the form of Eq. (3-1) was fit to experimental data for Ar from Dillon, et al.[13] and Hasted[14] using a least squares regression technique. The constants a and b were determined for Ar resonance charge exchange:

$$a = 1.51 \times 10^{-9}$$

$$b = 9.53 \times 10^{-11}$$

where Q_r in m^2 and v in m/sec. Other experimental data were available from Potter[15] that, however, were in disagreement with both Dillon, et al.[13] and Hasted;[14] thus, these data were not included in the fit to Eq. (3-1). Experimental data obtained by Kushnir, et al.[16] was also found to be in fair agreement with the work of Hasted[14] but existed at only a few discreet energies in the range of interest.

Figure 3-1 is a plot of the total resonance charge exchange cross section for Ar as a function of relative energy using this best fit for

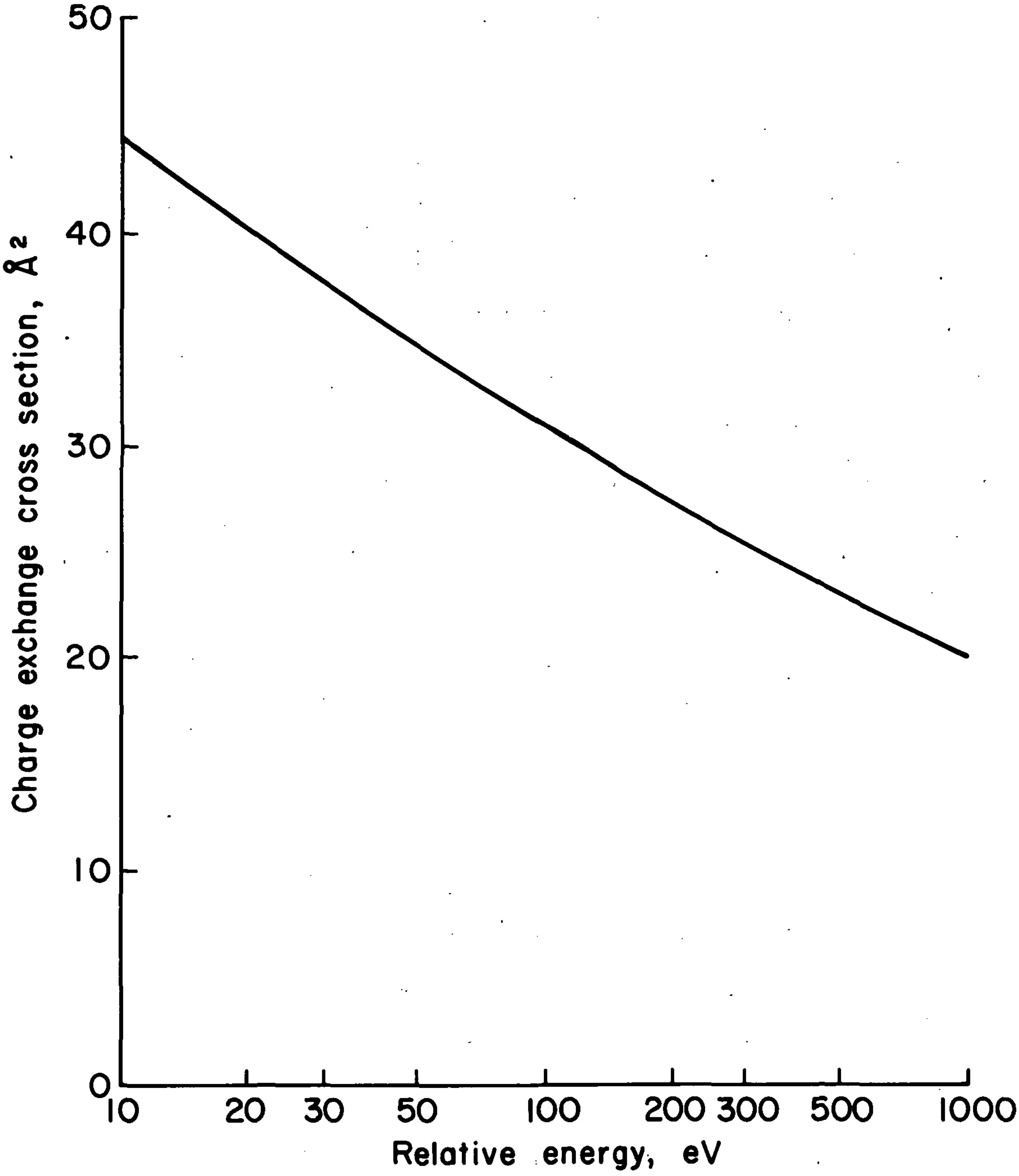

Figure 3-1. Total resonance charge exchange cross section for argon as a function of ion energy.

the function. At 500 eV, a typical beam energy, the charge exchange cross section is about 23 Å^2. The cross section decreases monotonically with increasing relative energy but the decrease is not rapid; the cross section is reduced by about half as the relative energy increases fifty-fold from 20 eV to 1000 eV. In addition, because this is a fairly smooth and slowly-varying function, a reasonable degree of confidence could be placed in mild extrapolations to lower or higher energies.

As an ion beam travels through the background gas in a vacuum chamber, the current in the beam as measured with a Faraday probe will exhibit a decrease with increasing distance from the ion source (because the beam current considered here is the total beam current obtained by integrating over the entire ion beam cross section, beam divergence is not a factor contributing to this decrease). The observed decrease in measured ion current occurs because the ions are being neutralized by charge exchange and the Faraday probe will indicate only positive ions. The detection of slow ions resulting from charge exchange is greatly reduced because they tend to diffuse radially from the beam region. If resonance charge transfer were the only process to consider, the beam current, I, would decrease exponentially with distance x from the ion source.

$$I = I_o e^{-nQ_r x} \tag{3-2}$$

where n is the number density of the neutral background gas and I_o is the total beam current extracted from the ion source.

Because the density of fast neutrals in the beam can approach the density of the fast ions, the competing process of $Ar_f + Ar^+ \rightarrow Ar_f^+ + Ar$ should be considered. This inverse process has the same cross section Q_r, so that fast neutrals can be converted back to ions. However, the density of background ions in typical ion beam applications is usually down by several orders of magnitude from the neutral density allowing the inverse process to be neglected.[17]

The mean free path λ of a beam ion with respect to charge transfer is given by

$$\lambda = \frac{1}{n\,Q_r} \; . \tag{3-3}$$

Background pressures in a bell jar with an operating ion source typically range from 1×10^{-5} Torr to about 5×10^{-4} Torr, the corresponding range of mean free paths for a 500 eV ion beam would thus be roughly 1300 cm down to 26 cm. Operating in the upper end of this background pressure range would yield beams having a significant content of fast neutrals within a transport distance of a few tenths of a meter. Because ion beam current densities are customarily monitored using Faraday probes, accurate values for the total sputtering dose delivered to a substrate or target must take into account the energetic neutral component of the beam.

Figure 3-2 is a plot of the product of the mean free path and the pressure as a function of ion energy. The curve was calculated from the data of Fig. 3-1 assuming ideal gas behavior at a temperature of approximately 300°K. At a given beam energy, dividing the ordinate by the background pressure yields a measure of the mean free path for resonance charge exchange.

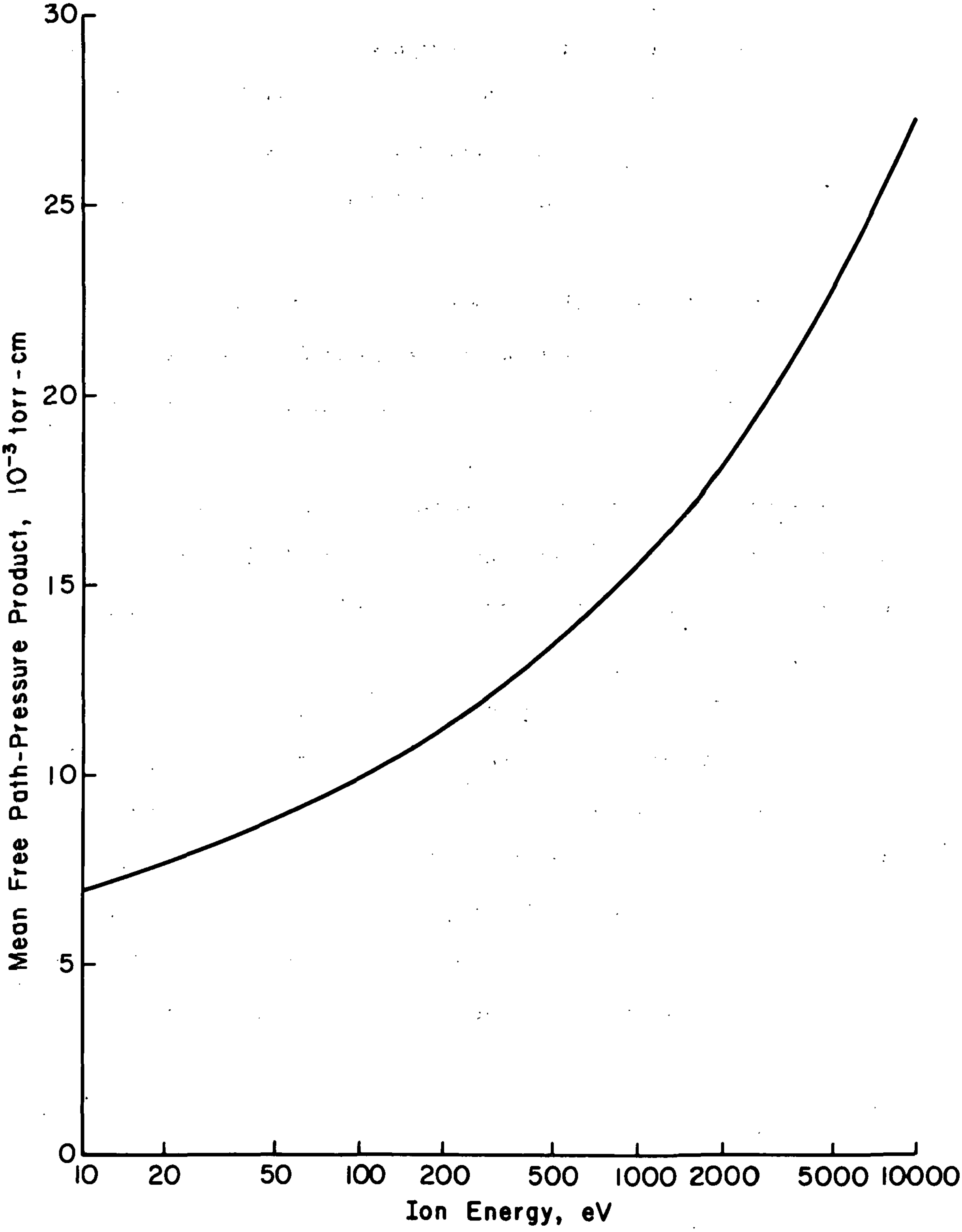

Figure 3-2. Argon resonance charge exchange: mean free path-pressure product as a function of ion energy.

A more refined estimate of the magnitude of the charge exchange effect could possibly be developed by considering the detailed effusion of neutral gas from the ion source rather than assuming a uniform density of background gas. Kaufman[17] has considered the gradient of neutral density downstream of an ion thruster and its effect on the generation of a charge exchange plasma. However, the accuracy of the experimental values used here for the charge exchange cross section probably does not warrant the inclusion of higher order effects in these estimates.

As an example of the loss in measured beam current with distance, the integrated beam current data taken using a 15 cm multipole ion source can be compared with calculated values based on the curve in Fig. 3-2. Table 3-1 compares total integrated beam currents at different distances from the ion source with values calculated for the two longer distances based on the value of the current at 5 cm. Data to calculate the total integrated beam current at the ion source were unavailable; therefore, the current I_o in Eq. (3-2) was calculated by inverting the equation and using the current measured 5 cm from the source along with the appropriate cross section from Fig. 3-1. The source operating conditions were the same for all three current density measurements.

Table 3-1. Comparison of Measured Beam Currents with Values Calculated from Charge Exchange Considerations.

Distance from Source, cm	Pressure, Torr	Total Integrated Beam Current, ma	Calculated Beam Current, ma	Percent Difference
5	4×10^{-4}	98.7	-	-
10	4×10^{-4}	85.0	85.1	0.0%
15	2.8×10^{-4}	86.1	83.8	2.7%

The agreement between the calculated beam currents and the measured currents is seen to be excellent, supporting the charge exchange theory as summarized in Fig. 3-2.

Momentum and Energy Transfer

Only through scattering from the particles of comparable mass can energetic particles of the beam lose significant energy and forward momentum. Scattering at sufficiently large angles will remove some ions or atoms entirely from the effective working volume of the beam. Because the neutral background gas has a density several orders of magnitude greater than the background ion density, collisions with neutral atoms are dominant compared with collisions involving the background charge exchange ions. Further, the probability of charge exchange prior to elastic collisions is high for incident ions. The collisions of high velocity neutrals with background neutrals is thus the dominant process for significant momentum and energy loss prior to sputtering. In addition, the cross sections for ion-neutral collisions are not expected to differ substantially from the neutral-neutral cross sections when multi-electron atoms are considered.

Collision Dynamics

The deBroglie wavelength of an argon atom or ion with a typical beam energy of 500 eV is:

$$\frac{h}{p} = 2.03 \times 10^{-13} \text{ m}$$

where h is Planck's constant and p is the momentum of the atom. This wavelength is very small compared to atomic dimensions, allowing the use of classical particle trajectories as a first approximation to the scattering of argon from argon. Measuring the angular momentum of the two colliding atoms in units of $h/2\pi$ yields an angular momentum quantum number for the collision that is typically several thousand for impact parameters of the order of atomic dimensions. This is a further indication that classical dynamics is applicable since most collisions of interest fall in the realm of very large quantum numbers.

If the interaction potential between two atoms is known, the classical equations of motion can be solved to relate the scattering angle to the impact parameter for the incident atom. The solution is most directly obtained using center of mass coordinates where a particle of reduced mass μ interacts with a fixed center of force through a potential $V(r)$ where r is the separation distance of the particle from the center of force.[18] Conservation of energy can be expressed as

$$\tfrac{1}{2}\mu\upsilon_o^2 = \tfrac{1}{2}\mu\dot{r}^2 + \tfrac{1}{2}\mu r^2\dot{\phi}^2 + V(r) \tag{3-4}$$

where υ_o is the relative speed of the two atoms at large separations where $V(r)$ is negligible, and ϕ and r are the angular and radial coordinates respectively of the incoming particle.

Conservation of angular momentum can be expressed as

$$\mu\upsilon_o s = \mu r^2\dot{\phi} \tag{3-5}$$

where s is the impact parameter (see Fig. 3-3). Eliminating $\dot{\phi}$ between Eqs. (3-4) and (3-5) and using the chain rule for differentiation we can write:

$$\frac{dr}{d\phi} = \frac{r^2}{s}\left(1 - \frac{s^2}{r^2} - \frac{V(r)}{\frac{1}{2}\mu\upsilon_o^2}\right)^{\frac{1}{2}} \tag{3-6}$$

or,

$$d\phi = \frac{s}{r^2}\left(1 - \frac{s^2}{r^2} - \frac{V(r)}{\frac{1}{2}\mu\upsilon_o^2}\right)^{-\frac{1}{2}} dr \tag{3-7}$$

Integration of Eq. (3-7) gives the angle through which the radius vector turns during the collision. Let the total turning angle be ϕ_t, then

$$\phi_t = 2\int_{r_o}^{\infty} \frac{s}{r^2}\left(1 - \frac{s^2}{r^2} - \frac{V(r)}{\frac{1}{2}\mu\upsilon_o^2}\right)^{-\frac{1}{2}} dr \tag{3-8}$$

where r_o is the distance of closest approach. The scattering angle in the center of mass system is given by

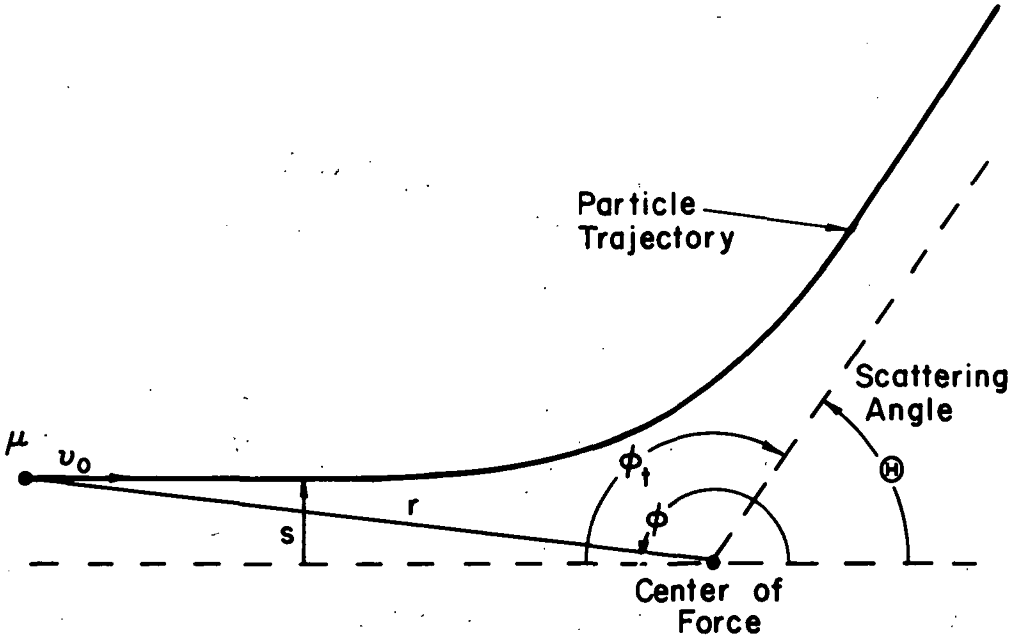

Figure 3-3. Scattering of reduced mass particle by a center of force.

$$\Theta = \pi - \phi_t \; . \tag{3-9}$$

Therefore,

$$\Theta = \pi - 2s \int_{r_o}^{\infty} \frac{dr}{r^2} \left(1 - \frac{s^2}{r^2} - \frac{V(r)}{\frac{1}{2}\mu \upsilon_o^2} \right)^{-\frac{1}{2}} \tag{3-10}$$

which relates the scattering angle in the center of mass system to the impact parameter and energy of the incident particle.

For incident and target particles having equal masses (which is the case of most interest), the scattering angle in the center of mass system is easily converted to the scattering angle θ in the laboratory frame of reference:[19]

$$\theta = \frac{\Theta}{2} \; . \tag{3-11}$$

The integration of Eq. (3-10) is not straightforward because the upper limit is infinite and the integrand itself has a singularity at the point of closest approach. Closed form solutions in terms of elliptic integrals are known for only a few power-law functions of r for the potential $V(r)$.[18]

The actual integration can be carried out numerically after a change of variables to $u = 1/r$ which gives finite limits but does not remove the singularity in the integral. An algorithm was developed for this integration utilizing a ten-point Gauss-Legendre quadrature scheme along with a logarithmically decreasing integration interval as the integration proceeds from the well-behaved end of the interval toward the singularity. Before integrating, the upper limit of integration, $u_o - 1/r_o$, was first determined by an iterative solution to the (usually) transcendental equation:

$$\frac{2V(r_o)}{E_t} + \frac{s^2}{r_o^2} = 1 \tag{3-12}$$

obtained from energy and momentum conservation, where E_t is the energy of the incident particle in the laboratory frame of reference.

To verify that the integration algorithm was functioning properly, scattering angles for an inverse square law force (Rutherford Scattering) were calculated. These calculated angles for 1 eV argon ions incident on argon ions were compared with the closed-form solution, Table 3-2 and Fig. 3-4. The qualitative agreement between the numerical and closed form solutions is adequately demonstrated in Fig. 3-4, while the numerical values tend to exhibit a divergence of only a few units in the third significant figure.

Table 3-2. Comparison of Numerical Integration with Closed Form Solution for Rutherford Scattering.

Impact Parameter Å	θ, Closed Form Deg.	θ, Numerical Integration Deg.
10	55.22	55.05
20	35.75	35.59
30	25.64	25.39
40	19.80	19.57
50	16.07	15.61
60	13.50	13.49
70	11.62	11.63
80	10.20	10.13
90	9.09	9.06
100	8.19	8.20

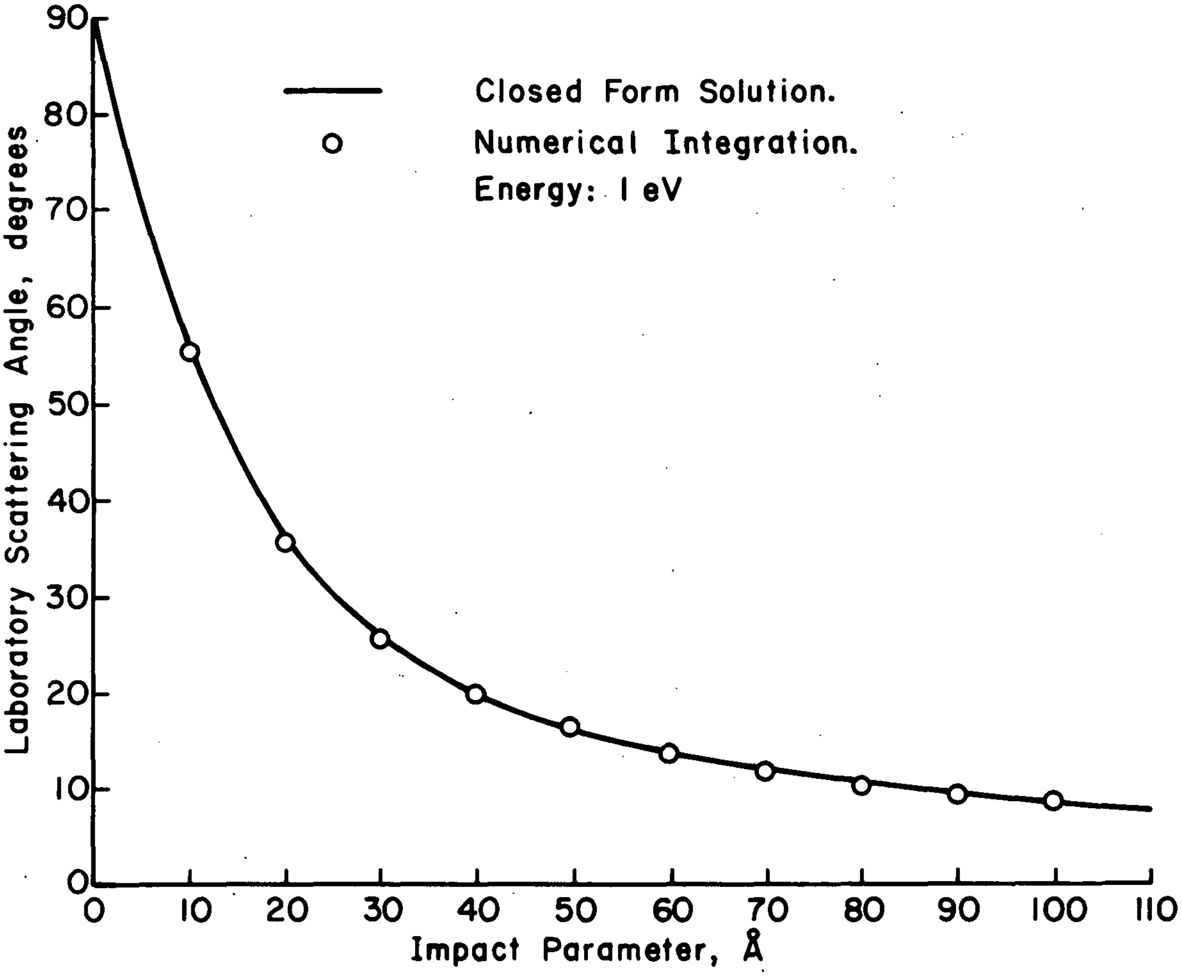

Figure 3-4. Rutherford Scattering: Comparison of closed form and numerical integration for $Ar^+ \rightarrow Ar^+$ @ 1 eV.

Argon Interaction Potential

To use a classical approximation for argon-argon scattering it is necessary to obtain a potential function describing the argon-argon pair interaction. Barker, Fisher and Watts[20] have developed an argon pair potential that is in best overall agreement with experimental data from a number of sources such as specific heats, internal energies, viscosities, solid state parameters, and scattering data. Their expression for the argon isolated pair potential is the Barker-Pompe form:

$$V(r) = \varepsilon \left[e^{-\alpha(R-1)} \sum_{i=o}^{5} A_i (R-1)^i - \frac{C_6}{(R^6 + \delta)} - \frac{C_8}{(R^8 + \delta)} - \frac{C_{10}}{(R^{10} + \delta)} \right] \tag{3-13}$$

where $R = r/r_m$.

The Barker-Fisher-Watts coefficients for argon are given in Table 3-3.

Table 3-3. Barker-Fisher-Watts Coefficients for the Argon Pair Potential.

Coefficient	Value	Coefficient	Value
ε	0.0122448 eV	C_6	1.10727
r_m	3.7612 Å	C_8	0.16971325
A_o	0.27783	C_{10}	0.013611
A_1	-4.50431	α	12.5
A_2	-8.331215	δ	0.01
A_3	-25.2696		
A_4	-102.0195		
A_5	-113.25		

The screened Coulomb potential used by Bingham[21,22] and Everhart, et al.[23,24] is valid at higher energies (e.g., above 50 KeV) but disregards the electron repulsion important at lower energies. Smoothly joining the Bingham[21,22] and Barker[20] potentials between the energies where each potential is known to fit experimental data well, supports the use of Barker's results up to about 1 KeV. Figure 3-5 is a plot of the pair potential on a linear scale showing the attractive part of the potential, the minimum, and the zero crossing. The depth of the attractive well is given by the coefficient $\varepsilon = 0.0122448$ eV. This is an energy four or five orders of magnitude lower than most beam energies of interest. Thus, in scattering, attractive forces will be of little consequence compared to the dominant repulsive core potential.

Potentials for Krypton and Xenon

Barker, et al.[25] have developed potentials for two other rare gases, krypton and xenon, using nearly the same analytical form for the potential as for argon with similar adjustable parameters. The form for these potentials is:

$$V(r) = \varepsilon \left[e^{\alpha(1-R)} \sum_{i=o}^{5} A_i (R-1)^i - \frac{C_6}{(R^6+\delta)} - \frac{C_8}{(R^8+\delta)} - \frac{C_{10}}{(R^{10}+\delta)} \right] + \varepsilon \left[P(R-1)^4 + Q(R-1)^5 \right] e^{\alpha(1-R)},$$

$$\text{for } R>1 \qquad (3\text{-}14)$$

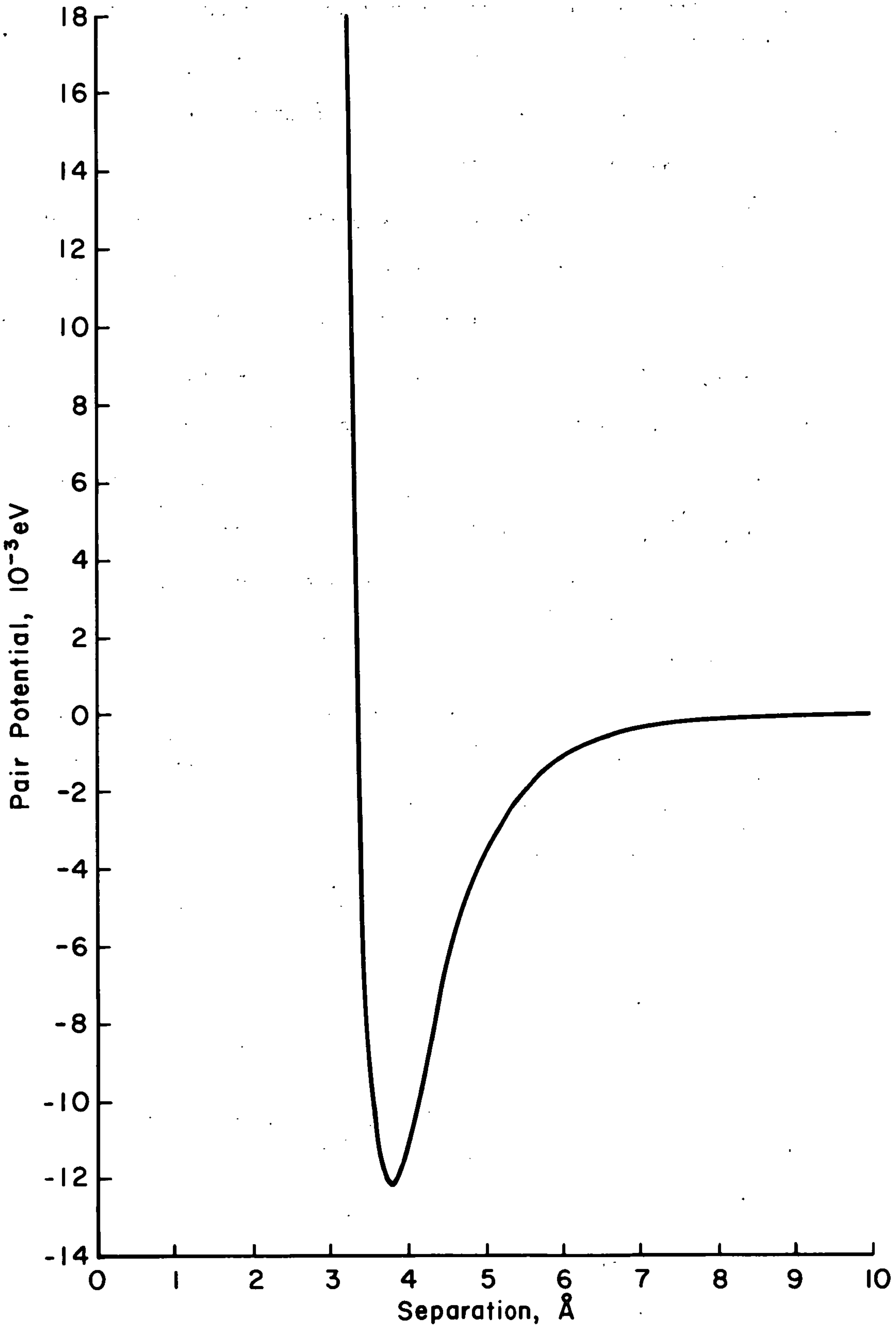

Figure 3-5. Barker-Fisher-Watts argon pair potential: attractive well and zero crossing.

$$V(r) = \varepsilon \left[e^{\alpha(1-R)} \sum_{i=o}^{5} A_i (R-1)^i - \frac{C_6}{(R^6 + \delta)} - \frac{C_8}{(R^8 + \delta)} \right.$$

$$\left. - \frac{C_{10}}{(R^{10} + \delta)} \right], \text{ for } R<1 \qquad (3\text{-}15)$$

with $R = r/r_m$. The coefficients for krypton and xenon are given in Table 3-4.

Table 3-4. Coefficients for Krypton and Xenon Pair Potentials

Coefficient	Kr Value	Xe Value
ε	0.01740 eV	0.02421 eV
r_m	4.0067 Å	4.3623 Å
A_o	0.23526	0.2402
A_1	-4.78686	-4.8169
A_2	-9.2	-10.9
A_3	-9.0	-25.0
A_4	-30.0	-50.7
A_5	-205.8	-200.0
C_6	1.0632	1.0544
C_8	0.1701	0.1660
C_{10}	0.0143	0.0323
α	12.5	12.5
δ	0.01	0.01
P	-9.0	59.3
Q	68.67	71.1

Figure 3-6 compares the pair potentials for Ar, Kr and Xe showing the increase in effective radius of the atom as the atomic number increases.

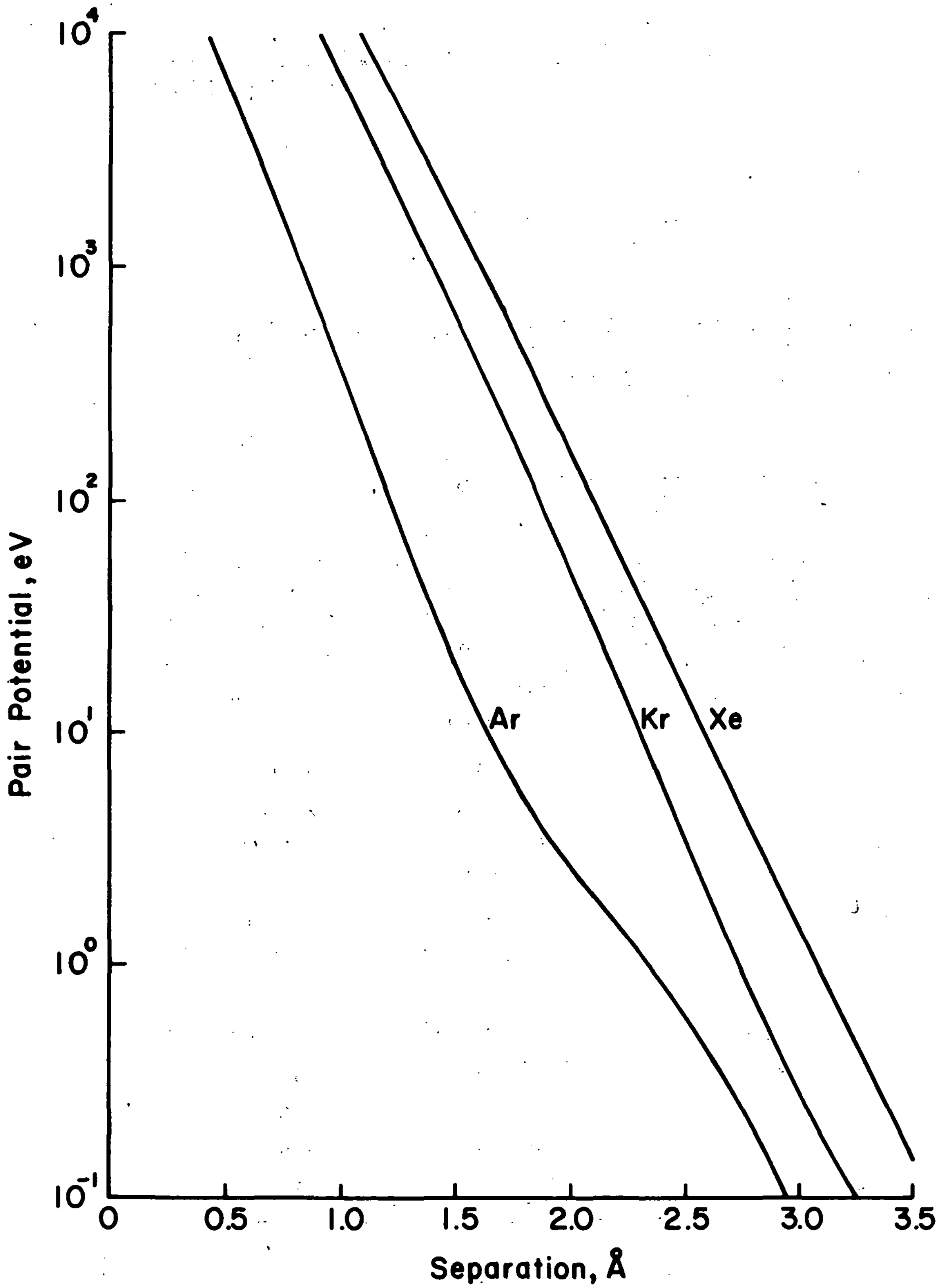

Figure 3-6. Pair potentials for rare gases.

The general character of the like-particle scattering from Ar, Kr and Xe in the classical approximation would be similar since the shapes of the potentials are similar. However, the corresponding cross sections for the heavier gases should be larger in the energy range displayed in Fig. 3-6.

Calculation Procedures

There are numerous intermediate steps in cross section calculations as well as several different modes for presenting the information. Some of the Ar-Ar calculations are presented here in detail for certain energies to emphasize the numerical procedures and to show some simplifying correlations that can be used.

Table 3-5 contains laboratory scattering angles calculated as a function of impact parameter and incident energy using the Barker-Fisher-Watts argon potential.

Table 3-5. Calculated Laboratory Scattering Angles in degrees as a Function of Incident Energy and Impact Parameter for Argon.

Impact Parameter, Å	Energy of Incident Atom, eV				
	1.0	10	100	500	1000
0.0	90.0	90.0	90.0	90.0	90.0
0.2	84.9	82.5	80.1	77.5	75.8
0.4	79.9	75.0	70.2	65.0	61.7
0.6	74.8	67.4	60.2	52.5	47.9
0.8	69.7	59.9	50.0	40.2	34.6
1.0	64.6	52.3	39.7	28.2	22.4
1.2	59.4	44.9	29.5	17.4	12.4
1.4	54.2	37.8	19.9	9.02	5.59
1.6	49.0	31.1	12.0	4.00	2.22
1.8	43.7	25.0	6.93	1.81	0.94
2.0	38.3	19.4	4.16	0.95	0.49
2.2	32.8	14.6	2.60	0.57	0.29
2.4	27.3	10.3	1.60	0.34	0.17

Table 3-5. (Continued)

Impact Parameter, Å	Energy of Incident Atom, eV				
	1.0	10	100	500	1000
2.6	21.8	6.78	0.93	0.19	0.10
2.8	16.3	4.03	0.49	0.10	0.05
3.0	11.0	2.10	0.24	0.05	0.02
3.2	6.28	0.90	0.10	0.02	0.01
3.4	2.49	0.26	0.03	0.01	
3.6	0.01	0.01	0.01		

Figure 3-7 is a plot of some of the numerically integrated scattering angles given in Table 3-5. These curves show the basic trends of the scattering in this energy range. Lower energy atoms are scattered at larger angles for the same impact parameter implying an increase in calculated cross sections as the beam energy is reduced.

Although, using classical calculations, it is not possible to obtain correct values for the total cross sections,[18] it is possible to correlate cross sections for scattering through angles greater than some minimum angle θ_o. The classical cross section is taken as the area of a circle of radius equal to the impact parameter for this minimum angle.

Table 3-6 gives representative calculated values for the total cross section, $Q(\theta > 10°)$, for scattering through angles greater than 10° as a function of energy.

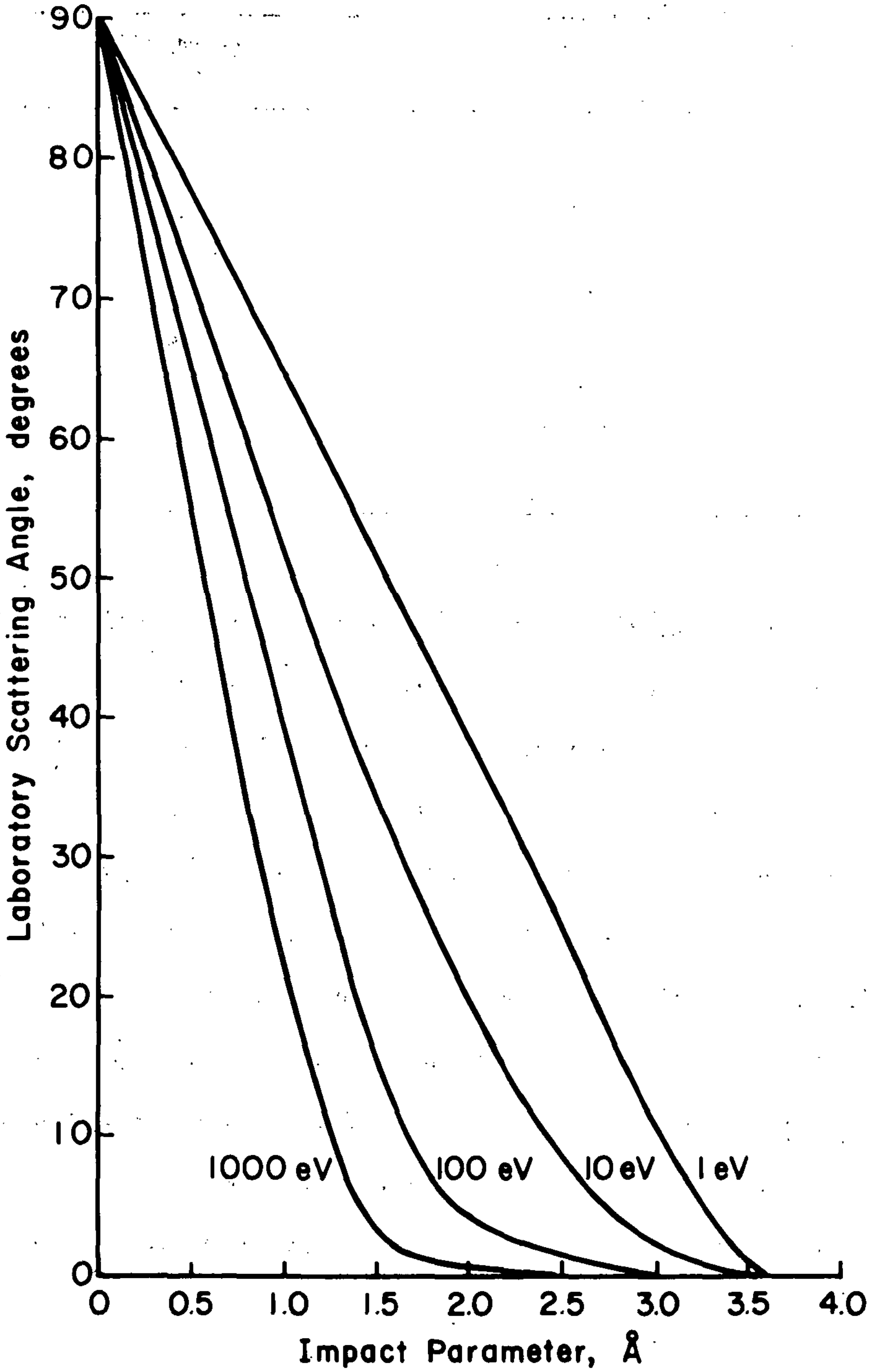

Figure 3-7. Calculated argon laboratory scattering angles as a function of impact parameter at various energies.

Table 3-6. Total Cross Section for Argon Scattering through Angles Greater than 10°.

E eV	Q (θ>10°) Å^2
1	29.1
3	24.2
10	18.4
30	12.9
100	8.76
300	6.71
1000	5.00
2000	4.14

For small angle scattering, an approximate correlation is achieved for potentials that approach exponential behavior in the energy range of interest. The Barker-Fisher-Watts potential exhibits exponential behavior over certain energy ranges at small separations. This correlation for the cross section as a function of energy can be seen by plotting the square root of the cross section versus the logarithm of the fourth root of the cross section divided by the energy.[26] Figure 3-8 is a plot of the correlated parameters showing the behavior over approximately four decades for $Q(\theta>10°)$. The correlation appears to be nearly linear in two separate energy ranges, $E>100$ eV and $E<100$ eV. Such a correlation can be used for interpolation and for minor extrapolation.

Calculated Differential Cross Sections for Argon

The necessity for calculating differential cross sections directly from a potential might reasonably be questioned; however, Massey and Gilbody have this to say:

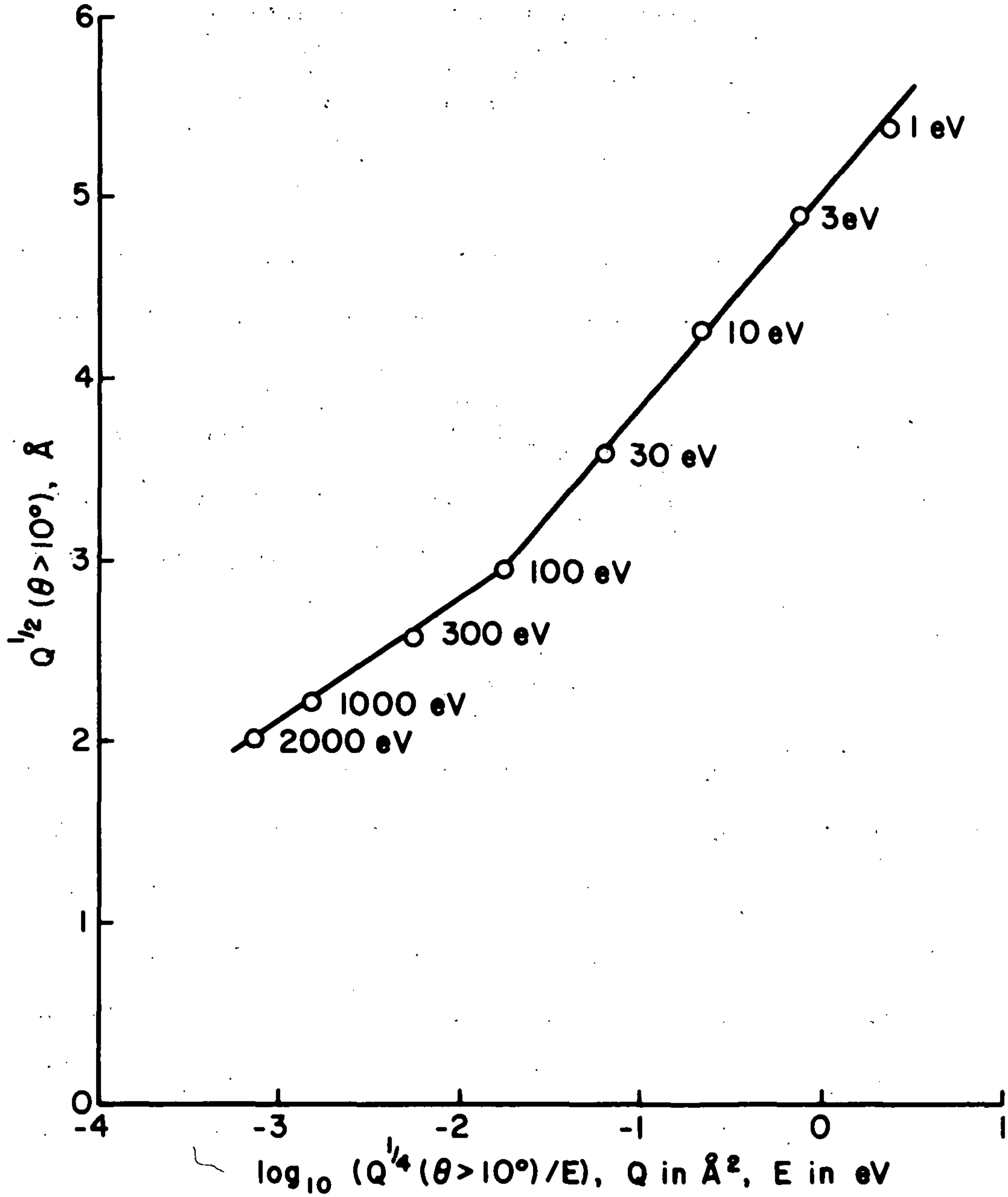

Figure 3-8. Correlation parameters for cross section and energy for argon scattering through angles greater than 10°.

> "Up to the time of this writing (1974) measurements of differential cross-sections for elastic scattering have been almost entirely confined to beams of positive ions in gases. For neutral atom beams observations have been confined to the 'total' scattering outside a particular mean scattering angle in the laboratory system. Measurements of this kind have also been carried out for ion beams."[27]

The thorough search conducted by Massey and Gilbody thus uncovered no data relating to the important neutral-neutral momentum transfer process.

To determine the average momentum transfer for argon atoms that suffer collisions with other argon atoms, the differential cross section must first be calculated. The differential cross section is given by[18]

$$\sigma(\theta) = - \frac{s}{\sin\theta} \frac{ds}{d\theta} , \qquad (3\text{-}16)$$

where s is the impact parameter and $\sigma(\theta)$ is the differential cross section measured in m^2/steradian. Data of the kind given in Fig. 3-7 were used to calculate the differential cross section using Eq. (3-16). As an example, the differential scattering cross section for 500 eV argon is plotted in Fig. 3-9. It can be seen from this curve that most of the scattering occurs at angles that do not contribute significantly to momentum transfer; also, the differential cross section tends to zero as the scattering angles approach 90°.

Ion-Neutral Collisions

A potential function was not available describing the interaction between an argon ion and a neutral argon atom. However, because only

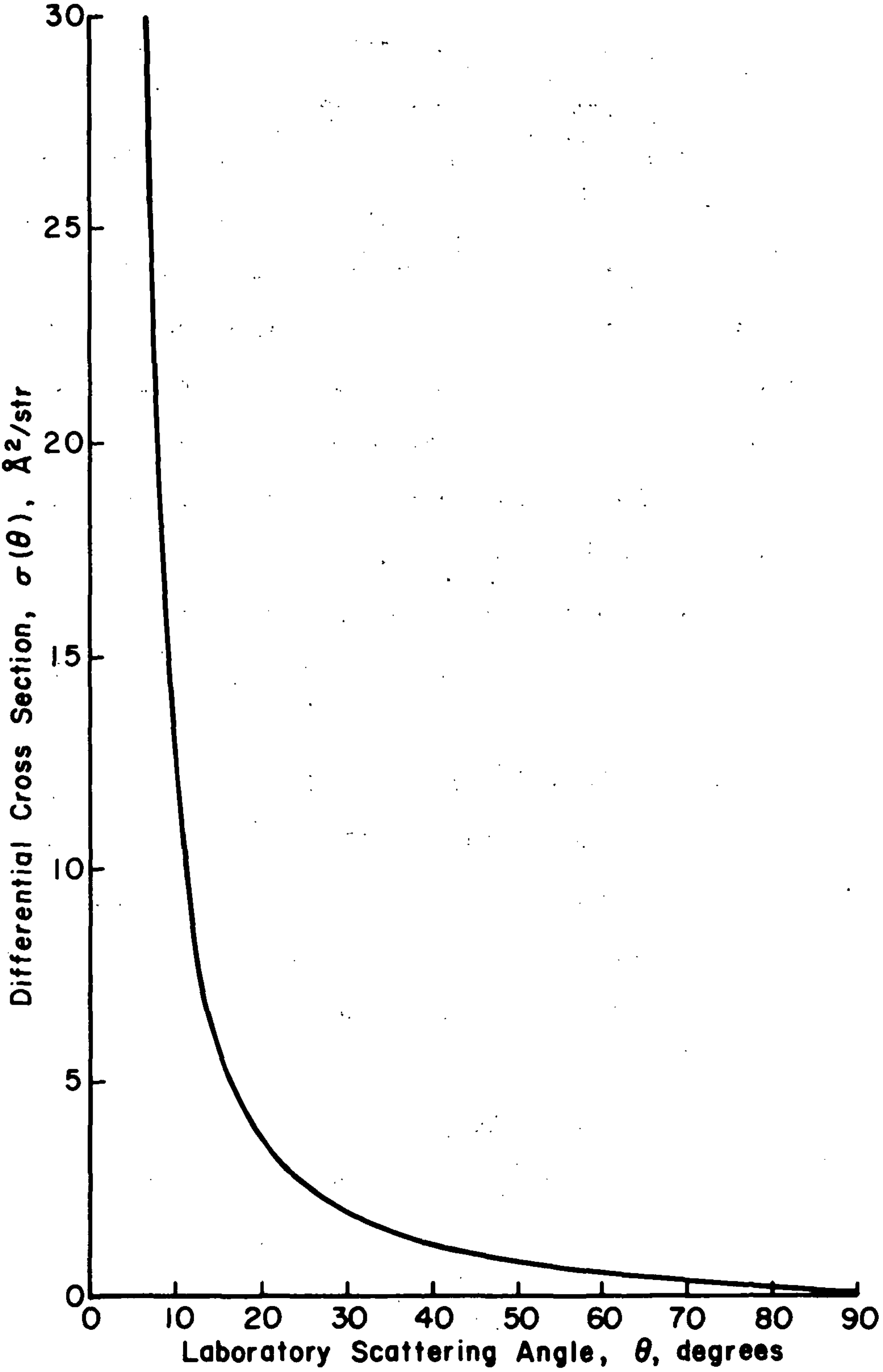

Figure 3-9. Calculated differential elastic scattering cross-section for 500 eV Ar-Ar collisions.

one of the particles is charged, the interaction at large distances can be of no lower order than dipole-monopole which would imply a modification in the potential to include attractive r^{-4} and higher-order potential terms. The repulsive core potential would be altered by the absence of one electron compared to the Ar-Ar interaction; but, generally, the ion-atom interaction should remain of similar order of magnitude to the atom-atom interaction at energies above several eV. The absence of one electron in the ion-atom interaction may tend to weaken the repulsion, thereby reducing the differential scattering cross section compared to the argon-argon differential cross section.

Some experimental data are available for Ar^+-Ar collisions at 400 eV.[28] These experimental data, expressed as a differential cross section, are compared in Fig. 3-10 to the calculated differential cross section for 500 eV Ar-Ar collisions.

As expected, the Ar^+-Ar differential cross section is less than that for Ar-Ar; however, the general trends of the data are similar in each case. The experimental data reported by Aberth and Lorents[28] oscillates somewhat but the linear fit shown in Fig. 3-10 is a fair representation of the magnitudes and trends in the data.

Even when the interaction cross sections are directly compared between Ar^+-Ar and Ar-Ar collisions, the neutral-neutral collisions remain the dominant process to be considered for momentum and energy loss in the beam.

Energy and Momentum Transfer

In a collision in which an atom is scattered through an angle θ, it will have lost a fraction of its energy equal to $(1-\cos^2\theta)$.

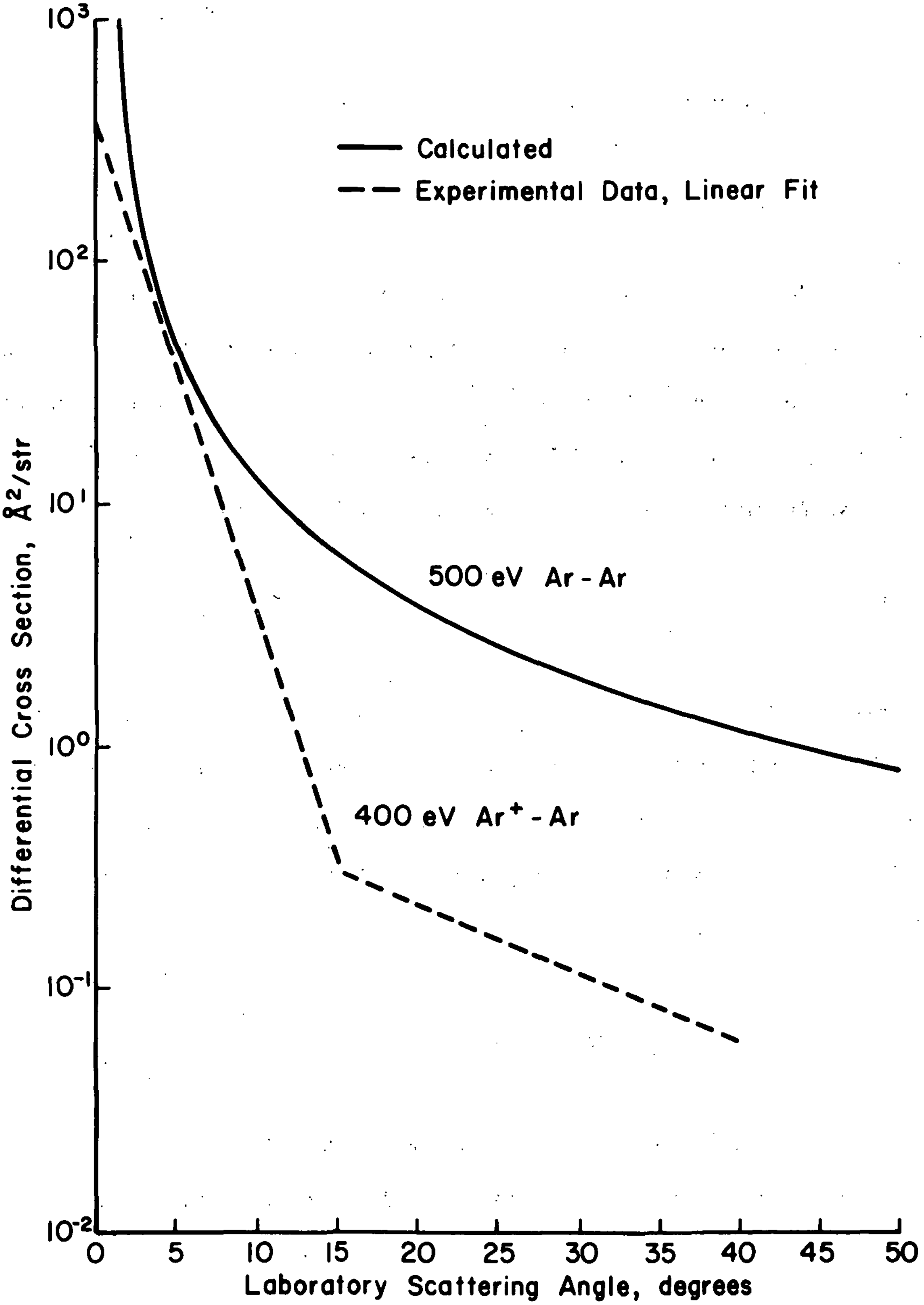

Figure 3-10. Comparison of differential scattering cross sections for Ar-Ar (calculated) and Ar^+-Ar (experimental).

The average fractional energy transfer, f, for scattered atoms is:

$$f = \frac{\int_0^{\pi/2} (1-\cos^2\theta)\ \sigma(\theta)\ 2\pi\sin\theta d\theta}{\int_0^{\pi/2} \sigma(\theta)\ 2\pi\sin\theta d\theta} . \tag{3-17}$$

This fraction can be thought of as the ratio of two cross sections: i.e., the ratio of an energy transfer cross section to the total scattering cross section. The fractional transfer of energy from a beam traversing a distance dx through a medium containing a number density n of scattering centers of total scattering cross section Q is:

$$\frac{\Delta E}{E} = f\ n\ Q\ dx \tag{3-18}$$

where f is the average fractional transfer per collision given in Eq. (3-17). The product fQ can be considered as a single parameter or cross section, Q_E, related to the rate of energy decay in the beam. Equation (3-19) is the customary form for the widely used, defined cross section for viscosity.[29]

$$Q_E = \int_0^{\pi/2} (1-\cos^2\theta)\ \sigma(\theta)\ 2\pi\sin\theta d\theta \tag{3-19}$$

A similar expression is obtained when momentum transfer is considered. This momentum transfer cross section is used to describe diffusion processes:

$$Q_p = \int_0^{\pi/2} (1-\cos\theta)\ \sigma(\theta)\ 2\pi\sin\theta d\theta . \tag{3-20}$$

Integration of Eqs. (3-19) and (3-20) yields cross sections for energy and momentum transfer.

Using differential cross sections calculated for a number of incident energies, the integrals of the form given in Eqs. (3-19) and (3-20) were evaluated to yield cross sections for energy and momentum transfer as a function of beam energy for Ar, Kr, and Xe. Some of the results of these integrations are given in Table 3-7. These data are plotted in Figs. 3-11 and 3-12 over the energy range from 1 eV to 1000 eV. These cross sections then are the desired end result of this numerical effort. An example of their anticipated use is in the determination of acceptable background pressures for ion beam etching. Figure 3-13 is a plot of the mean free path for energy transfer times the pressure versus beam energy. At a given energy, dividing the ordinate by the background pressure yields a measure of the mean free path or attenuation length for beam energy decay in that environment and at the given beam energy. The curve was calculated from the Ar data of Table 3-7 assuming ideal gas behavior and a temperature of approximately 300°K. An energy attenuation in the beam of up to 10 percent might be expected to be acceptable. The source-to-substrate distance should therefore correspond to about 1/10 of a mean free path. At 1000 eV, for example, the pressure times distance should equal about 1.9×10^{-2} Torr-cm, or less, for a 10 percent, or less, attenuation in beam energy. This calculation, then, permits a tradeoff to be made between pumping capacity and the ion beam energy and momentum content. The simple method described should be adequate for losses up to 10 to 20 percent of the initial beam energy, but larger losses will probably require a more detailed calculation that will take into account both the mean

Table 3-7. Calculated Energy and Momentum Transfer Cross Sections.

Energy, eV	Energy Transfer Cross Section, Å^2			Momentum Transfer Cross Section, Å^2		
	Ar	Kr	Xe	Ar	Kr	Xe
1	11.2	14.0	17.7	7.17	9.04	11.5
2	9.54	12.5	15.9	6.07	8.10	10.3
3	8.57	11.8	14.9	5.42	7.61	9.66
5	7.37	10.9	13.8	4.63	7.03	8.93
10	5.88	9.78	12.4	3.68	6.31	8.02
20	4.72	8.77	11.1	2.97	5.66	7.18
30	4.20	8.22	10.4	2.65	5.30	6.73
50	3.67	7.55	9.59	2.32	4.86	6.17
100	3.09	6.70	8.51	1.96	4.30	5.47
200	2.60	5.89	7.49	1.65	3.77	4.81
300	2.34	5.44	6.93	1.48	3.48	4.44
500	2.03	4.89	6.24	1.28	3.12	3.99
1000	1.65	4.19	5.36	1.04	2.66	3.41

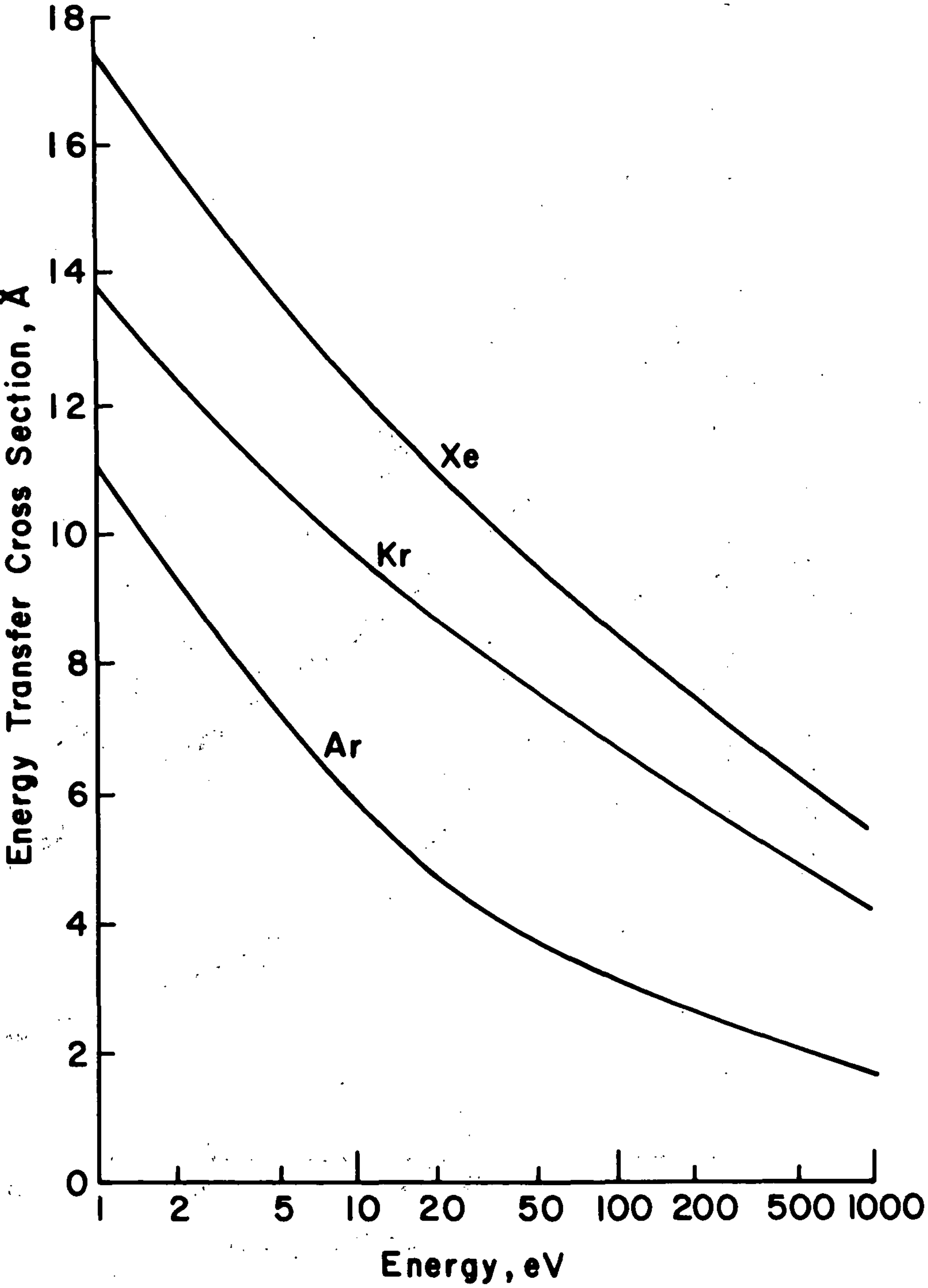

Figure 3-11. Energy transfer (viscosity) cross section for Ar, Kr, and Xe as a function of energy.

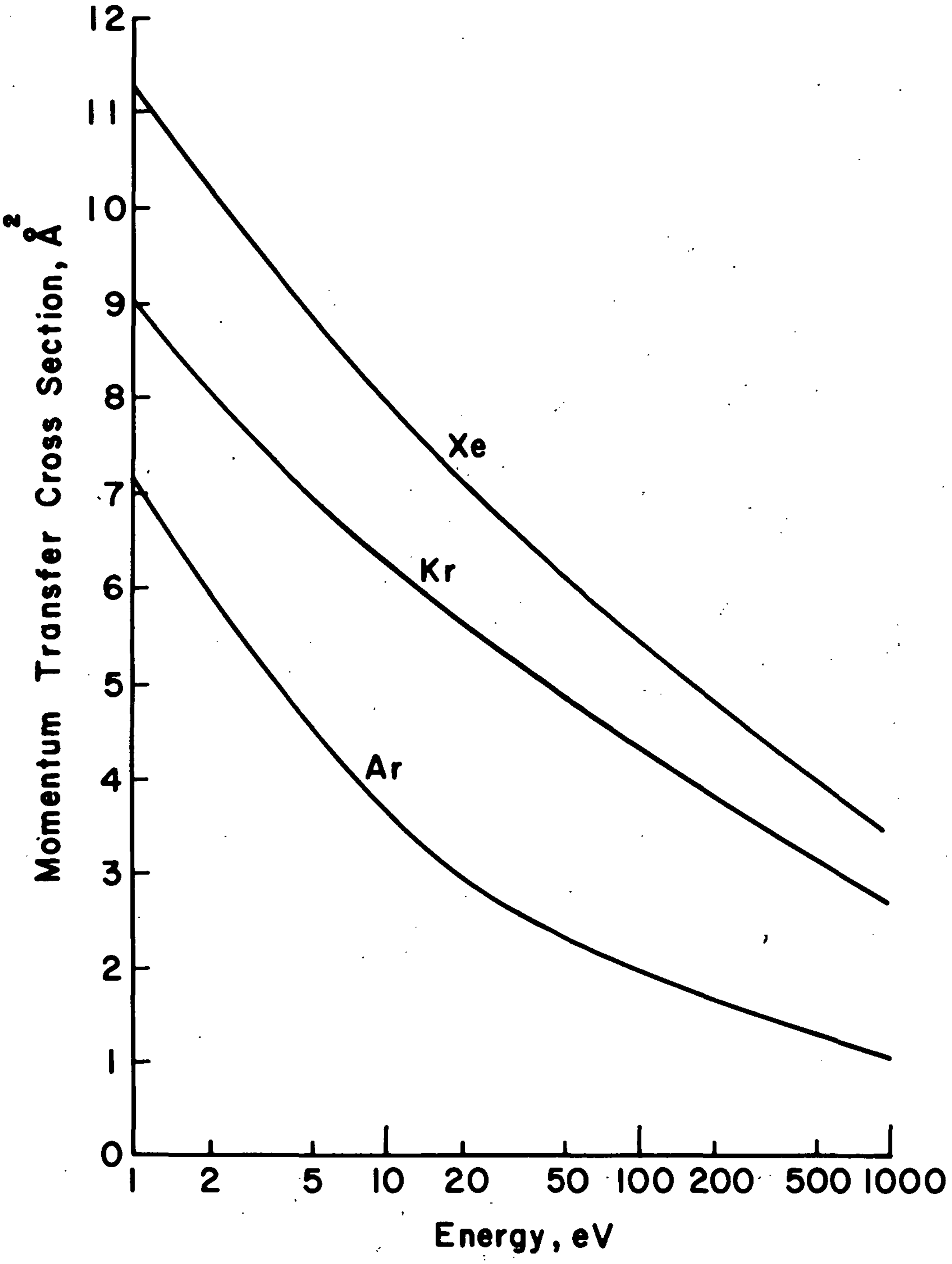

Figure 3-12. Momentum transfer (diffusion) cross section for Ar, Kr, and Xe as a function of energy.

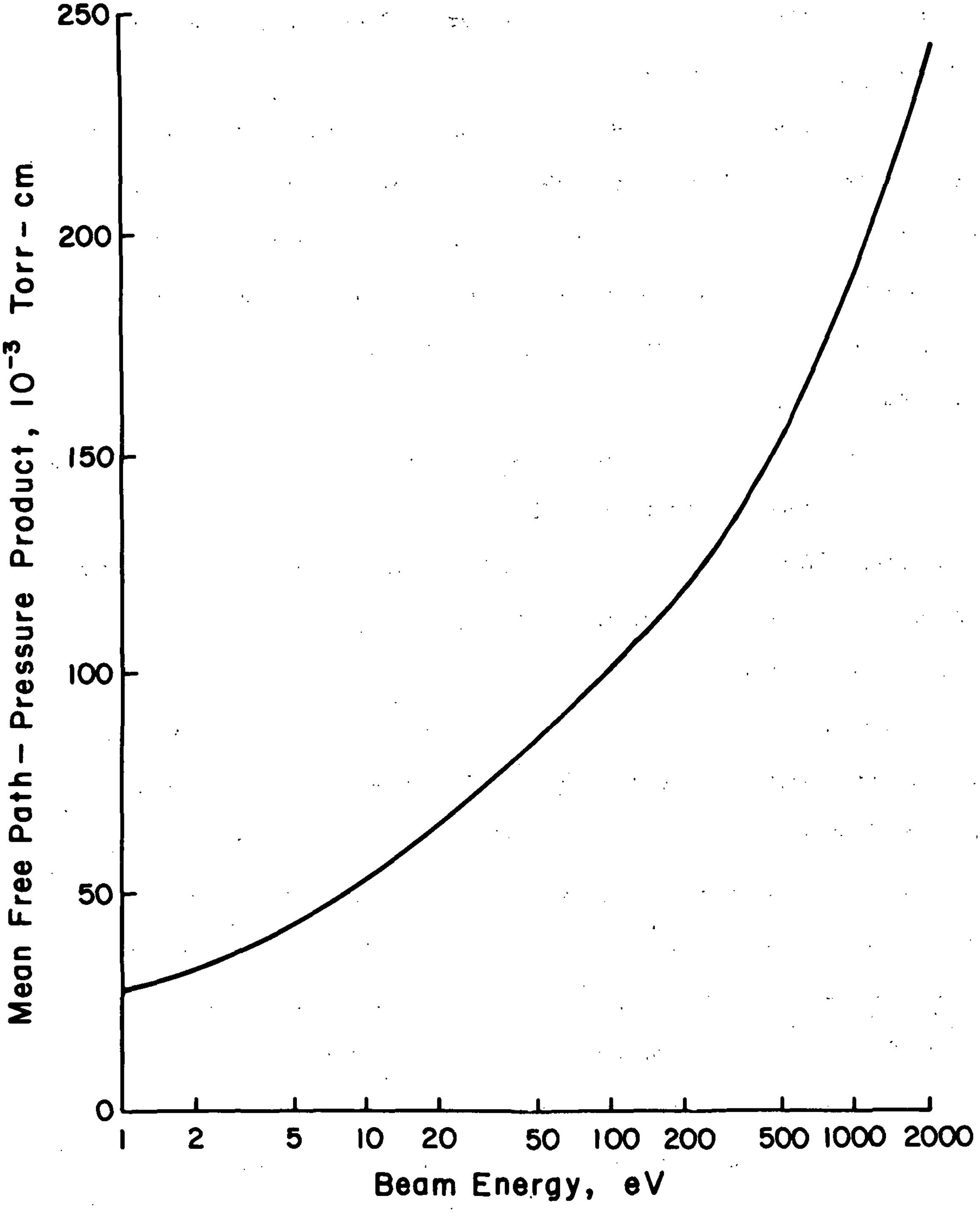

Figure 3-13. Argon energy transfer: mean free path-pressure product as a function of beam energy.

energy and the distribution of particle energies as a function of distance. Knock-on atoms should also be included as well as beam atoms in a more detailed analysis.

In comparison to the 1.9×10^{-2} Torr-cm for a 10 percent energy loss in the beam, a 10 percent charge exchange requires 1.4×10^{-3} Torr-cm. It should be clear that a substantial amount of charge exchange can take place without significantly affecting the momentum, energy, or, to a first approximation, the sputtering capability of the beam.

The interaction of a beam of ions passing through a background gas is of interest for industrial application of broad-beam ion sources, particularly for etching. The momentum or energy losses in the beam can be used to determine pressure, hence pumping, requirements in etching applications.

The rare gas interaction cross sections that have been obtained will allow a more thorough analysis and understanding of a variety of energetic processes involved in both ion beam and plasma devices. Cross sections at these high energies have not previously been available to investigators, resulting in the occasional erroneous use of thermal values. The argon energy transfer cross section has been successfully applied to the theoretical elucidation, by Harper, Cuomo, Gambino, Kaufman and Robinson[30] of a complex negative ion sputtering phenomenon discovered experimentally in diode plasma devices.

IV. ION BEAM TEXTURING OF SURFACES

Ion beam sputtering is frequently used in surface etch or milling operations where the desired result is the uniform removal of material, perhaps using a mask to produce a relief pattern on a substrate, or simply as a thinning process such as sample preparation for transmission electron microscopy. The processed surfaces, however, are often not microscopically smooth but exhibit a variety of surface textures that develop as a result of the ion bombardment.

Textures can develop on solid surfaces in several ways during directed ion beam sputtering. Physical sputtering of solid materials, which is customarily accomplished using chemically inert ion species, can reveal individual crystal grains because of differential sputter etch rates dependent on crystal grain orientation. Impurities, precipitates, phases or initially irregular surfaces can also cause characteristic textures to develop during sputtering because of preferential etching of higher sputter yield sites.[1] In addition, reactive ion beam etching can chemically texture a surface through selective removal of elements from an alloy.[2]

Of particular interest here, however, is the texturing induced by the deliberate deposition of an impurity onto a solid surface while simultaneously bombarding the surface with an ion beam. This technique is often referred to as "seeding", with the impurity being termed the seed material. Under appropriate conditions, microscopic cones or hillocks develop because of preferential sputtering of surrounding material. It has been generally understood that these cones result from clusters of seed atoms protecting the underlying substrate while surrounding substrate material is etched away.[3] Extensive experimental studies of the ion beam texturing of surfaces have been reported by Robinson and Haynes.[4]

Ion beam texturing has been attempted with many material combinations and has several potential applications. Textured surfaces have been successfully used for enhanced absorption of radiant energy in solar collectors.[5] Perhaps one of the more promising applications is in the realm of biomedical materials such as prostheses with soft or hard tissue interfaces that require firm bonding.[6,7,8,9]

Some examples of textured surfaces are shown in Figs. 4-1 to 4-4 for various combinations of seed and substrate materials. These surfaces were documented using a scanning electron microscope. Of particular interest are the prominent round knobs attached to the apexes of the Cu cones in Fig. 4-1. It appears likely that these knobs are the seed material aiding in cone formation by protecting the apexes. The sequence appears to be first the knob formation, then the eventual undercutting and removal of the knob, and finally the rounding off of the apex. Cones in all phases of this sequence are visible in Fig. 4-1.

It has been postulated that the formation and replenishment of seed clusters is a result of the surface diffusion or migration of seed atoms with nucleation or attachment occurring when other seed atoms are encountered. It has also been widely believed that a necessary, but possibly not a sufficient, condition for the formation of sputter cones is that the seed material must have a lower sputter yield than the substrate material to account for the observed differential etch. The validity of these ideas is explored within the context of an analytical model along with experimental tests.

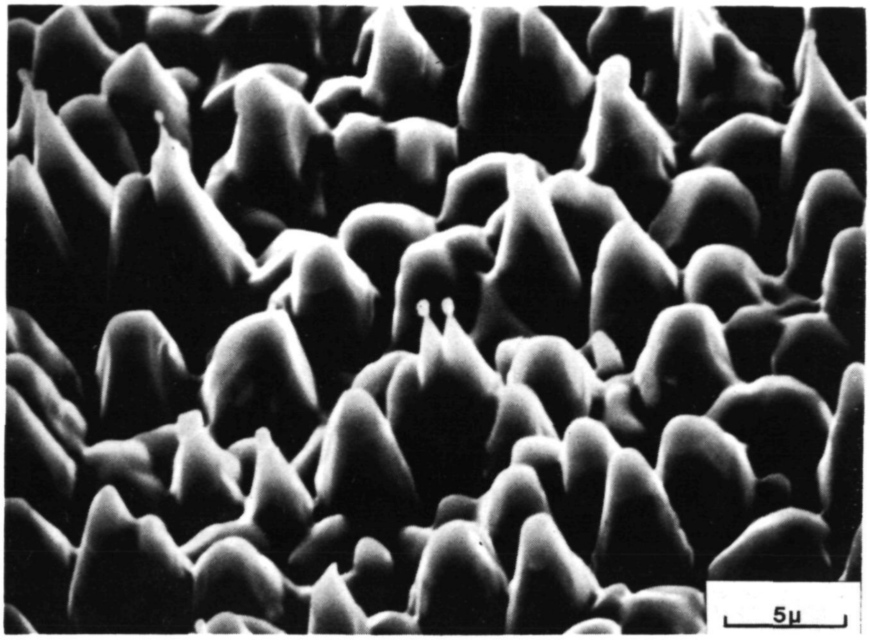

Figure 4-1. Copper sample coned using molybdenum as seed material, 500 eV Ar^+ ions, 250°C.

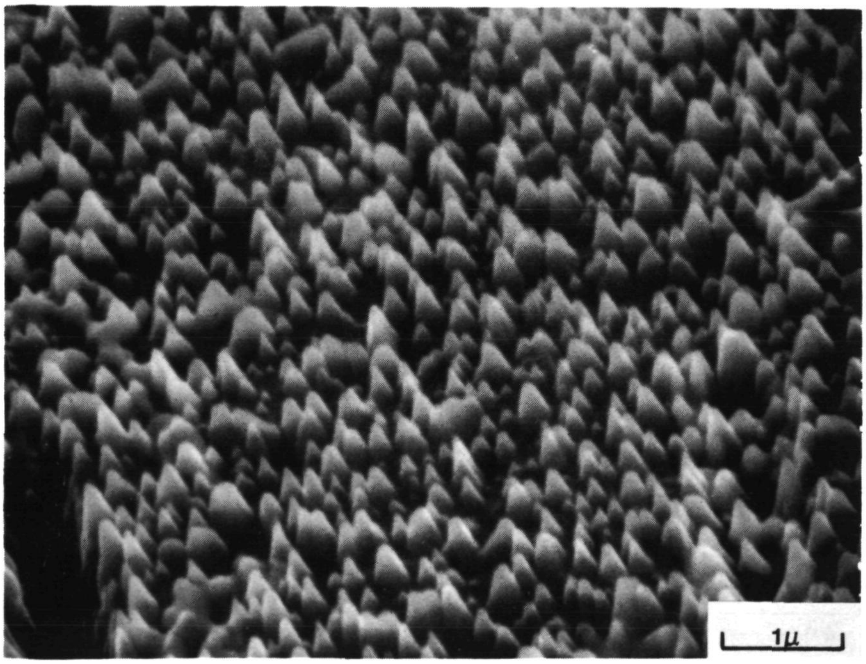

Figure 4-2. Aluminum sample coned using gold as seed material, 500 eV Ar^+ ions, 450°C.

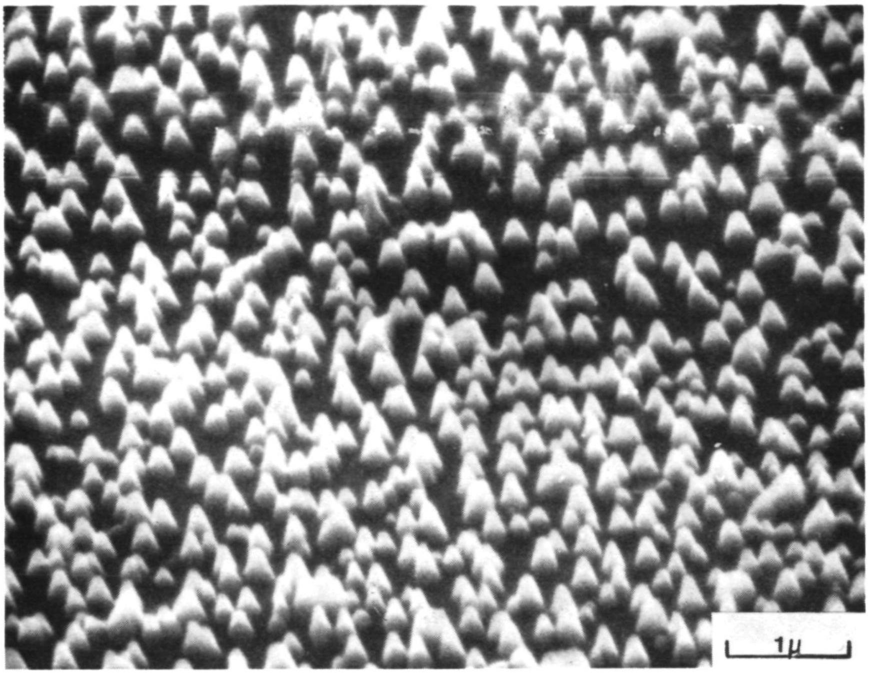

Figure 4-3. Aluminum sample coned using molybdenum as seed material, 500 eV Ar^+ ions, 250°C.

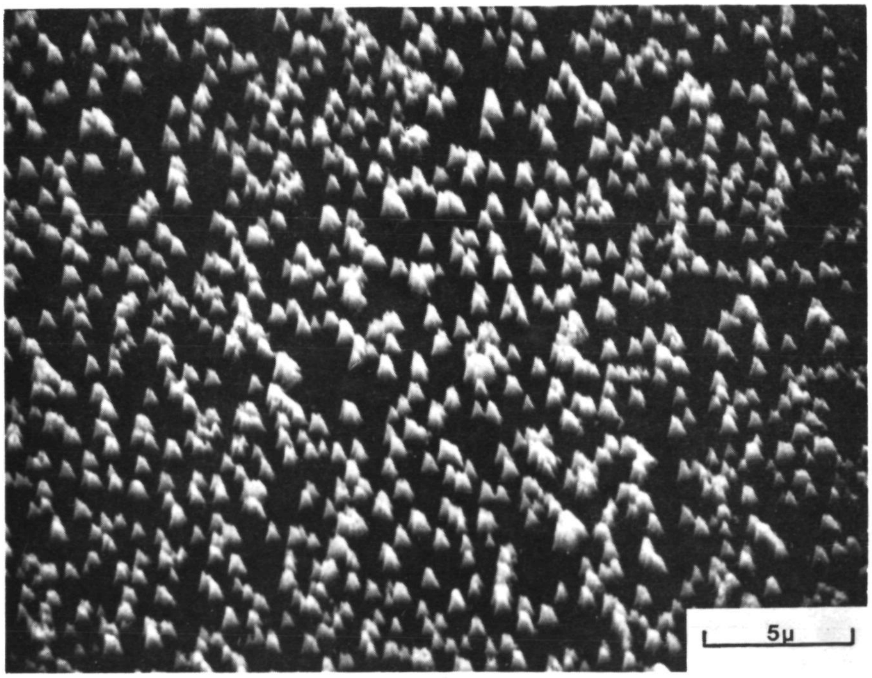

Figure 4-4. Silicon sample coned using iron as seed material, 500 eV Ar^+ ions, 600°C.

A model has been developed as a first approximation to both a qualitative and quantitative description of the surface migration of seed atoms, the clustering process, and the resulting distribution of cones on a substrate. Experimentally controllable parameters as well as physical properties of the materials involved are included in the model. The diffusion aspect is described first. The critical minimum size of seed clusters is then related to the seed diffusion rate. As a further result, a critical substrate temperature is obtained, below which cones will not be formed by the diffusion and sputtering of seed material. The predictions based on this model are investigated experimentally and an assessment is made of the impact of the model on the variously held postulates and assumptions regarding the seeding and cone formation processes.

Sputter Cone Seeding Theory

The primary features of a conceptual model used to understand seed diffusion are: (1) a substrate surface characterized as an array of uniformly distributed adsorption sites at which seed atoms can be bound to the surface after being deposited onto the substrate; (2) these individual adsorption sites described as potential energy minima that interact with seed atoms through isotropic binding and restoring forces; (3) the seed atoms of sizes and masses appropriate to the seeding species used that are deposited onto the substrate through some external means; and (4) an ion beam of a given energy and type of ion providing a uniform flux density of energetic ions over the substrate.

Surface Diffusion

The frequency for an isolated seed atom, located at an adsorption site and belonging to a population of adsorbed seed atoms in thermal equilibrium with a substrate of temperature T, to jump between adsorption sites is

$$\nu = (1/\tau_o) \exp(-E_d/kT) \ , \tag{4-1}$$

where $1/\tau_o$ is the attempt frequency for the jumping process, E_d is the activation energy for diffusion (i.e., the energy barrier between adsorption sites) and k is Boltzmann's constant. The exponential factor reflects the probability that, given thermal equilibrium at temperature T, a seed atom has an energy greater than E_d, assuming a uniform density of states. The reciprocal of the characteristic time τ_o may be thought of as a characteristic frequency of oscillation for the seed atom in the potential well representing the adsorption site. The total number of adsorption sites visited by an adsorbed seed atom during the time that it spends on the surface is given by the jump frequency ν multiplied by the mean adsorption time τ_a:

$$n_a = \nu\,\tau_a = (\tau_a/\tau_o) \exp(-E_d/kT) \ . \tag{4-2}$$

The magnitude of the mean adsorption time τ_a is governed by those processes that would tend to remove or desorb a seed atom from the surface. One candidate process would be evaporation or sublimation which would occur if a seed atom possessed simultaneously sufficient energy to break the adsorption bond and a momentum directed away from the surface. If the seed atoms are considered to be in thermal equilibrium with the substrate, the probability of having sufficient thermal energy to desorb would be $\exp(-E_o/kT)$ where E_o is the total binding energy of the seed atom to the surface. Clearly, $E_o > E_d$, making this process highly improbable. A more likely mechanism for removal of adsorbed seed atoms is physical sputtering by an applied high current density ion beam. The probability of a seed atom being sputtered depends linearly on the ion flux and on the seed cross section.

The migration of seed atoms along the surface of the substrate can be viewed as a random-walk process. Using a_o as the mean distance between adsorption sites, the random-walk diffusion length r_d is given by

$$r_d = a_o n_a^{\frac{1}{2}} = a_o(\tau_a/\tau_o)^{\frac{1}{2}} \exp(-E_d/2kT) \ . \qquad (4\text{-}3)$$

The random-walk diffusion length represents the average net separation distance of a seed atom from its initial adsorption site, achieved during a time τ_a. This, then, is the average radius through which seed atoms are expected to be able to diffuse. This expression (Eq. 4-3) is similar to diffusion equations derived for condensation of a vapor phase onto a substrate. It is necessary to obtain appropriate values for τ_a and τ_o to apply this equation to the seeding and texturing problem.

The seed adsorption time is limited by the ion beam sputter removal of seed atoms once they are attached to the surface. If the ion flux (ions/m^2-sec) is given by R_i and the cross section that a seed atom presents to the ion beam is given by σ_a then the probability per unit time P_c for individual ion-seed collisions to occur is

$$P_c = R_i\sigma_a \ . \tag{4-4}$$

The probability that a given collision will result in removal of an atom is the sputter yield or sputter probability Y_a. Thus, the probability per unit time P_s for sputter removal of individual seed atoms from the substrate is

$$P_s = Y_aR_i\sigma_a \ . \tag{4-5}$$

The reciprocal of this probability per unit time is then the mean adsorption lifetime for a seed atom on the substrate

$$\tau_a = \frac{1}{P_s} = 1/Y_aR_i\sigma_a \ . \tag{4-6}$$

A first estimate of τ_a can be obtained by inserting approximate values for the quantities of Eq. (4-6). For a loosely bonded and mobile seed atom, the sputtering yield Y_a should be near unity. The cross section σ_a can be approximated as $N_o^{-2/3}$, where N_o is the atomic density of the substrate with a typical value of $10^{29}m^{-3}$.[10] The value of R_i for a typical 10 A/m^2 (1 mA/cm^2) ion beam current density is about 6×10^{19} $(m^2\text{-sec})^{-1}$. With these substitutions an adsorption time of about 1/3 sec is obtained.

Seed atoms of interest in the process of sputter cone formation must be mobile. The seed atoms should therefore exhibit weaker bonding to the substrate than that of the substrate atoms to one another.

Because of this relatively weak bonding for seed atoms, the characteristic time τ_o for a seed atom to jump between adsorption sites should be a function of this bonding interaction, rather than the substrate lattice vibrations to which it is only loosely coupled. Considering a seed atom at an adsorption site, the site can be thought of as a potential well within which the seed atom is bound. The potential barrier between adjacent sites is the activation energy E_d. Motion along the surface should therefore be characterized by a well depth E_d and an approximate periodicity. Using a_o as the average spacing between sites, a sinusoidal representation of a periodic, undulating potential is

$$U(r) \approx E_d(1-\cos 2\pi r/a_o)/2 \ . \tag{4-7}$$

A parabolic potential results from retaining only the first two terms in the cosine series expansion.

$$U(r) \approx \pi^2 E_d r^2/a_o^2 \tag{4-8}$$

Using m_s as the mass of the seed atom, the equation of motion is

$$m_s d^2r/dt^2 = -\partial U(r)/\partial r = -2\pi^2 E_d r/a_o^2 \ , \tag{4-9}$$

which implies an harmonic oscillation frequency of

$$\nu = (E_d/2m_s a_o^2)^{\frac{1}{2}} \ , \tag{4-10}$$

or a period of

$$\tau_o = (2m_s a_o^2/E_d)^{\frac{1}{2}} . \qquad (4\text{-}11)$$

A numerical estimate of τ_o can be obtained using the appropriate substitutions. The distance a_o can be approximated as $N_o^{-1/3}$, with N_o again the atomic density. The mass m_s of a representative heavy seed atom can be taken as 3×10^{-25} kg, while the activation energy E_d may be assumed to be in the neighborhood of 1.6×10^{-19} J (1 eV).[11] With these substitutions, τ_o is found to be about 4×10^{-13} sec.

Using Eqs. (4-6) and (4-11) to substitute for τ_a and τ_o in Eq. (4-3):

$$r_d = (E_d/2m_s)^{\frac{1}{4}}(a_o/R_i Y_a \sigma_a)^{\frac{1}{2}}\exp(-E_d/2kT) . \qquad (4\text{-}12)$$

With the substitutions of $N_o^{-1/3}$ and $N_o^{-2/3}$ for a_o and σ_a, together with unity for Y_a, a simplified expression is obtained,

$$r_d = (E_d/2m_s)^{\frac{1}{4}}(N_o^{1/3}/R_i)^{\frac{1}{2}}\exp(-E_d/2kT) . \qquad (4\text{-}13)$$

The exponential factor varies rapidly over a wide range. The square-root factor is much more slowly varying, so that numerical values may be substituted therein for a first approximation. Making the substitutions of 1.6×10^{-19} J for E_d, 10^{29} m^{-3} for N_o, 3×10^{-25} kg for

m_s and 6×10^{19} $(m^2\text{-sec})^{-1}$ for R_i in the square-root factor,

$$r_d = 2 \times 10^{-4} \exp(-E_d/2kT) \ . \quad (m) \qquad (4\text{-}14)$$

This, then, is an estimate of the radius over which surface diffusion can be expected to take place. This radius is a function primarily of the activation energy E_d and the substrate temperature. Other factors such as seed atom mass m_s, ion flux R_i, and the adsorption site spacing a_o are considerably less important. The activation energy is a function of the seed-substrate material combination (together with a small temperature effect) and ranges from about 0.5 to 2 eV for metallic materials of interest for seeding.[12] The large variation of r_d with temperature is shown in Fig. 4-5 for this range of activation energies. It can be seen that relatively modest temperature changes can have a profound effect on the mean seed diffusion radius.

A distance equal to twice the average diffusion radius can be used as a measure of the average separation between clusters. If clusters were, on the average, much farther apart than $2r_d$, more clusters would begin to nucleate and grow in the intervening spaces where seed densities were enhanced, thus narrowing the gaps between clusters. At the other extreme, if clusters began to nucleate at separations much less than $2r_d$, larger clusters would grow faster and intercept diffusing seed material at the expense of smaller clusters. Thus, an average cluster separation of about $2r_d$ would be expected to be stable.

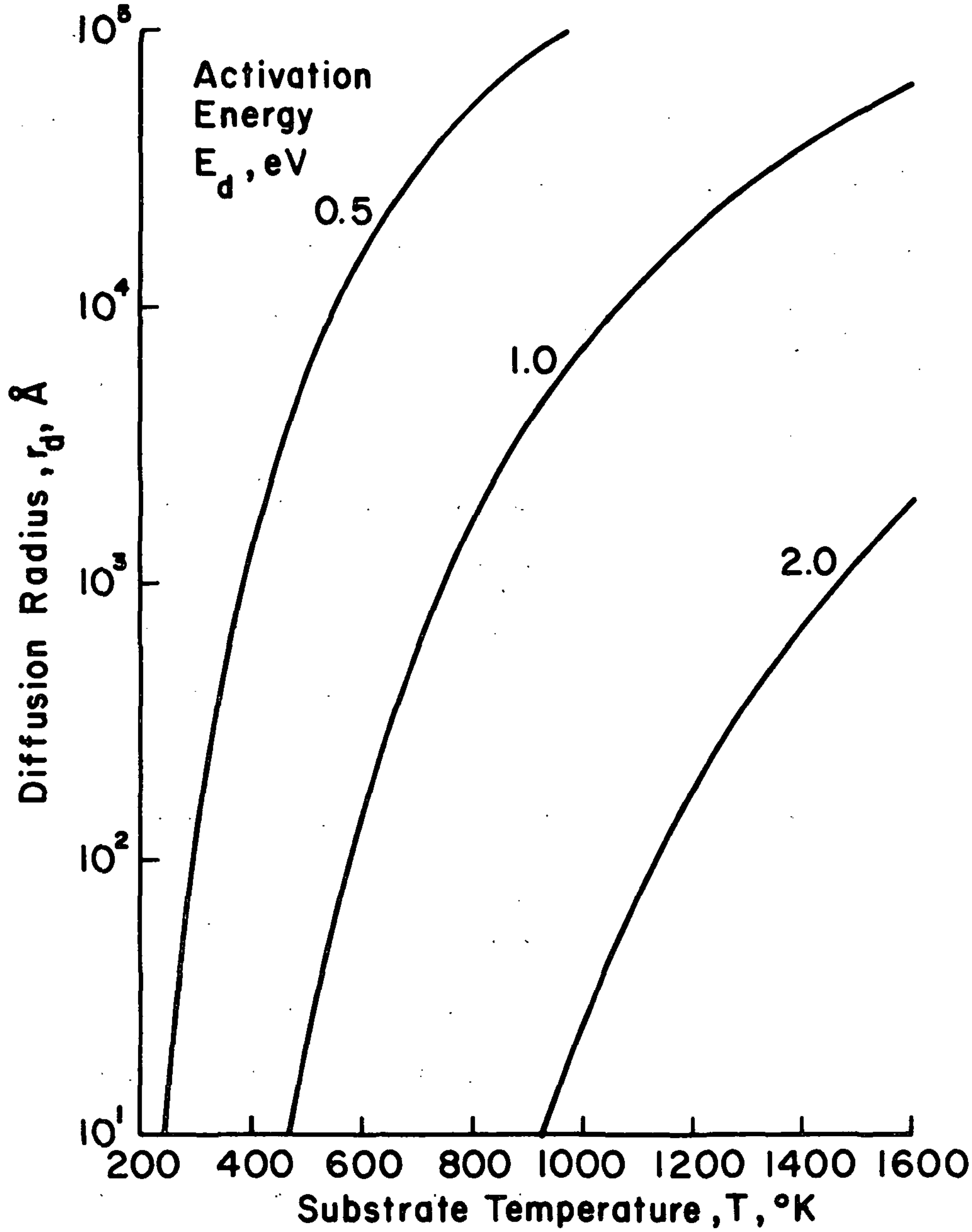

Figure 4-5. Diffusion radius as a function of activation energy and substrate temperature for a specific case.

Seed Clustering

Having found the radius from which diffusion will supply a seed cluster, it is appropriate to consider the stability of that cluster. There is a critical size of a seed cluster, below which steady growth is not possible.[13] This critical radius is essentially the same value as is used in nucleation theory. It is obtained by setting to zero the derivative of free energy (surface plus volume) with respect to radius.[14] Continuous growth can take place above this radius, but dissociation of the cluster will tend to occur at smaller radii.

Whether or not a seed cluster is stable will therefore depend on the diffusion rate to the cluster being sufficient, or insufficient, to supply the sputtering loss from a cluster of critical radius. To determine the stability requirements of seed clusters it is necessary to investigate more closely the processes of seed movement, and clustering while adsorbed on a substrate.

Seed atoms are assumed to move from adsorption site to adsorption site on the surface by a random walk process. Only those seed atoms that acquire an energy greater than E_d are mobile. Energy is exchanged between seed atoms and the lattice through the loose coupling of the seed atom to thermal lattice vibrations bringing the adsorbed seed atom population into approximate thermal equilibrium with the substrate lattice. It is then the temperature of the substrate that governs the fraction of seed atoms that are mobile at any given time. A random walk process for seed motion requires that, on the average, seed atoms experience an inelastic "collision" as a result of each jump to a neighboring adsorption site. The energy loss in the inelastic process would then be associated with a loss of the initial direction of motion resulting in a random direction for the next jump. Regarding each jump to a neighboring adsorption site as an independent event terminating with directional and energy losses can be further supported by considering the adsorption bonding forces tending to accelerate a seed atom down into the neighboring adsorption site once it has cleared the potential barrier E_d, where E_d is the diffusion activation energy. It is improbable that the incoming seed velocity vector would be sufficiently well-aligned with the spatial symmetry of the neighboring adsorption site to proceed without significant deflection.

To appropriately model the clustering of seed atoms, it is first necessary to characterize the mean speed for the surface migration of seed atoms. There are different characteristic velocities of mobile seed atoms. One velocity, designating the micro-velocity υ_m, could be derived from the spacing of adsorption sites and the jump time,

$$\upsilon_m = \frac{a_o}{\tau_o} \tag{4-15}$$

or, using Eq. (4-11),

$$\upsilon_m = (E_d/2m_s)^{\frac{1}{2}} \, . \tag{4-16}$$

Substituting 1 eV for E_d and 3×10^{-25} Kg for m_s yields,

$$\upsilon_m = 5.2 \times 10^2 \text{ m/sec} \, . \tag{4-17}$$

Another velocity, designated macro-velocity υ_M, can be obtained from the random walk diffusion radius and the mean adsorption time,

$$\upsilon_M = r_d/\tau_a \tag{4-18}$$

or, using Eqs. (4-6) and (4-13),

$$\upsilon_M = (E_d/2m_s)^{\frac{1}{4}}(R_iY_a^{\ 2}/N_o)^{\frac{1}{2}}\exp(-E_d/2kT) \ . \tag{4-19}$$

Using the representative values of 1 eV for E_d, $6 \times 10^{19}\ m^{-2}\ sec^{-1}$ for R_i, 1 for Y_a, 3×10^{-25} Kg for m_s, $10^{29}\ m^{-3}$ for N_o, and 800°K for T we get

$$\upsilon_M = 4.0 \times 10^{-7}\ m/sec \ . \tag{4-20}$$

This is nine orders of magnitude less than υ_m. Perhaps a more appropriate expression for the seed velocity, for seed clustering, would take into account the total distance of travel found by summing all jumps taken in a seed lifetime τ_a. The number of jumps is given by Eq. (4-2):

$$n = (\tau_a/\tau_o)\exp(-E_d/kT) \ , \tag{4-21}$$

and the mean seed speed is:

$$\upsilon_s = na_o/\tau_a \ , \tag{4-22}$$

or, using Eqs. (4-21) and (4-11)

$$\upsilon_s = (E_d/2m_s)^{\frac{1}{2}} \exp(-E_d/kT) \ , \tag{4-23}$$

or,

$$\upsilon_s = 2.6 \times 10^{-4} \text{ m/sec} \tag{4-24}$$

with the usual substitutions. Equation (4-23) is the appropriate expression for average seed velocity for the purpose of understanding diffusion and clustering.

With an expression for seed velocity, the detailed movements of seed atom populations will now be considered. As a first example, an estimate for the upper bound of the areal density of seed atoms on the substrate, N_s, can be obtained by assuming that clusters fail to form on a seeded surface. In the absence of seed clusters, a steady state will be reached with the seed deposition rate and the re-sputtering rate being equal. The seed flux R_s (seed atoms deposited/m^2-sec) can be written in terms of the ion flux using a factor F_s, the seeding fraction, that reflects the ratio of seed deposition to ion flux:

$$R_s = F_s R_i \ . \tag{4-25}$$

The seeding rate is discussed in detail in Appendix B. The rate of seed removal by physical sputtering S_s is the probability per unit time for sputtering an individual seed atom multiplied by the areal seed density N_s.

$$S_s = Y_a R_i \sigma_a N_s \ . \qquad (4\text{-}26)$$

Equating the deposition and sputter removal rates gives,

$$F_s R_i = Y_a R_i \sigma_a N_{s_{max}} \ , \qquad (4\text{-}27)$$

where $N_{s_{max}}$ is the maximum achievable areal seed density in the absence of clustering. Solving for $N_{s_{max}}$:

$$N_{s_{max}} = F_s / Y_a \sigma_a \ . \qquad (4\text{-}28)$$

With a value of 0.01 for F_s (see Appendix B) this expression yields, using the previous substitutions:

$$N_{s_{max}} \approx 2 \times 10^{17} \ m^{-2} \ . \qquad (4\text{-}29)$$

We can also look at the fraction of surface coverage by seed atoms. Since $1/\sigma_a$ is approximately the density of adsorption sites we get

$$F_s N_a \approx N_s \qquad (4\text{-}30)$$

where Y_a has been assumed to be approximately 1 and N_a is the adsorption site density. Thus, the maximum fractional surface coverage by seed material is about equal to the seeding fraction F_s.

A more detailed analysis is necessary when clusters are assumed to be present on the substrate. Figure (4-6) represents a cluster and its surrounding seed diffusion area. The various $\dot{N}$'s shown in Fig. (4-6) are flow rates of seed atoms in atoms/sec. Let N_c be the area density of seed clusters, then $1/N_c = A = A_c + A_d$, where A_c is the cluster area and A_d is the diffusion 'drawing' area. The definitions of the seed flow rates are in Table 4-1.

Table 4-1. Seed Flow Rates.

$\dot{N}_1$	Seed atom deposition rate into area A_d
$\dot{N}_2$	Seed atom deposition rate into area A_c
$\dot{N}_3$	Rate of seed atom acquisition by the cluster
$\dot{N}_4$	Rate of re-sputtering of seed atoms from A_d
$\dot{N}_5$	Rate of re-sputtering of seed atoms from A_c
$\dot{N}_6$	Rate of diffusion of seed atoms out of A_d
$\dot{N}_7$	Rate of diffusion of seed atoms into A_d

All rates, N_i are positive with the direction of seed flow indicated by the arrows in Fig. 4-6.

A steady state situation will be considered first. Under steady state conditions, the following relations hold:

$$\dot{N}_6 = \dot{N}_7 \tag{4-31}$$

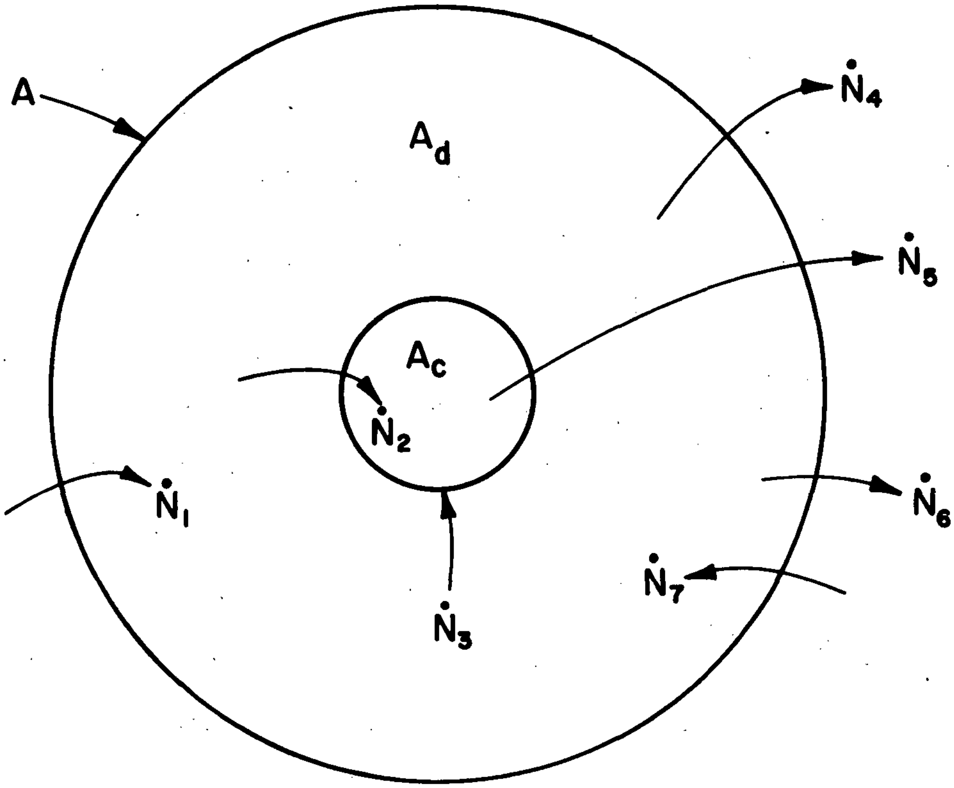

Figure 4-6. Geometrical representation of a cluster of seed atoms of area A_c with the surrounding area A_d. Seed atom fluxes are represented by arrows.

$$\dot{N}_1 + \dot{N}_2 = \dot{N}_4 + \dot{N}_5 \qquad (4\text{-}32)$$

$$\dot{N}_1 - \dot{N}_4 = \dot{N}_3 \qquad (4\text{-}33)$$

$$\dot{N}_2 + \dot{N}_3 = \dot{N}_5 \; . \qquad (4\text{-}34)$$

Equation (4-31) simply expresses the symmetry of seed diffusion into and out of the area A containing a single cluster. Equation (4-32) equates the total seed deposition rate to the total sputter removal rate in area A. Equation (4-33) relates the net seed flux into A_d (taking re-sputtering into account) to the diffusion flux from A_d to the cluster. Finally, Eq. (4-34) equates the total flux to the cluster to the total sputtering from the cluster. Equation (4-32) can be obtained by eliminating $\dot{N}_3$ between Eqs. (4-33) and (4-34).

Most of the individual rates can be obtained from consideration of simple sputtering rates:

$$\dot{N}_1 = R_i F_s A_d \qquad (4\text{-}35)$$

$$\dot{N}_2 = R_i F_s A_c \qquad (4\text{-}36)$$

$$\dot{N}_4 = R_i Y_a \sigma_a N_s A_d \qquad (4\text{-}37)$$

$$\dot{N}_5 = R_i Y_c A_c \; , \qquad (4\text{-}38)$$

where Y_c is the sputter yield of atoms from the seed cluster and the sticking coefficient for all deposited atoms is assumed to be 1. $\dot{N}_3$ is related to the 'collision' frequency of seeds with clusters. Assuming that each seed colliding with a cluster adheres we can use a length of $2r_c$ to describe the two-dimensional cluster interaction cross section where r_c is the cluster radius.

$$\dot{N}_3 = 2r_c \upsilon_s N_c N_s A_d \tag{4-39}$$

This relation can be understood more simply by noting that $2r_c \upsilon_s N_c$ is the collision frequency for a single seed moving through clusters of density N_c at a speed υ_s. Multiplying by the number of seed atoms per unit area gives the total frequency of seed-cluster collisions per unit area. Multiplying by the "drawing" area A_d for a single cluster gives the number of collisions with one cluster per unit time.

With substitutions for the various rates, Eqns. (4-33) and (4-34) can be rewritten as:

$$R_i F_s A_d - R_i Y_a \sigma_a N_s A_d = 2r_c \upsilon_s N_c N_s A_d \tag{4-40}$$

and

$$R_i F_s A_c + 2r_c \upsilon_s N_c N_s A_d = R_i Y_c A_c \tag{4-41}$$

These equations may be solved simultaneously for the drawing area A_d and for the surface seed density N_s.

$$A_d = \frac{A_c(Y_c - F_s)(2r_c\upsilon_s + A_c Y_a \sigma_a R_i)}{2r_c\upsilon_s F_s - A_c(Y_c - F_s)Y_a\sigma_a R_i} \tag{4-42}$$

$$N_s = \frac{A_c(Y_c - F_s)R_i}{2r_c\upsilon_s}\left(1 + A_c/A_d\right) . \tag{4-43}$$

Under typical seeding and sputtering conditions the additive terms in Eq. (4-42) involving the ion arrival rate can be neglected giving:

$$A_d \approx A_c(Y_c - F_s)/F_s . \tag{4-44}$$

Physically, this approximation corresponds to the actual seed coverage between clusters being much smaller than the maximum possible coverage. Equation (4-44) can be written in terms of r_d assuming circular geometry.

$$r_d = r_c[(Y_c - F_s)/F_s]^{\frac{1}{2}} \tag{4-45}$$

This is the required diffusion radius to sustain a seed cluster of critical radius r_c. For most applications, $F_s \ll Y_c$, so that F_s may often be neglected in the numerator with little error.

Critical Temperature

This diffusion radius (Eq. (4-45)) can be equated to that of Eq. (4-12) to determine the minimum substrate temperature that will give the required diffusion to sustain clusters of the minimum size.

$$T_c = E_d/k\ell n \left[(E_d/2m_s)^{\frac{1}{2}} \left(F_s N_o^{1/3}/R_i Y_a r_c^{\,2} (Y_c - F_s) \right) \right] \qquad (4\text{-}26)$$

The logarithmic factor will vary slowly with changes in the variables therein; thus, the activation energy will most strongly dominate the critical temperature. The new variables that have been introduced are the critical radius r_c and the seeding fraction F_s. The seeding fraction is treated in Appendix B, a value of 0.01 will be used as a reasonable approximation. Values of the critical radius range from about 6 to 10 Å.[15] A cross check was made on these values of r_c from another point of view. The use of a critical radius derived from nucleation studies implies perturbations corresponding to thermal energy. The energy of an ion impact in a sputtering environment, however, is far above the thermal level. The limiting condition for ion impact is that the cluster should be large enough to absorb all the ion energy without vaporizing. The heat of sublimation for typical seed materials ranges from about 3 to 9 eV/atom.[16] For typical ion energies of 500 to 1000 eV, then, this minimum cluster radius is about 5 Å to 10 Å assuming a roughly spherical cluster shape. The heat of sublimation is, of course, a macroscopic quantity. However, this calculation indicates that the increase in cluster size to accomodate the maximum perturbation of an ion collision should be moderate, almost certainly less than a factor of two times the nucleation theory radius of 10 Å.

Using 10 Å for r_c and 0.01 for F_s an approximate expression can be obtained for T_c in terms of the activation energy measured in eV for this expression only.

$$T_c \approx 587°K\ E_d \tag{4-47}$$

This expression may be used for rapid estimates and approximations without paying undue attention to the precise values used for some of the other quantities.

Experimental Results and Discussion

Two physical effects following from the cone seeding theory were investigated experimentally: (1) the variation in cone density with substrate temperature, and (2) the existence of a critical temperature for cone formation. In the experiments, samples of aluminum were heated to a specified temperature and sputtered for 20 min. using a 1 mA/cm^2 beam of 500 eV Ar ions, while simultaneously seeding the sample with a source of either Mo or Au. The specified substrate temperatures ranged from 400 to 575°C in different tests, with In used to assure good thermal contact between the samples and the heat source.

Seeding was accomplished by partially covering the sample with a sheet of the seed material. Seed material was then sputtered from the beveled edge of this covering sheet onto the sample. Because of this geometrical arrangement, the seeding intensity decreased with increasing distance from the beveled edge (see Appendix B). After sputtering, scanning electron micrographs were obtained of the sample surfaces. The average separation between cones was then $(A/N)^{\frac{1}{2}}$, where N is the number of cones counted in an area A of the micrograph.

We identify $\langle r \rangle$, one half the average separation between cones, with the diffusion radius r_d in the preceding theory. Figures 4-7 and 4-8 show plots of $\langle r \rangle$ as a function of reciprocal temperature for

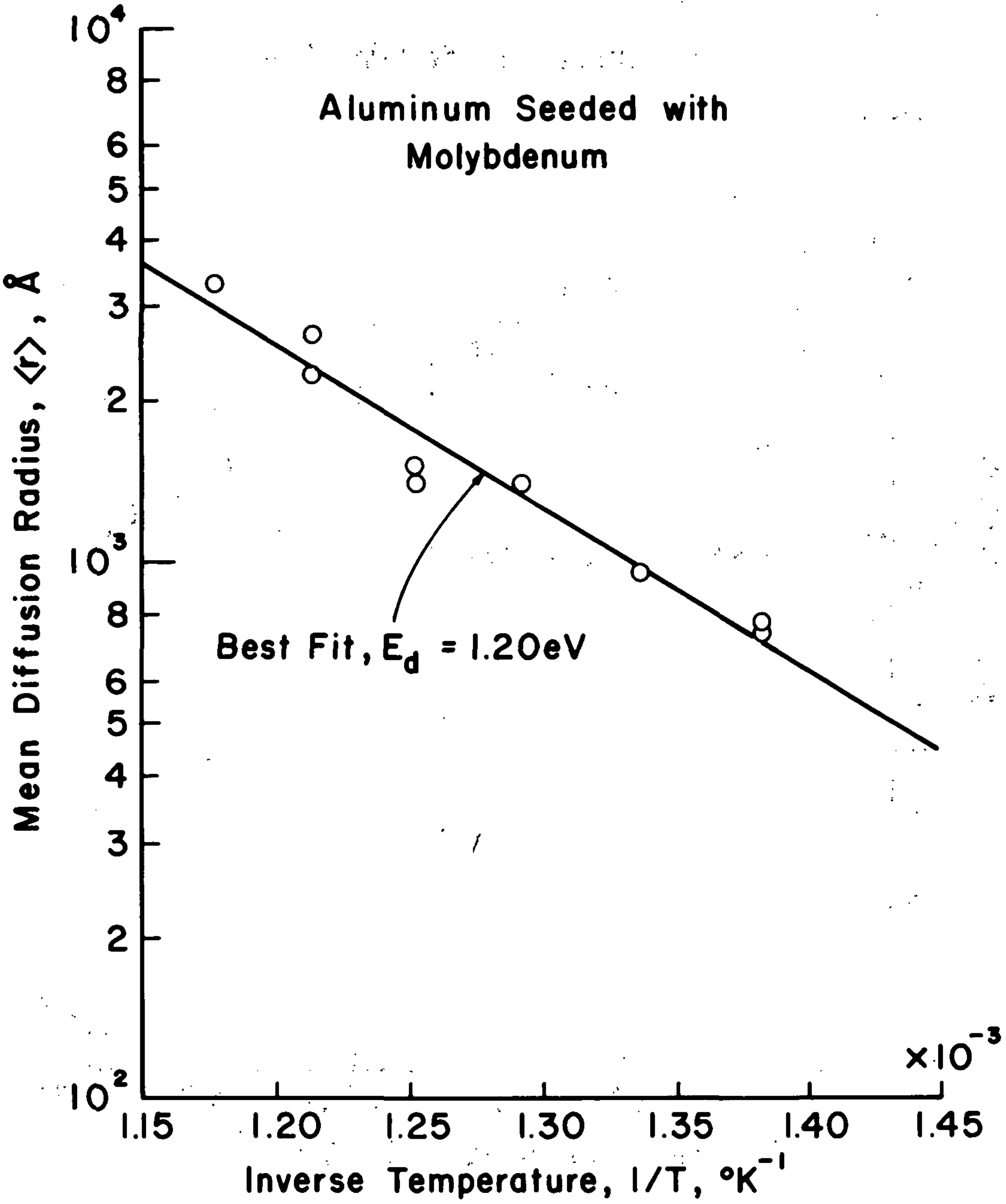

Figure 4-7. Correlation for Al seeded with Mo.

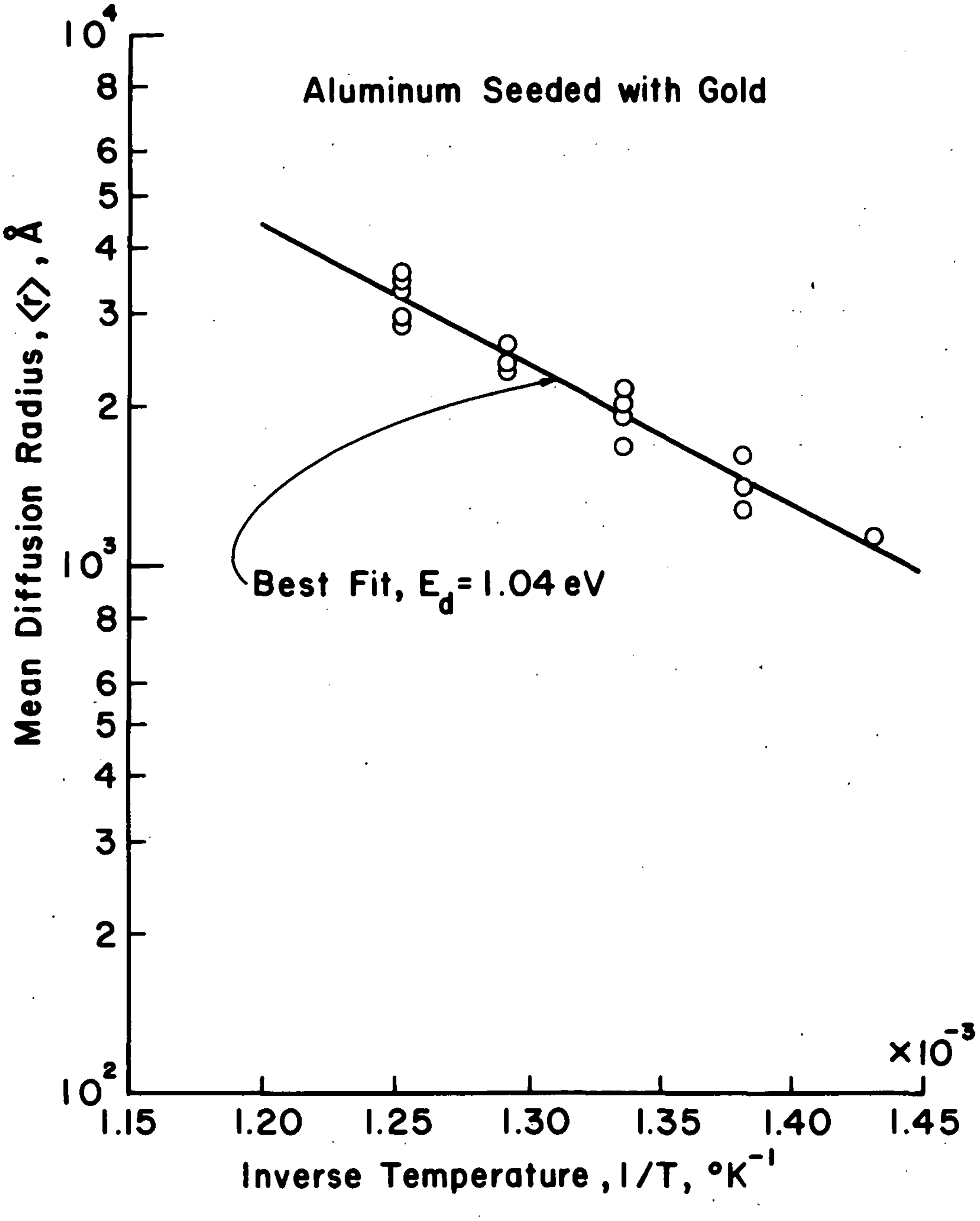

Figure 4-8. Correlation for Al seeded with Au.

the two seed materials. From the theory, we expect straight lines on these plots. This can be shown by rewriting Eq. (4-13) as

$$r_d = r_o \exp(-E_d/2kT) \tag{4-48}$$

where r_o is a constant

$$r_o = (E_d/2m_s)^{\frac{1}{4}} (N_o^{1/3}/R_i Y_a)^{\frac{1}{2}} \ . \tag{4-49}$$

Taking the natural logarithm of Eq. (4-48) and rearranging the result,

$$\ell n\, r_d = (-E_d/2k)\ 1/T + \ln r_o \ . \tag{4-50}$$

This expression is linear if $\ell n\, r_d$ is plotted as a function of inverse temperature, as done in Figs. 4-7 and 4-8. This slope of the line is $-E_d/2k$, while the ordinate intercept is r_o.

A least squares regression line was fitted to each of Figs. 4-7 and 4-8. The best fit corresponded to an E_d of 1.20 eV and an r_o of 1.10 × 10^7 Å for Fig. 4-7 and an E_d of 1.04 eV and an r_o of 6.04 × 10^6 Å for Fig. 4-8. The correlation coefficients exceeded 0.9 for both fits. Experimental critical temperatures were also determined: 700°K for Al seeded with Mo and 675°K for Al seeded with Au.

The qualitative trends shown in Figs. 4-7 and 4-8 are all consistent with theory. The data shown also include varying distances from the edge of covering sheet, which corresponded to different seed ratios F_s. The only data selection used was that regions far enough from the covering sheet (low enough seed ratio) showed large fractions of the areas without cones and were omitted. For regions with sufficient seed to show fully developed cone structures, then, the effect of seed fraction F_s on cone spacing must be small. This result is in agreement with Eq. (4-13), which does not include F_s as a variable. Activation energies for surface diffusion were not available from literature for the exact combinations of materials used, but the values obtained from the slopes of Figs. 4-7 and 4-8 are in qualitative agreement with other combinations that have been studied using standard diffusion measurement techniques.

The activation energies from Figs. 4-7 and 4-8 can be used for a more quantitative comparison of experimental results with theory. Using these activation energies together with 6.24×10^{19} ions/m^2-sec for R_i, .01 for F_s, 1×10^{-10}m for r_c, and handbook values for other variables including using bulk sputter yields, theoretical values were calculated for r_o and the critical temperature. These values were 2.21×10^6 Å and 684°K for Al seeded with Mo and 1.78×10^6 Å and 646°K for Al seeded with Au. The agreement for critical temperature is close, with experimental values being 2 and 4 percent above the theoretical values for Eq. (4-46). This close agreement is due in part to most of the variables in Eq. (4-46) being included in a logarithmic factor. Closer agreement is to be expected between the predictions of the model and experimental results for the critical temperature than for other aspects of the model. For example, a limiting case of a flat surface as used in this model is more appropriate for derivation of the critical temperature at which no cones are present than for determining cone separation on a fully developed surface. The agreement for cone spacing is less close, with experimental values of r and cone spacing being 3 to 5 times the theoretical ones from Eq. (4-13). This difference may be the result of theory being derived for a flat isotropic surface, while the experimental values were for well developed conical surfaces. The cascades of sputtered substrate atoms on the conical surfaces would be expected to reduce seed diffusion toward the apexes, resulting in the reduction of some seed clusters below the critical size.

The choice of materials for Fig. 4-8 also represents support for the theory. Previous descriptions of coning state that low sputter yield materials protected the apexes of cones in higher sputter yield substrates. The present theory indicates that the seed can have a higher sputter yield than the substrate if the seed material is sufficiently mobile to replenish the sputtering loss from a seed cluster. The Au seed in Fig. 4-8 has a much higher yield than the Al substrate, so that this result is an example of coning that was predicted by the present theory.

A texturing theory based on surface diffusion has shown substantial agreement with experimental results. The existence of a minimum substrate temperature for texturing, the variation of cone spacing with temperatures and the texturing with a high sputter yield seed on a lower sputter yield substrate were all predicted by this theory. This theory has obvious utility in the production of textured surfaces for applications such as low reflectance solar cells, high emissivity heat radiators, and medical implants. The existence of a minimum critical temperature for coning is also important for the production of smooth surfaces, in that a sufficient reduction in surface temperature should reduce the mobility of any seed material enough to avoid coning, whether the seeding is due to stray sputtering or one of the elements in the substrate material. Due to the continual cleaning of the surface by the bombarding specie, the coning process also permits evaluation of the surface diffusion activation energy under conditions of extreme cleanliness.

V. CONCLUDING REMARKS

The theory and experimental evidence presented here can have application in ion thruster work or in alternative types of plasma devices. However, the desire to increase understanding of the physical processes important in directed ion beam sputtering has been paramount. An increased understanding of basic processes has come in three main areas: (1) reliable discharge chamber design, (2) directed ion beam interactions, and (3) the physical texturing of surfaces on a micron and sub-micron scale.

Discharge chambers can now be designed and constructed with a considerably increased confidence that is largely the result of an almost complete decoupling of the bulk plasma from the magnetic fields used for containment. This decoupling has yielded a tractable configuration in terms of theoretical analysis. The enhanced plasma and beam uniformity expected with a large multipole design have been obtained experimentally, along with the observation that the bulk of the discharge plasma is exceptionally quiet when DC heaters are employed. The integrated magnetic field necessary to contain primary electrons has been determined theoretically and three multipole ion sources designed to meet this criterion have performed well. Of particular interest is the absence of numerous iterations in the design and construction of new multipole chambers, in sharp contrast with the cut and try approach used so often in the past. The question of Maxwellian electron conduction across the multipole field has been treated satisfactorily as a simple additional requirement for a sufficient anode area for electron collection. This requirement, then, allows stable operation without a large forward potential at the anodes to drive the electron diffusion. Although these analyses have been directed principally at multipole chambers, many of the concepts and trends seen here are equally valid for other magnetic field designs.

Interaction cross sections for energetic collisions of rare gas atoms have been calculated from isolated pair potentials, and, in the case of Ar charge exchange, obtained from the literature. The energy and momentum transfer cross sections were previously unavailable and are substantially smaller than the thermal values that have occasionally been misleading when used at higher energies. Experimental data have been found to be in agreement with the values for the charge exchange cross section, while the momentum transfer cross section was used somewhat less directly in the analysis of a newly observed sputtering phenomenon in diode plasma devices. The known energy losses in the beam can be used to determine pressure requirements in practical systems as well as allowing a more thorough analysis and understanding of a variety of energetic processes in ion beam and plasma devices.

A model has been developed that describes the process of conical texturing of a surface due to simultaneous directed ion beam etching and sputter deposition of an impurity material. This model accurately predicts both a minimum temperature for texturing to take place and the variation of cone density with temperature. It also provides the correct order of magnitude of the cone separation. It was predicted from the model, and subsequently verified experimentally, that a high sputter yield material could serve as a seed for coning of a lower sputter yield substrate material if the seed were sufficiently mobile on the surface. The specific combination reported was gold seed on an aluminum substrate. Seeding geometries and seed deposition rates were studied to obtain an important input to the theoretical texturing model and to permit rapid and effective application of the coning model to specific experiments.

REFERENCES

Chapter I

1. R. E. Lee, "Microfabrication by Ion Beam Etching", TFWM-1, 25th Nat. Sym. Am. Vac. Soc., San Francisco (Nov. 1978).

2. S. M. Kane and K. Y. Ahn, "Characteristics of Ion Beam Sputtered Thin Films", TFWM-3, 25th Nat. Sym. Am. Vac. Soc., San Francisco (Nov. 1978).

3. H. R. Kaufman and R. S. Robinson, "Ion Beam Texturing of Surfaces", TFWM-4, 25th Nat. Sym. Am. Vac. Soc., San Francisco (Nov. 1978).

4. H. R. Kaufman, J.M.E. Harper, and J. J. Cuomo, "Focused Ion Beam Designs for Sputter Deposition", TFWM-5, 25th Nat. Sym. Am. Vac. Soc., San Francisco (Nov. 1978).

5. J. Franks, "Properties and Applications of Saddle-Field Ion Sources", TFWM-6, 25th Nat. Sym. Am. Vac. Soc., San Francisco (Nov. 1978).

6. R. N. Castellano, L. G. Feinstein, "Ion Beam Deposition of Thin Films of Ferro-Electric Lead Zirconate Titante (PZT)", TFWM-7, 25th Nat. Sym. Am. Vac. Soc., San Francisco (Nov. 1978).

7. R. S. Robinson, "Energetic Binary Collisions in Rare Gas Plasmas", TFWM-8, 25th Nat. Sym. Am. Vac. Soc., San Francisco (Nov. 1978).

8. L. E. Bradley and J. R. Sites, "Silicon Nitride Layers on Gallium Arsenide by Low Energy Ion Beam Sputtering", TFWM-9, 25th Nat. Sym. Am. Vac. Soc., San Francisco (Nov. 1978).

9. J. Mirtich and J. S. Sovey, "Adhesive Bonding of Ion Beam Textured Metal and Fluoropolymers", ETHM-1, 25th Nat. Sym. Am. Vac. Soc., San Francisco (Nov. 1978).

10. J. S. Sovey, "Ion Beam Sputtering of Fluoropolymers", ETHM-2, 25th Nat. Sym. Am. Vac. Soc., San Francisco (Nov. 1978).

11. W. W. Molzen, A. N. Broers, J. J. Cuomo, J. M. E. Harper, and R. B. Laibowitz, "Materials and Techniques used in Nanostructure Fabrication", TFTHM-3, 25th Nat. Sym. Am. Vac. Soc., San Francisco (Nov. 1978).

12. H. R. Kaufman, "Technology of Ion Beam Sources used in Sputtering", J. Vac. Sci. Technol., Vol. 15, 272-278 (1978).

13. R. S. Robinson, "Thirty-Centimeter-Diameter Ion Milling Source", J. Vac. Sci. Technol., Vol. 15, 277-280 (1978).

14. J. M. E. Harper, "Ion Beam Deposition", in Thin Film Processes, Academic Press, pp. 175-206 (1978).

15. H. R. Kaufman, "Technology of Electron-Bombardment Ion Thrusters", in Advances in Electronics and Electron Physics, Academic Press (1974).

16. K. Atkins, C. Terwilliger, "Ion Drive: A Step Toward "Star Trek", AIAA Paper No. 76-1069, (Nov. 1976).

17. J. R. Beattie and P. J. Wilbur, "Cusped Magnetic Field Mercury Ion Thruster", J. Spacecr. Roc., Vol. 14, 747-755 (1977).

18. G. Aston, H. R. Kaufman, and P. J. Wilbur, "Ion Beam Divergence Characteristics of Two-Grid Accelerator Systems", AIAA Journal, Vol. 16, 516-524 (1978).

19. G. C. Isaacson and H. R. Kaufman, "15-cm Multipole Gas Ion Thruster", J. Spacecr. Roc., Vol. 14, 469-473 (1977).

20. R. R. Peters and P. J. Wilbur, "Mercury Ion Thruster Doubly Charged Ion Model", AIAA Paper, No. 76-1010 (Nov. 1976).

21. L. Rehn and H. R. Kaufman, "Correlation of Inert Gas Hollow Cathode Performance", AIAA Paper, No. 78-707 (1978).

22. D. E. Siegfried and P. J. Wilbur, "An Investigation of Mercury Hollow Cathode Phenomena", AIAA Paper, No. 78-705 (1978).

23. G. R. Longhurst, Prediction of Plasma Properties in Mercury Ion Thrusters, NASA CR-159448 (1978).

Chapter II

1. H. R. Kaufman, "Technology of Electron-Bombardment Ion Thrusters", in Advances in Electronics and Electron Physics, Vol. 36 (1974).

2. J. R. Beattie, Cusped Magnetic Field Mercury Ion Thruster, NASA CR-135047 (July 1976).

3. J. R. Beattie and P. J. Wilbur, "Cusped Magnetic Field Mercury Ion Thruster", J. Spacecr. Roc., Vol. 14, 747-755 (1977).

4. G. C. Isaacson and H. R. Kaufman, "15-cm Multipole Gas Ion Thruster", J. Spacecr. Roc., Vol. 14, 469-473 (1977).

5. R. D. Moore, "Magneto-Electrostatically Contained Plasma Ion Thruster", AIAA Paper No. 69-260 (1969).

6. W. D. Ramsey, "12-centimeter Magneto-Electrostatic Containment Mercury Ion Thruster Development", AIAA Paper No. 71-692 (1971).

7. N. A. Krall and A. W. Trivelpiece, Principles of Plasma Physics, McGraw-Hill, Chapter 6 (1973).

8. G. Medicus, "Simple Way to Obtain the Velocity Distribution of the Electrons in Gas Discharge Plasmas from Probe Curves", J. Appl. Phys., Vol. 27, 1242-1248 (1956).

9. A. R. Martin, "Electron Energy Distributions in an Ion Engine Discharge", J. Spacecr. Roc., Vol. 8, 548-550 (1971).

10. F. F. Chen, Introduction to Plasma Physics, Plenum Press, Chapter 2 (1975).

11. J. R. Beattie, "Numerical Procedure for Analyzing Langmuir Probe Data", AIAA Jour., Vol. 13, pp. 950-952 (1975).

12. F. F. Chen, Introduction to Plasma Physics, Plenum Press, Chapter 5 (1975).

13. D. Bohm, "Qualitative Description of the Arc Plasma in a Magnetic Field", in The Characteristics of Electrical Discharges in Magnetic Fields (A. Guthrie and R. K. Wakerling, eds.) McGraw-Hill Book Co., pp. 1-12, (1949).

14. L. Spitzer, Jr., Physics of Fully Ionized Gases, 2nd ed., Interscience Publishers, N. Y., pp. 47-48 (1962).

15. F. F. Chen, Introduction to Plasma Physics, Plenum Press, N. Y., p. 169 (1974).

16. G. C. Isaacson, Multipole Gas Thruster Design, NASA CR-135101, pp. 45-51 (1977).

17. C. M. Haynes, "Fifteen cm Ion Source", in Industrial Ion Source Technology, (H. R. Kaufman, ed.), NASA Contr. Rep. CR-135353, pp. 18-23 (Nov. 1977).

18. H. R. Kaufman, "Charge-Exchange Plasma Generated by an Ion Thruster", NASA Contr. Rep. CR-135318, (Dec. 1977).

Chapter III

1. R. S. Robinson, "Thirty-Centimeter-Diameter Ion Milling Source", J. Vac. Sci. Technol., 15, 277-280 (1978).

2. J. J. Cuomo, R. J. Gambino, J. M. E. Harper, J. D. Kuptsis, and J. C. Webber, "Significance of Negative Ion Formation in Sputtering and SIMS Analysis", J. Vac. Sci. Technol., 15, 281-287 (1978).

3. H. R. Kaufman, "Technology of Ion Beam Sources used in Sputtering", J. Vac. Sci. Technol., 15, 272-276 (1978).

4. J. M. E. Harper, J. J. Cuomo, R. J. Gambino, H. R. Kaufman, and R. S. Robinson, "Mean Free Path of Negative Ions in Diode Sputtering", J. Vac. Sci. Technol., 15, 1597-1600 (1978).

5. R. S. Robinson and C. M. Haynes, "Surface Texturing", Industrial Ion Source Technology, NASA CR-135353, 24-75 (1978).

6. P. J. Wilbur, "Argon-Xenon Discharge Chamber Model for the Production of Doubly Charged Ions", Inert Gas Thrusters, NASA CR-135226, 46-64 (1977).

7. R. J. McDonald and D. Haneman, "Depths of Low-Energy Ion Bombardment Damage in Germanium", J. Appl. Phys., 37, 1609-1613 (1966).

8. G. R. Brewer, Ion Propulsion Technology and Applications, 78-80, Gordon and Breach (1970).

9. L. Spitzer, Jr., Physics of Fully Ionized Gases, 148-151, Interscience (1962).

10. I. Popescu Iovitsu and N. Ionescu-Pallas, "Resonant Charge-Exchange and the Kinetics of Ions", Sov. Phys.-Tech.-Phys., 4, 781-791 (1960).

11. D. Rapp and W. E. Francis, "Charge Exchange between Gaseous Ions and Atoms", J. Chem. Phys., 37, 2631-2645 (1962).

12. D. Zuccaro, Measurement of the Charge Exchange Cross Section of Mercury, NASA CR-72398.

13. J. A. Dillon, Jr., W. F. Sheradin, H. D. Edwards, and S. N. Ghosh, "Charge Transfer Reactions in Monatomic and Diatomic Gases", J. Chem. Phys., 23, 776-779 (1955).

14. J. B. Hasted, "The Exchange of Charge between Ions and Atoms", Proc. Roy. Soc. (London) A205, 421 (1951).

15. Potter, R. F., "Cross Sections for Charge Transfer Collisions of Low-Energy Ions in N_2 and O_2", J. Chem. Phys., 22, 974-979 (1954).

16. R. M. Kushnir, B. M. Palyukh, and L. A. Sena, "Investigation of Resonance Charge Exchange in Monatomic Gases and Metal Vapors", Bull. Acad. Sci. USSR Phys. Ser., 23, (1959).

17. H. R. Kaufman, "Interaction of a Solar Array with an Ion Thruster Due to the Charge-Exchange Plasma", NASA CR-135099, (Oct. 1976).

18. H. Goldstein, Classical Mechanics, Addison-Wesley, pp. 58-82 (1950).

19. R. D. Evans, The Atomic Nucleus, McGraw-Hill, p. 834 (1955).

20. J. A. Barker, R. A. Fisher and R. O. Watts, "Liquid Argon: Monte Carlo and Molecular Dynamics Calculations", Molecular Physics, Vol. 21, 657-673 (1971).

21. F. W. Bingham, "Classical Calculation of Atomic Scattering Parameters", J. Chem. Phys., Vol. 46, 2003 (1967).

22. F. W. Bingham, "Tabulation of Atomic Scattering Parameters Calculated Classically from a Screened Coulomb Potential", Sandia Corporation Research Report SC-RR-66-506, (August 1966).

23. E. Everhart, R. J. Carbone, and Gerald Stone, "Differential Cross-Section Measurements for Large-Angle Collisions of Helium, Neon and Argon Ions with Argon Atoms at Energies to 100 keV", Phys. Rev., Vol. 98, 1045 (1955).

24. E. Everhart, G. Stone, and R. J. Carbone, "Classical Calculation of Differential Cross Section for Scattering from a Coulomb Potential with Exponential Screening", Phys. Rev., Vol. 99, 1287 (1955).

25. J. A. Barker, R. O. Watts, J. K. Lee, T. P. Schafer, and Y. T. Lee, "Interatomic Potentials for Krypton and Xenon", J. Chem. Phys., 61, 3081 (1974).

26. H. S. W. Massey and H. B. Gilbody, Electronic and Ionic Impact Phenomena, Vol. IV, Oxford, Clarendon, p. 2354 (1974).

27. H. S. W. Massey and H. B. Gilbody, Electronic and Ionic Impact Phenomena, Vol. IV, Oxford, Clarendon, p. 2338 (1974).

28. W. Aberth and D. C. Lorents, "Elastic Differential Scattering of He^+ Ions by Ne and Ar and of Ar^+ Ions by Ar in the 10-600 eV Range", Phys. Rev., 144, 109-115 (1966).

29. C. V. Heer, Statistical Mechanics, Kinetic Theory, and Stochastic Processes, Academic Press, New York and London, p. 132 (1972).

30. J. M. E. Harper, J. J. Cuomo, R. J. Gambino, H. R. Kaufman, and R. S. Robinson, "Mean Free Path of Negative Ions in Diode Sputtering", J. Vac. Sci. Technol., 15(4), 1597-1600, (July/Aug. 1978).

Chapter IV

1. R. S. Berg and G. J. Kominiak, "Surface Texture by Sputter Etching", J. Vac. Sci. Technol., Vol. 13, No. 1, pp. 403-405, (Jan./Feb. 1977).

2. R. S. Robinson and C. M. Haynes, "Surface Texturing", Industrial Ion Source Technology, NASA CR-135353, pp. 24-75, (Nov. 1977).

3. G. K. Wehner and D. J. Hajicek, "Cone Formation on Metal Targets during Sputtering", J. Appl. Phys., 42, pp. 1145-1149 (Mar. 1971).

4. R. S. Robinson and C. M. Haynes, "Surface Texturing", in NASA Contractor Report CR-135353, (Nov. 1977).

5. J. J. Cuomo, J. F. Ziegler, and J. M. Woodall, "A New Concept for Solar Energy Thermal Conversion", Appl. Phys. Lett., Vol. 26, No. 10, pp. 557-559 (May 1975).

6. B. A. Banks, A. J. Weigand, C. A. Babbush, and C. L. Van Kampen, "Potential Biomedical Applications of Ion Beam Technology", AIAA Paper No. 76-1018, AIAA International Electric Propulsion Conference, Key Biscayne, Florida, (Nov. 14-17, 1976).

7. W. R. Hudson, "Nonpropulsive Applications of Ion Beams", AIAA Paper No. 76-1015, AIAA International Electric Propulsion Conference, Key Biscayne, Florida, (Nov. 14-17, 1976).

8. A. J. Weigand and B. A. Banks, "Ion-Beam-Sputter Modification of the Surface Morphology of Biological Implants", J. Vac. Sci. Technol., Vol. 14, No. 1, pp. 326-331, (Jan./Feb. 1977).

9. W. R. Hudson, "Ion Beam Texturing", J. Vac. Sci. Technol., Vol. 14, No. 1, pp. 286-289 (Jan./Feb. 1977).

10. C. Kittel, Introduction to Solid State Physics, Fifth Edition, John Wiley and Sons, Inc., p. 32 (1976).

11. G. Neumann and G. M. Neumann, Surface Self-Diffusion of Metals, Diffusion Information Center, Bay Village, Ohio, pp. 49-60 (1972).

12. D. B. Butrymowicz, J. R. Manning and M. E. Read, "Diffusion in Copper and Copper Alloys", J. Phys. Chem. Ref. Data, Vol. 2, pp. 643-655 (1973).

13. C. A. Neugebauer, "Condensation, Nucleation, and Growth of Thin Films", in Handbook of Thin Film Technology, pp. 8-3, 8-44 (1970).

14. A. W. Adamson, Physical Chemistry of Surfaces, pp. 372-384 (1976).

15. G. A. Somorjai, Principles of Surface Chemistry, Prentice Hall, Englewood Cliffs, New Jersey, p. 77 (1972).

16. C. B. Eisenhandler and B. M. Siegel, J.A.P., Vol. 37, p. 1613 (March 1966).

Appendix B

1. C. B. Cooper and J. Comas, "Angular Distribution of Sublimed and Sputtered Particles from Ag Single Crystals", J. Appl. Phys., 2891-2895 (Sept. 1965).

2. C. E. Ramer, et al., "Sputtering of Polycrystalline Copper and Silver by 30-170 KeV Argon Ions", J. Appl. Phys., 1673-1680 (June 1964).

3. H. Patterson and D. H. Tomlin, "Experiments by Radioactive Tracer Methods on Sputtering by Rare Gas Ions", Proc. Roy. Soc., A265, 474-488 (1962).

4. G. K. Wehner and D. Rosenberg, "Angular Distribution of Sputtered Material", J. Appl. Phys., 177-179 (Jan. 1960).

5. F. Gronlund and W. J. Moore, "Sputtering of Silver by Light Ions with Energies from 2 to 12 KeV", J. Chem. Phys., 1540-1545 (May 1960).

APPENDIX A

CHARGED PARTICLE MOTIONS IN SPATIALLY INHOMOGENEOUS ELECTRIC AND MAGNETIC FIELDS

Where magnetic fields are introduced to contain or confine charged particles within the volume of a plasma, potential gradients will often develop within the magnetic field region in response to applied voltages, current flow and density gradients. Of particular interest is the case of a spatially localized magnetic field distribution separating a plasma volume of essentially unobstructed flow from a container wall or an electrode.

The equation of motion for a particle of charge q in a time-independent given distribution of fields is:

$$\frac{d^2\vec{r}}{dt^2} = \frac{q}{m}\left(-\vec{\nabla}V(\vec{r}) + \frac{d\vec{r}}{dt} \times \vec{B}(\vec{r})\right) \qquad \text{(A-1)}$$

where $\vec{r}$ is the position vector of a particle with charge to mass ratio q/m, $V(\vec{r})$ is the potential and $\vec{B}(\vec{r})$ is the magnetic induction. Equation (A-1) will, in general, be non-linear and closed form solutions will not exist. It can, however, be integrated to obtain trajectories for prescribed fields using standard Runge-Kutta techniques. In Cartesian coordinates, Eq. (A-1) becomes a set of three second-order coupled equations.

$$\frac{d^2x}{dt^2} = -\frac{q}{m}\frac{\partial V}{\partial x} + \frac{q}{m}\frac{dy}{dt}B_z - \frac{q}{m}\frac{dz}{dt}B_y \qquad \text{(A-3)}$$

$$\frac{d^2y}{dt^2} = -\frac{q}{m}\frac{\partial V}{\partial y} + \frac{q}{m}\frac{dz}{dt}B_x - \frac{q}{m}\frac{dx}{dt}B_z \qquad \text{(A-3)}$$

$$\frac{d^2z}{dt^2} = -\frac{q}{m}\frac{\partial V}{\partial z} + \frac{q}{m}\frac{dx}{dt}B_y - \frac{q}{m}\frac{dy}{dt}B_x \qquad \text{(A-4)}$$

A problem of practical concern involves certain constraints on $\vec{B}(\vec{r})$ and $V(\vec{r})$ within a specified volume. The magnetic field is assumed to be uniform in direction but not necessarily in magnitude with the magnetic field normal to the gradient of the potential. Consider a region of space from $x = a$ to $x = b$ where the magnetic field is along the z-axis but with a magnitude that depends arbitrarily on x. The potential is also allowed to vary arbitrarily in x with the constraint that the total change in potential from $x = a$ to $x = b$ in a fixed quantity ΔV. A particle impinges on this region from $x < a$ with an incident velocity $\vec{v}_o$. The region from $x = a$ to $x = b$ may form a barrier to particle penetration to the region $x > b$ if the particle has lost all momentum in the x-direction upon reaching $x = b$. With the stated limitations on $V(x)$ and $\vec{B}(x)$, Eqns. (A-2) to (A-4) become:

$$\frac{d^2x}{dt^2} = -\frac{q}{v}\frac{\partial V}{\partial x} + \frac{q}{m}\frac{dy}{dt}B_z \qquad \text{(A-5)}$$

$$\frac{d^2y}{dt^2} = -\frac{q}{m}\frac{dx}{dt}B_z \qquad \text{(A-6)}$$

$$\frac{d^2z}{dt^2} = 0 \ . \tag{A-7}$$

Equation (A-7) yields a constant velocity in the z-direction equal to that initial velocity component v_{o_z}. To determine the exact trajectory, Eqns. (A-5) and (A-6) must be solved simultaneously. However, a simplification is possible in that the requirement for a zero velocity in the x-direction implies that the incident energy plus the energy acquired in traversing the potential difference ΔV should all appear as kinetic energy in the y-z plane at $x = b$ giving,

$$\tfrac{1}{2} m(v_{o_x}{}^2 + v_{o_y}{}^2 + v_{o_z}{}^2) - q\Delta V = \tfrac{1}{2} m\,(v_y{}^2(x=b) + v_{o_z}{}^2) \tag{A-8}$$

or,

$$v_{o_x}{}^2 + v_{o_y}{}^2 - 2q\Delta V/m = v_y{}^2(x = b) \ . \tag{A-9}$$

Equation (A-6) may be written as:

$$\frac{d}{dt}\frac{dy}{dt} = -\frac{q}{m} B_z(x) \frac{dx}{dt} \tag{A-10}$$

or

$$dv_y = -\frac{q}{m} B_z(x) dx \ . \tag{A-11}$$

Integrating over the barrier region

$$\int_{v_{o_y}}^{v_{f_y}} dv_y = -\frac{q}{m}\int_a^b B(x)dx \ . \qquad \text{(A-12)}$$

Let the total field integral be represented by B_{ab}

$$v_{f_y} - v_{o_y} = -\frac{q}{m} B_{ab} \qquad \text{(A-13)}$$

or,

$$\frac{m}{|q|} v_{o_y} + \frac{m}{|q|} (v_{o_x}{}^2 + v_{o_y}{}^2 + 2|q|\Delta V/m)^{\frac{1}{2}} = B_{ab} \ . \qquad \text{(A-14)}$$

This, then is the criterion that must be met by the integrated magnetic field for containment of a particle of specified incident velocity crossing a region of total potential charge ΔV. If the incident energy of an electron is negligible with respect to $e\Delta V$ then the criterion simplifies to:

$$B_{ab} = (2m\Delta V/e)^{\frac{1}{2}} \ . \qquad \text{(A-15)}$$

APPENDIX B

SEEDING RATE FROM A BEVELED SOURCE

Experimental arrangements for ion beam texturing include a beveled source of seed material placed on top of a substrate (Fig. B-1). Part of the substrate is covered with the seed source providing a control surface for comparison with the part that is uncovered and exposed to both sputter deposition of seed material and ion bombardment. This study will focus on the deposition rate of seed material onto the substrate from such a beveled surface.

A number of assumptions will be implicit in this seeding rate model. The ion beam will be assumed to have uniform current density over the area of interest and the beam will be directed normal to the substrate surface. The emission of sputtered seed atoms from points on the beveled edge will be assumed to correspond to a cosine distribution about the local surface normal. This assumption is in close agreement with experimental observations where only small departures from a cosine distribution have been observed.[1,2,3,4,5]

To model in detail the emission of sputtered atoms from the beveled surface and their subsequent deposition onto the substrate, we explore the geometry indicated in Fig. B-2. Let $d\Gamma_2$ be the rate of sputtered particle collection at the element of area da_2 in particles per unit time arriving from the element of area da_1. This rate is proportional to the fraction of hemispherical solid angle subtended by da_2 as viewed from da_1, i.e., $da_2 \cos\phi_2 / 2\pi r^2$. The emission from da_1 in the direction ϕ_1 is proportional to $da_1 \cos\phi_1$ because of the assumed cosine emission distribution. The emission from da_1 arriving at da_2 can thus be expressed as:

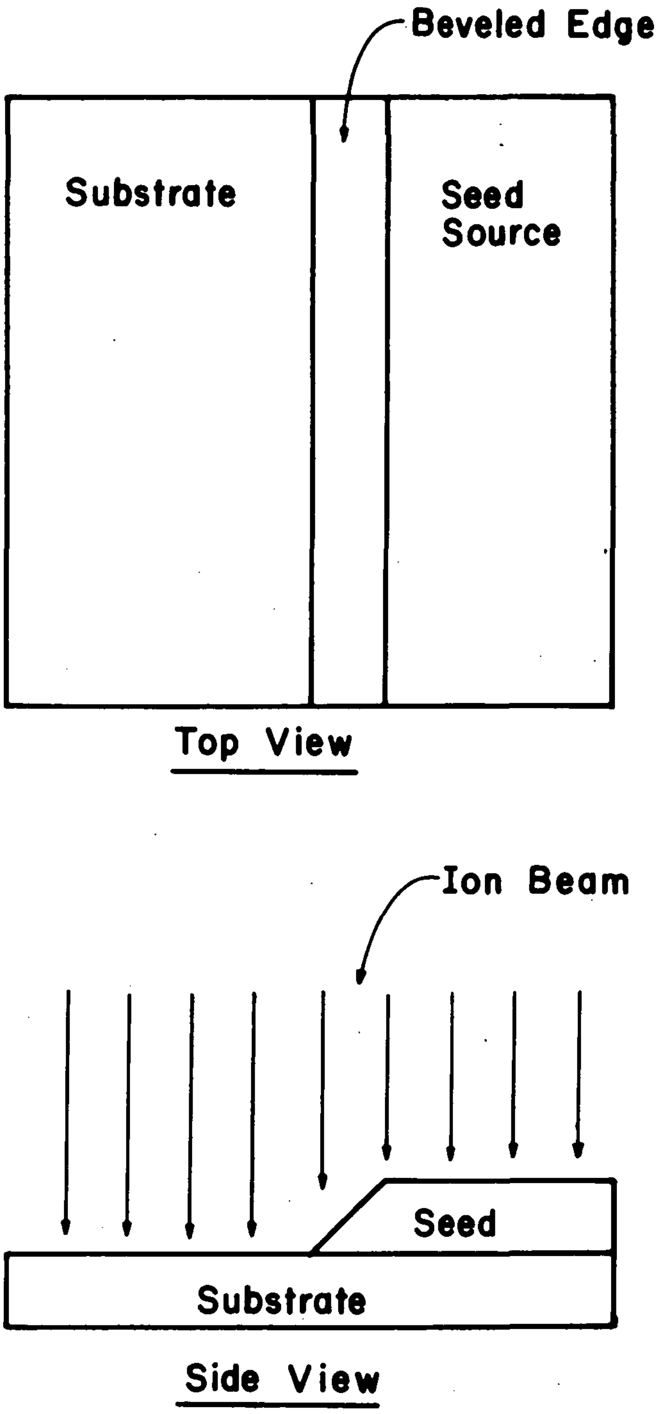

Figure B-1. Experimental seeding arrangement for ion beam texturing.

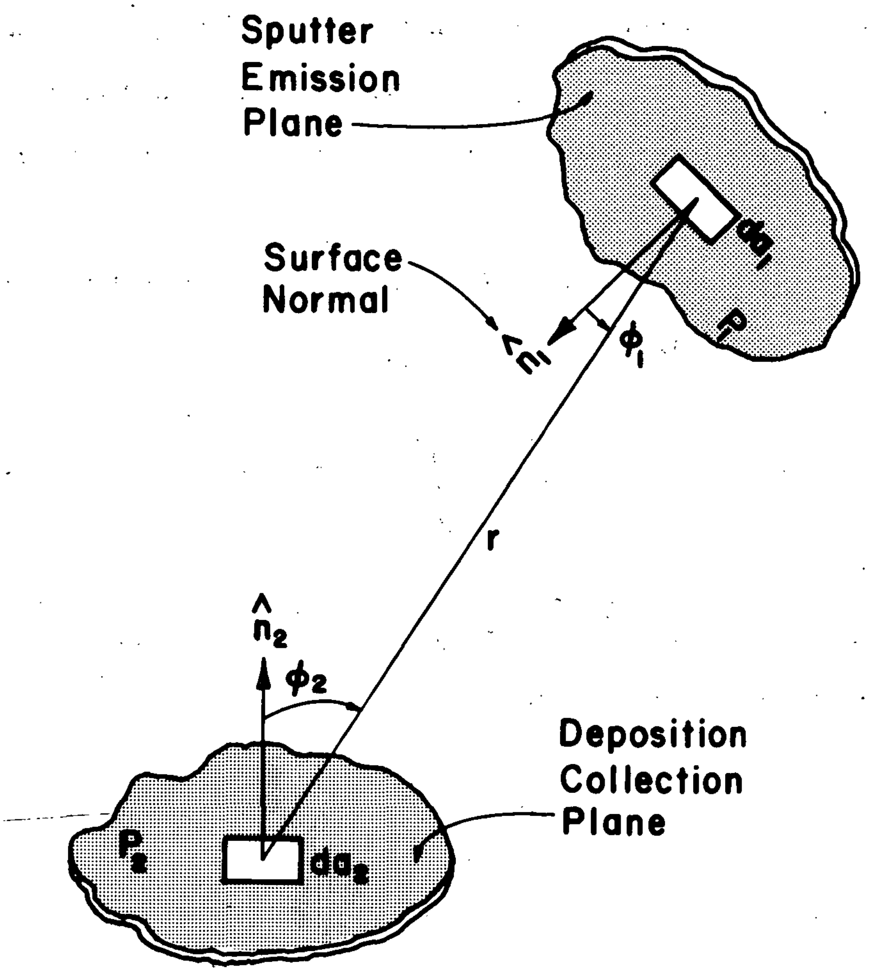

Figure B-2. Geometry for sputter emission and flux collection.

$$d\Gamma_2 = F\, da_1 \cos\phi_1 \frac{da_2 \cos\phi_2}{2\pi r^2} \tag{B-1}$$

where F is a constant of proportionality representing the sputtered flux in particles per unit time per unit area emitted normal to da_1. The factor F normalizes to total emission from the emitter plane, P_1.

Integrating over the plane P_1 will yield the total rate of particle collection at da_2

$$\Gamma_2 = \frac{F da_2}{2\pi} \int_{P_1} \frac{\cos\phi_2}{r^2} \cos\phi_1 da_1 \ . \tag{B-2}$$

An effective flux at da_2 is found by dividing the particle arrival rate by the area of the element da_2

$$F_2 = \frac{\Gamma_2}{da_2} = \frac{F}{2\pi} \int_{P_1} \frac{\cos\phi_2}{r^2} \cos\phi_1 da_1 \ . \tag{B-3}$$

The relative seeding rate as a function of position on the substrate plane can thus be found from the integral indicated in Eq. (B-3). This integral will, in general, not be solvable in closed form and will thus require a numerical procedure for evaluation.

Figure B-3 shows the geometry and definition of variables to be used in a numerical integration algorithm. From Fig. B-3 it can be seen that:

$$r^2 = (x_2 - x_1)^2 + y_1^2 \sin^2\beta + (y_2 + y_1\cos\beta)^2 \ , \tag{B-4}$$

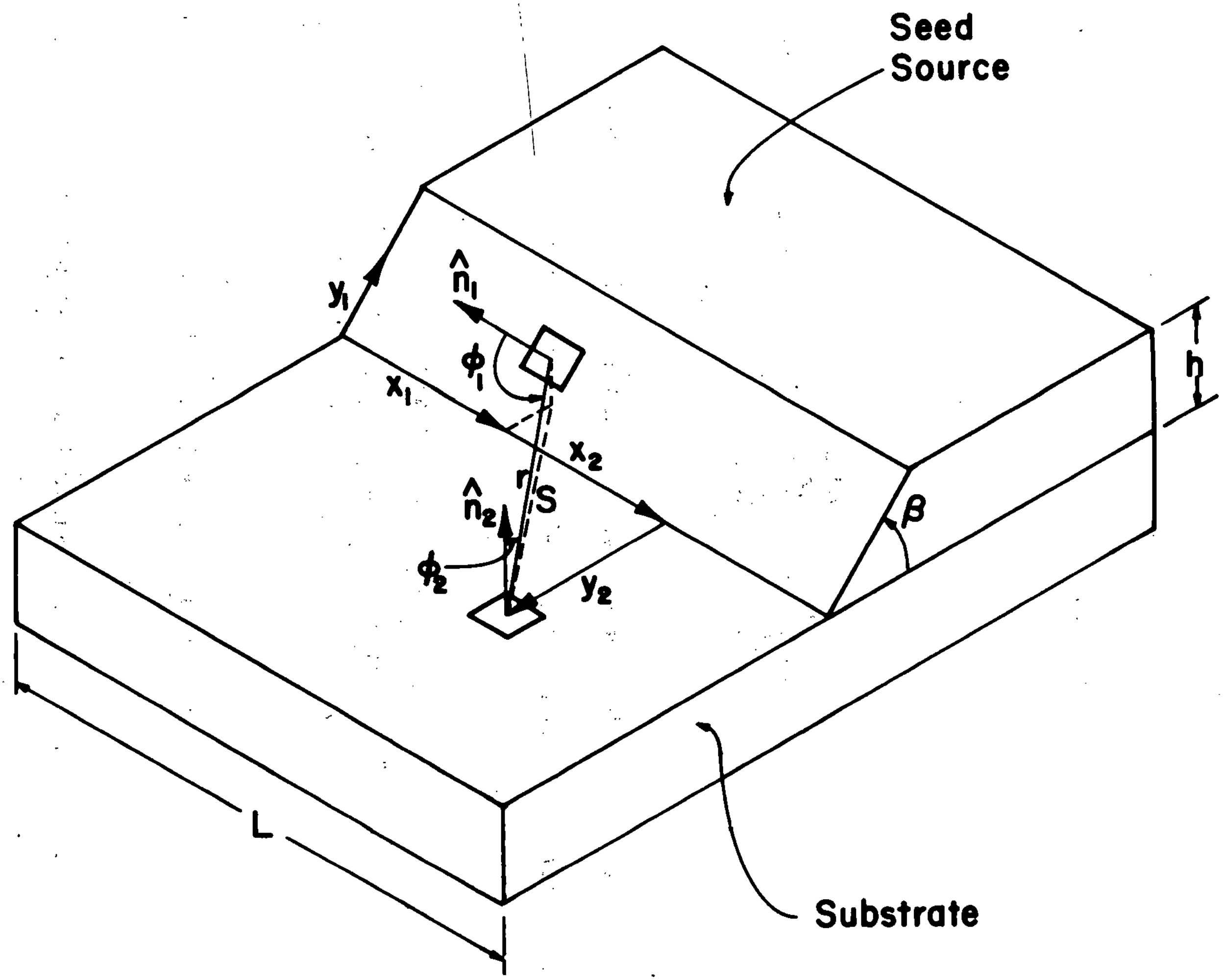

Figure B-3. Geometry and parameter definition for numerical integration algorithm.

$$\cos\phi_2 = y_1\sin\beta/r \ , \tag{B-5}$$

and that

$$\cos\phi_1 = y_2\sin\beta/r \ . \tag{B-6}$$

Thus Eq. (B-3) becomes:

$$F_2 = \frac{F}{2\pi}\int_o^L dx_1 \int_o^{h/\sin\beta} dy_1 \frac{y_1y_2\sin^2\beta}{r^4} \ . \tag{B-7}$$

Given the coordinates of the observation point and the dimensions and bevel angle of the seed source Eq. (B-7) can be written:

$$F_2 = \frac{Fy_2\sin^2\beta}{2\pi}\int_o^L dx_1 \int_o^{h/\sin\beta} dy_1y_1\Big[(x_2-x_1)^2 + y_1{}^2\sin^2\beta + (y_2+y_1\cos\beta)^2\Big]^{-2} \ . \tag{B-8}$$

The numerical integration is carried out in N increments of Δx, and M increments of Δy, where:

$$\Delta x_1 = L/N \tag{B-9}$$

and

$$\Delta y_1 = h/M\sin\beta \ . \qquad \text{(B-10)}$$

The integral can now be written approximately as a summation:

$$\frac{F_2}{F} = \frac{y_2\sin^2\beta}{2\pi} \sum_{i=1}^{N} \sum_{j=1}^{M} \frac{\Delta x_1 \Delta y_1 \; y_{1j}}{\left[\left(x_2 - x_{1_i}\right)^2 + y_{1j}{}^2\sin^2\beta + \left(y_2 + y_{1j}\cos\beta\right)^2\right]^2} \qquad \text{(B-11)}$$

where

$$x_{1_i} = (i-\tfrac{1}{2})\Delta x_1 \qquad \text{(B-12)}$$

and

$$y_{1_i} = (j-\tfrac{1}{2})\Delta y_1 \ . \qquad \text{(B-13)}$$

A program was written to carry out the numerical procedure indicated in Eq. (B-11). The factor F is carried as a constant through the numerical work. It is, however, proportional to the ion arrival rate and the sputter yield of the seed material.

$$F = R_i \cos\beta \; Y(\beta) \qquad \text{(B-14)}$$

where R_i is the ion arrival rate in ions per unit area per unit time at the substrate, the cosine of β takes into account the tilt of the beveled edge with respect to the ion beam direction, and $Y(\beta)$ is the sputter yield of the seed material at the angle β in atoms per ion.

First the integration step size necessary to assure convergence within one percent was investigated. The parameters used corresponded to a realistic experimental arrangement: $L/h = 8.0$, $\beta = 45°$, $x_2/h = 4.0$, and $y_2/h = 1.0$. The results of calculating F_2/F as a function of N and M are given in Table 5-1.

Table B-1. Integrations with Various Increments of Area.

N	M	F_2/F
6	1	3.0645×10^{-2}
11	2	2.8013×10^{-2}
17	3	2.6867×10^{-2}
23	4	2.6396×10^{-2}
28	5	2.6164×10^{-2}
34	6	2.6035×10^{-2}
40	7	2.5955×10^{-2}
45	8	2.5903×10^{-2}
51	9	2.5867×10^{-2}
154	27	2.5746×10^{-2}
20	7	2.5957×10^{-2}
10	7	2.5948×10^{-2}
8	7	2.5881×10^{-2}
6	7	2.5489×10^{-2}
4	7	2.3271×10^{-2}

Letting the $N = 154$, $M = 27$ value be the standard, this standard is approached within 1% by letting $N = 40$ and $M = 7$. However, N can be further reduced by a factor of 4 without sacrificing significant accuracy. These values, $N = 10$ and $M = 7$, are appropriate when the observation point y_2/h is a unit distance, or greater, from the source. If y_2/h is decreased by a factor of two, accuracy can be maintained by increasing both M and N each by a factor of two. Other, similar adjustments would be appropriate as y_2/h changes.

The seeding rate variation as a function of distance from the center of the seed source is given in Table B-2 for the choice of parameters: $L/h = 8.0$, $\beta = 45°$, $x_2/h = 4.0$.

The data of Table B-2 are plotted in Figs. B-4 and B-5. The seeding rate decreases rapidly near the source and falls off more slowly at greater distances as shown in Fig. B-4. For typical dimensions of seed source and substrate, the seeding rate can vary by one or two orders of magnitude over the substrate. Both seeding rate and distance are represented on logarithmic scales in Fig. B-5. The linear portion at large distances from the source has a slope corresponding to an inverse cubic variation with distance in agreement with the y_2 dependence of Eq. (B-8). At small distances from the source, the seeding rate from a source of semi-infinite extent tilted at an angle β.

The limit can be calculated by integrating Eq. (B-8) after changing to suitable dimensionless variables: $u = x_1/y_2$ and $\upsilon = y_1/y_2$.

Table B-2. Seeding Rate along the Centerline of the Source.

y_2/h	F_2/F	y_2/h	F_2/F
0.03125	7.07×10^{-2}	2.6	8.02×10^{-3}
0.0625	6.81×10^{-2}	2.7	7.55×10^{-3}
0.125	6.32×10^{-2}	2.8	7.11×10^{-3}
0.5	4.18×10^{-2}	2.9	6.71×10^{-3}
0.6	3.77×10^{-2}	3.0	6.33×10^{-3}
0.7	3.41×10^{-2}	3.1	5.98×10^{-3}
0.8	3.10×10^{-2}	3.2	5.66×10^{-3}
0.9	2.82×10^{-2}	3.4	5.07×10^{-3}
1.0	2.59×10^{-2}	3.5	4.81×10^{-3}
1.1	2.38×10^{-2}	3.6	4.57×10^{-3}
1.2	2.18×10^{-2}	3.7	4.34×10^{-3}
1.3	2.01×10^{-2}	3.8	4.12×10^{-3}
1.4	1.85×10^{-2}	3.9	3.92×10^{-3}
1.5	1.71×10^{-2}	4.0	3.73×10^{-3}
1.6	1.58×10^{-2}	8.0	8.70×10^{-4}
1.7	1.47×10^{-2}	16	1.37×10^{-4}
1.8	1.37×10^{-2}	32	1.83×10^{-5}
1.9	1.27×10^{-2}	64	2.35×10^{-6}
2.0	1.19×10^{-2}	128	2.99×10^{-7}
2.1	1.11×10^{-2}	256	3.77×10^{-8}
2.2	1.04×10^{-2}	512	4.72×10^{-9}
2.3	9.70×10^{-3}	1024	5.92×10^{-10}
2.4	9.09×10^{-3}	2048	7.40×10^{-11}
2.5	8.54×10^{-3}	4096	$9\ 26 \times 10^{-12}$

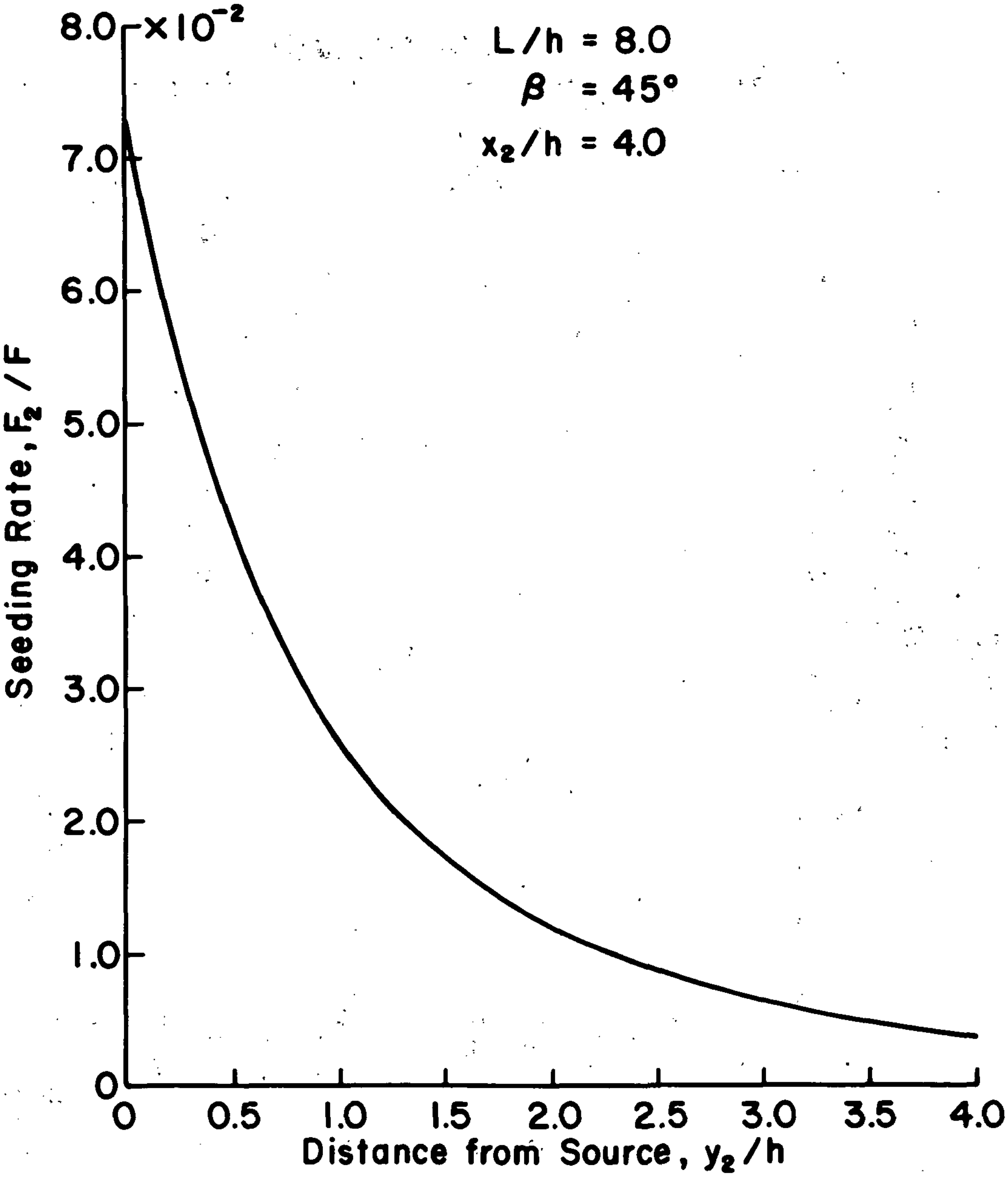

Figure B-4. Seeding rate versus distance from the seed source along the centerline.

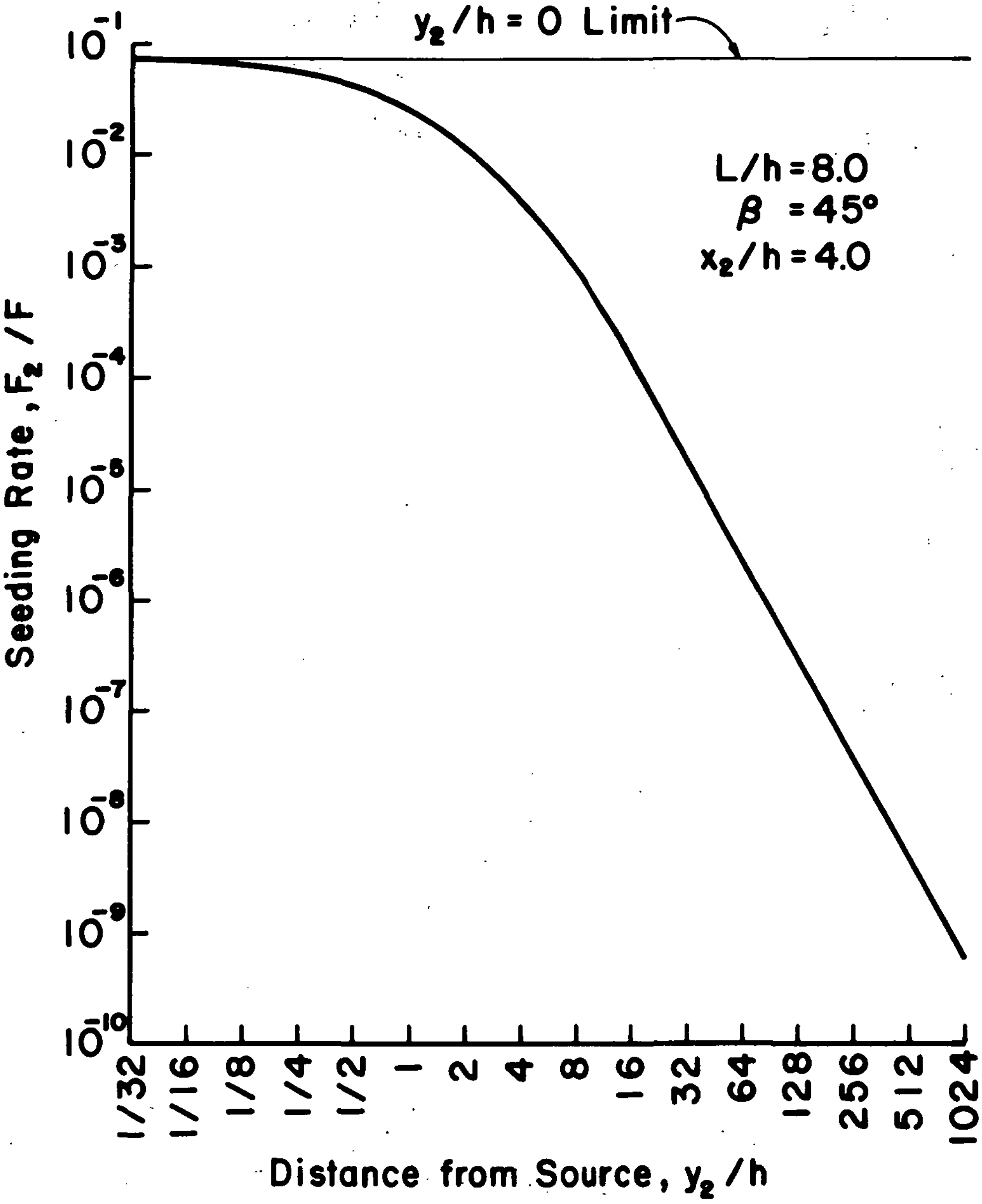

Figure B-5. Seeding rate versus distance from the seed source along the centerline (log-log plot).

$$(F_2/F)_{\text{limit}} = \frac{\sin^2\beta}{2\pi} \int_{-\infty}^{\infty} du \int_{0}^{\infty} d\upsilon \; \upsilon \left[u^2 + \upsilon^2 \sin^2\beta + (1 + \upsilon\cos\beta)^2 \right]^{-2} . \tag{B-15}$$

Equation (B-15) can be integrated to yield:

$$(F_2/F)_{\text{limit}} = (1-\cos\beta)/4 \tag{B-16}$$

which can be evaluated for $\beta = 45°$ as 7.32×10^{-2}. This value is plotted in Fig. B-5 as the $y_2/h = 0$ limit which the function approaches very closely at small y^2/h.

Table B-3 lists calculated values for F_2/F obtained over a regular mesh covering the substrate region for the same geometrical parameters used for Table B-2. The data of Table B-3 are plotted in Fig. B-6. Close to the seed source there is a strong variation with lateral position dropping to only about one half the center value at the extreme ends where flux contributions are being received from the right or left side only. As the observation line is moved further from the source the lateral variations diminish considerably because the subtended angle of the seed source is then changed less when observed from various lateral positions.

An Auger surface composition analysis done at various distances from the shield location on a seeded sample should provide an experimental verification of the calculated profile shown in Fig. B-4.

Table B-3. Calculated Vaues for F_2/F for Positions on the Substrate.

	y_2/h			
x_2/h	0.5	1.0	1.5	2.0
0.0	2.11×10^{-2}	1.33×10^{-2}	8.92×10^{-3}	6.35×10^{-3}
0.5	3.32×10^{-2}	1.86×10^{-2}	1.16×10^{-2}	7.89×10^{-3}
1.0	3.82×10^{-2}	2.20×10^{-2}	1.37×10^{-2}	9.20×10^{-3}
1.5	4.02×10^{-2}	2.39×10^{-2}	1.51×10^{-2}	1.02×10^{-2}
2.0	4.11×10^{-2}	2.49×10^{-2}	1.60×10^{-2}	1.09×10^{-2}
2.5	4.15×10^{-2}	2.55×10^{-2}	1.66×10^{-2}	1.14×10^{-2}
3.0	4.17×10^{-2}	2.58×10^{-2}	1.69×10^{-2}	1.17×10^{-2}
3.5	4.18×10^{-2}	2.59×10^{-2}	1.71×10^{-2}	1.18×10^{-2}
4.0	4.18×10^{-2}	2.59×10^{-2}	1.71×10^{-2}	1.19×10^{-2}

	y_2/h			
x_2/h	2.5	3.0	3.5	4.0
0.0	4.72×10^{-3}	3.62×10^{-3}	2.85×10^{-3}	2.29×10^{-3}
0.5	5.67×10^{-3}	4.25×10^{-3}	3.28×10^{-3}	2.60×10^{-3}
1.0	6.53×10^{-3}	4.83×10^{-3}	3.69×10^{-3}	2.89×10^{-3}
1.5	7.22×10^{-3}	5.32×10^{-3}	4.04×10^{-3}	3.14×10^{-3}
2.0	7.75×10^{-3}	5.70×10^{-3}	4.32×10^{-3}	3.35×10^{-3}
2.5	8.12×10^{-3}	5.99×10^{-3}	4.54×10^{-3}	3.52×10^{-3}
3.0	8.36×10^{-3}	6.18×10^{-3}	4.69×10^{-3}	3.64×10^{-3}
3.5	8.49×10^{-3}	6.30×10^{-3}	4.78×10^{-3}	3.71×10^{-3}
4.0	8.54×10^{-3}	6.33×10^{-3}	4.81×10^{-3}	3.73×10^{-3}

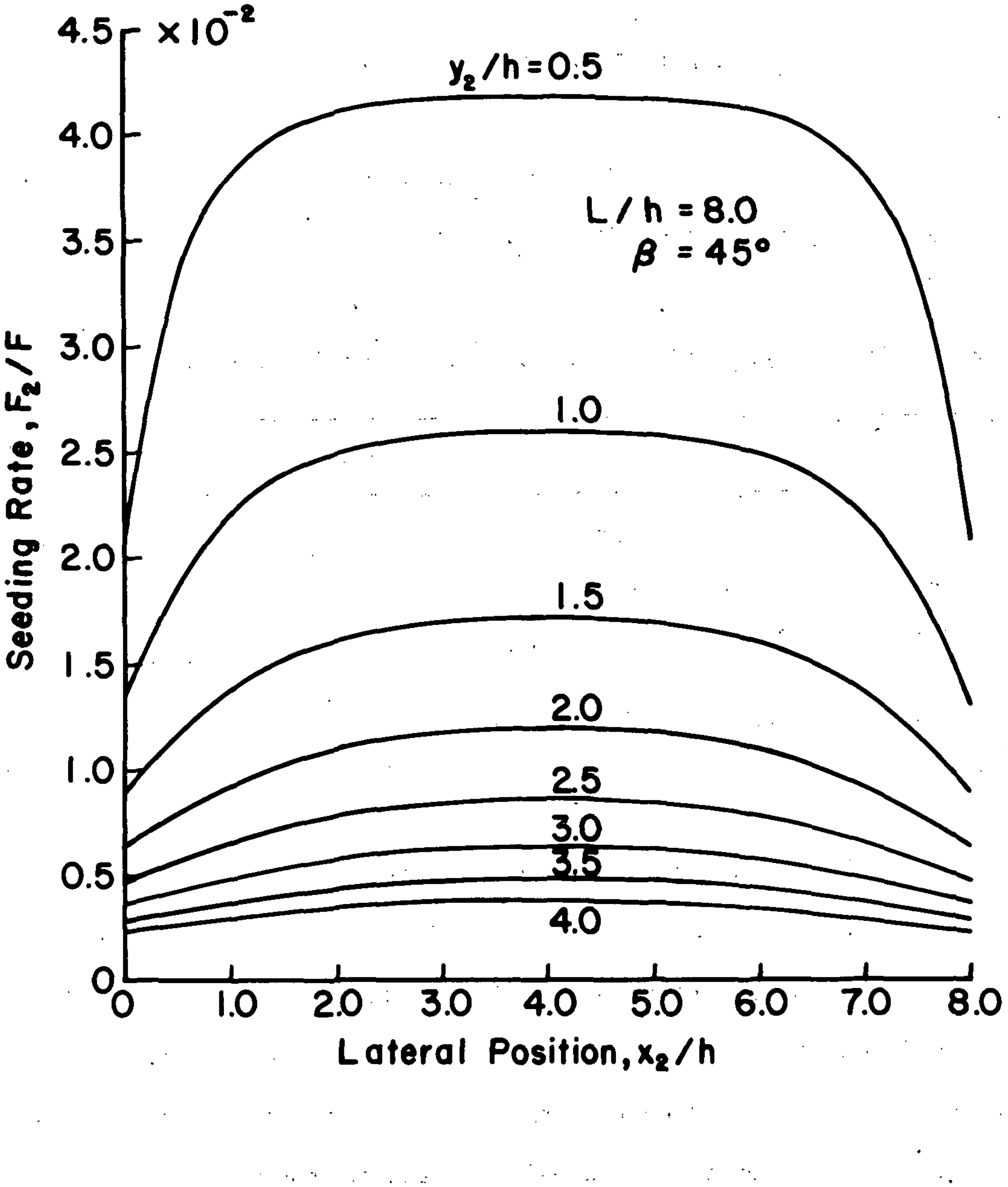

Figure B-6. Seed flux on lines parallel to the source at increasing distances from the source.

From seeding theory (see Chapter IV) we have shown that the critical temperature varies inversely as the logarithm of the seeding density times a constant.

$$T_c \approx \frac{E_d \; 11600^\circ K}{25 + \ln F_s} \tag{B-17}$$

for reasonable magnitudes of the variables (E_d in eV). Table B-4 shows a possible variation of T_c with F_s.

Table B-4. Variation of Critical Temperature with Seed Fraction.

T_c	F_s	ΔT_c
735°K	.0001	
		94°K
641°K	.001	
		72°K
569°K	.01	
		58°K
511°K	.1	
		47°K
464°K	1.0	

Thus, the variation in seeding density across a substrate can be translated into a corresponding variation in the critical texturing temperature across the substrate. Contours of equal critical temperature can in theory be specified as to shape and position. If a substrate were held at a temperature corresponding to a contour a certain distance from the seed source, then locations between the source and that contour would be textured and locations beyond would remain non-textured. Such a texture boundary would be convex, curved and symmetrical about the centerline of the seed source. Silicon seeded with Mo has exhibited textured regions suggestive of this effect.

The technique presented here for calculating seeding rate can be used to determine appropriate seed source geometries to be utilized when uniform seeding is desired over an entire substrate to generate uniform texturing. Such a possibility is the use of a wire mesh normal to the beam direction.

DISTRIBUTION LIST

	No. of Copies
National Aeronautics and Space Administration	
Washington, DC 20546	
Attn: RPE/Mr. Wayne Hudson	1
Mr. Daniel H. Herman, Code SL	1
National Aeronautics and Space Administration	
Lewis Research Center	
21000 Brookpark Road	
Cleveland, OH 44135	
Attn: Research Support Procurement Section	
Mr. Allen Jones, MS 500-313	1
Technology Utilization Office, MS 3-19	1
Report Control Office, MS 5-5	1
Library, MS 60-3	2
N. T. Musial, MS 600-113	1
Spacecraft Technology Division, MS 501-8	
Mr. H. Douglass	1
Mr. R. Finke	1
Mr. D. Byers	1
Mr. B. Banks	1
Mr. S. Domitz	1
Mr. F. Terdan	1
Mr. W. Kerslake	1
Mr. Vincent K. Rawlin	1
Mr. M. Mirtich	20
Physical Science Division, MS 301-1	
Mr. W. E. Moeckel	1
National Aeronautics and Space Administration	
Marshall Space Flight Center	
Huntsville, AL 35812	
Attn: Mr. Jerry P. Hethcoate	1
Research and Technology Division	
Wright-Patterson AFB, OH 45433	
Attn: (ADTN) Lt. David A. Fromme	1
NASA Scientific and Technical Information Facility	
P. O. Box 8757	
Baltimore/Washington International Airport	
Baltimore, MD 21240	40
Case Western Reserve University	
10900 Euclid Avenue	
Cleveland, OH 44106	
Attn: Dr. Eli Reshotko	1
Royal Aircraft Establishment	
Space Department	
Farnborough, Hants, ENGLAND	
Attn: Dr. D. G. Fearn	1

United Kingdom Atomic Energy Authority
Culham Laboratory
Abingdom, Berkshire, ENGLAND
Attn: Dr. P. J. Harbour 1
Dr. M. F. A. Harrison 1
Dr. T. S. Green 1

National Aeronautics and Space Administration
Goddard Space Flight Center
Greenbelt, MD 20771
Attn: Mr. W. Isley, Code 734 1
Mr. R. Bartlett, Code 713 1
Mr. R. Callens, Code 734 1

SAMSO
Air Force Unit Post Office
Los Angeles, CA 90045
Attn: Capt. D. Egan/ SYAX 1

Comsat Laboratories
P. O. Box 115
Clarksburg, MD 20734
Attn: Mr. B. Free 1
Mr. O. Revesz 1

Roket Propulsion Laboratory
Edwards AFB, CA 93523
Attn: LKDA/Ms. Tom Waddell 2

DFVLR - Institut für Plasmadynamik
Technische Universitat Stuttgart
7 Stuttgart-Vaihingen
Allmandstr 124
WEST GERMANY
Attn: Dr. G. Krülle 1
Mr. H. Bessling 1

Giessen University
1st Institute of Physics
Geissen, WEST GERMANY
Attn: Professor H. W. Loeb 1

Jet Propulsion Laboratory
4800 Oak Grove Drive
Pasadena, CA 91102
Attn: Dr. Kenneth Atkins 1
Technical Library 1
Mr. Eugene Pawlik 1
Mr. James Graf 1

Electro-Optical Systems, Inc.
300 North Halstead
Pasadena, CA 91107
Attn: Mr. R. Worlock 1
Mr. E. James 1
Mr. W. Ramsey 1

TRW, Inc.
TRW Systems
One Space Park
Redondo Beach, CA 90278
Attn: Mr. M. Huberman 1
Dr. J. M. Sellen 1
Dr. S. Zafran 1

National Aeronautics and Space Administration
Ames Research Center
Moffett Field, CA 94035
Attn: Technical Library 1

National Aeronautics and Space Administration
Langley Research Center
Langley Field Station
Hampton, VA 23365
Attn: Technical Library 1

Hughes Research Laboratories
3011 Malibu Canyon Road
Malibu, CA 90265
Attn: Dr. Jay Hyman 1
Mr. J. H. Molitor 1
Dr. R. L. Poeschel 1
Mr. R. Vahrenkamp 1
Dr. John R. Beattie 1

United States Air Force
Office of Scientific Research
Washington, DC 20025
Attn: Mr. M. Slawsky 1

Princeton University
Princeton, NJ 08540
Attn: Mr. W. F. Von Jaskowsky 1
Dean R. G. Jahn 1
Dr. K. E. Clark 1

Communications Research Centre
Ottawa, Ontario, CANADA
Attn: Dr. W. F. Payne 1

Joint Institute for Laboratory Astrophysics
University of Colorado
Boulder, CO 80302
Attn: Dr. Gordon H. Dunn 1

Department of Aeronautics and Astronautics
Stanford University
Stanford, CA 94305
Attn: Professor Howard S. Seifert 1

Boeing Aerospace Company
P. O. Box 3999
Seattle, WA 98124
Attn: Mr. Donald Grim 1

Intelcom Rad Tech
7650 Convoy Court
P. O. Box 80817
San Diego, CA 92138
Attn: Dr. David Vroom 1

Lockheed Missiles and Space Company
Sunnyvale, CA 94088
Attn: Dr. William L. Owens
Propulsion Systems, Dept. 62-13 1

Fairchild Republic Company
Farmingdale, NY 11735
Attn: Dr. William Guman 1

COMSAT Corporation
950 L'Enfant Plaza S.W.
Washington, DC 20024
Attn: Mr. Sidney O. Metzger 1

Electrotechnical Laboratory
Tahashi Branch
5-4-1 Mukodai-Machi, Tanashi-Shi
Tokyo, JAPAN
Attn: Dr. Katsuva Nakayama 1

Office of Assistant for Study Support
Kirtland Air Force Base
Albuquerque, NM 87117
Attn: Dr. Calvin W. Thomas OAS Ge 1
Dr. Berhart Eber OAS Ge 1

Bell Laboratories
600 Mountain Avenue
Murray Hill, NJ 07974
Attn: Dr. Edward G. Spencer 1
Dr. Paul H. Schmidt 1

Massachusetts Institute of Technology
Lincoln Laboratory
P. O. Box 73
Lexington, MA 02173
Attn: Dr. H. I. Smith 1

Sandia Laboratories
Mail Code 5742
Albuquerque, NM 87115
Attn: Mr. Ralph R. Peters 1

Service du Confinement des Plasma
Centre d'Etudes Nucléaires - F.A.R.
B.P. 6
92260 Fontenay-aux-Roses
FRANCE
Attn: Dr. J. F. Bonal 1

International Business Machines Corporation
Thomas J. Watson Research Center
P. O. Box 218
Yorktown Heights, NY 10598
Attn: Dr. Jerome J. Cuomo 1
Dr. James M. E. Harper 1

IBM East Fishkill
D/42K, Bldg. 300-40F
Hopewell Junction, NY 12533
Attn: Dr. Charles M. McKenna 1

DFVLR-Forschungszentrum Braunschweig
Inst. A, Flughafen
3300 Braunschweig
WEST GERMANY
Attn: Dr. H. A. W. Bessling 1

Ion Beam Equipment, Inc.
P. O. Box 0
Norwood, NJ 07648
Attn: Dr. W. Laznovsky 1

Optic Electronics Corporation
11477 Pagemill Road
Dallas, TX 75243
Attn: Bill Hermann, Jr. 1

Circuits Processing Apparatus, Inc.
725 Kifer Road
Sunnyvale, CA 94086
Attn: Spencer R. Wilder 1

Ion Tech, Inc.
1807 E. Mulberry
P. O. Box 1388
Fort Collins, CO 80522
Attn: Dr. Gerald C. Isaacson 1

Physicon Corporation
221 Mt. Auburn Street
Cambridge, MA 02138
Attn: H. von Zweck 1

Commonwealth Scientific Corporation
500 Pendleton Street
Alexandria, VA 22314
Attn: George R. Thompson 1

Veeco Instruments Inc.
Terminal Drive
Plainview, NY 11803
Attn: Norman Williams 1